An Investigation of High Tc Superconductivity in the Doped $YBa_2Cu_3O_7$ and Ln_2CuO_4 (Ln=La, Nd) Systems by Neutron Scattering and Nuclear Magnetic Resonance

Laurence Wilfred John Caves

A thesis submitted to the University of Warwick for admission to the degree of Doctor of Philosophy

Department of Physics

September 1992

This thesis is dedicated to all my family but especially to my wife, Helen.

LIST OF CONTENTS

LIST OF TABLES

LIST OF FIGURES

ACKNOWLEDGEMENTS

I would like to thank my supervisor Dr D McK Paul (now Professor) for his guidance, over the years it has taken to complete this thesis, in this rapidly developing field. Many other people have put in hours of patient work to bring me this far. Foremost among them is Dr G Balakrishnan (Geetha) who taught me the art of good sample preparation and characterisation — at one stage she gave up on me and went back to India but has recently relented. I am also very grateful to all the instrument scientists and technicians who have assisted me in my experimental work at both RAL and the ILL. In the former group I would name especially Dr A D Taylor, Dr R Osborn, Dr W I F David, Zoe Bowden and Richard Ibberson (Uncle Rixie). In the latter group — who due to a strange act of fate get no other mention in this work — I would like to thank Garry McIntyre and Mary Vrtis for their advice and practical help and also all those who enlightened me to the more gastronomic side of neutron scattering (especially Prof. B D Rainford, who also mentioned crystal fields to me).

Closer to home, I have been thankful for the technical help of David, "Woodie", Bob, Harold and Pat (to name a few) and have enjoyed fruitful discussions (sometimes about physics) with the members of the NMR coffee club as it evolved over the years. I have also benefited from the entertainment of the "Solid State Boys" — they know who they are — as a result of my "living" for a time in the Laser-Ultrasound empire (thank you to Prof. S Palmer for the desk and chair). Finally I would give an extra-special thanks to Andy Howes who stopped me "climbing the walls" at tense times by letting me "ab-off" the ceiling instead.

Even closer to home , I would like to acknowledge the support of my wife, Helen, who has gone out of her way (and mine) to give me the opportunity to finish writing-up. Both our parents have also done their best in this respect too — mine stayed in Canada most of the time. Last, but not least, thank you to Richard and Christiana for being so patient with Daddy.

Declaration

The work for this thesis was based in the Department of Physics at the Univeristy of Warwick from October 1987 to September 1990. This thesis is the result of my own independent research except where referenced and has not been previously submitted for any other degree.

Some parts of this thesis have been published:

1. "NMR evidence for fluctuating, localised magnetic fields in zinc - doped $YBa_2Cu_3O_{7-\delta}$."
Balakrishnan G, Caves L W J, Dupree R, Paul D McK and Smith M E 1989 *Physica C* **161** 9

2. "High energy crystal field excitations in $Pr_xY_{1-x}Ba_2Cu_3O_{7-\delta}$."
Boothroyd A T, Caves L W J, Paul D McK and Osborn R 1991 *Bull Mater. Sci.* **14** 613

An additional paper was written over the same period:

"A ^{89}Y NMR study of Pr and Nd doped $YBa_2Cu_3O_7$."
Han Z P, Dupree R, Paul D McK, Howes A P and Caves L W J 1991 *Physica* **C 181** 355

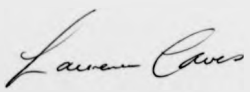

L. W. J. Caves

ABSTRACT

Neutron scattering and nuclear magnetic resonance are excellent probes of the physical properties of the high T_c Superconductors. Both techniques have been used in this work.

$La_{2-x}Ba_xCuO_4$ [214] has a maximum T_c of ~30K and was one of the first of the high T_c materials to be identified. The structure of the undoped parent compound has been known for some time so any structural changes as a result of Ba doping might also be associated with the onset of superconductivity. A high resolution neutron powder diffraction study is reported for a range of doping and temperatures (especially in the region of T_c). The parent compound is confirmed to be tetragonal at room temperature; space group I4/mmm. For Ba doping near to x=0.15 a sequence of phase transitions is observed: tetragonal (I4/mmm) at room temperature, orthorhombic (Abma) below ~250K and returning to tetragonal ($P4_2/ncm$) below ~100K, but co-existing with the orthorhombic phase to low temperatures. Refined structural cell parameters are given for each doping at selected temperatures. The reasons for these changes and their possible link with the onset of superconductivity is discussed.

$Nd_{2-x}Ce_xCuO_4$ has been reported to be an n-type superconductor (in contrast to other high T_c compounds) with a maximum T_c of ~24K. It has a similar structure to La[214] and has also been the subject of a high resolution neutron powder diffraction study. The range of doping was more restricted than in the Ba doped La[214] so as to match the range for which superconductivity occurs. The temperature dependence of the structure was looked at for each **x** in the vicinity of T_c. No structural phase transitions were resolved in any of the samples — all remained tetragonal (I4/mmm). A smooth decrease in lattice parameters **a** and **c** was observed as a function of temperature. Refined cell parameters are given at selected temperatures for each **x**. The contrast with La[214] and the possibility of phase separation are discussed.

The only magnetic rare-earth (R) to suppress superconductivity upon substitution for Y in $YBa_2Cu_3O_7$ [123] (T_c ~90K) is Pr. It was initially suggested that this could be explained by a 4+ Pr valence resulting in Cu-O plane hole filling. A high resolution inelastic neutron scattering study was undertaken to determine the crystal electric field (CEF) spectra of Pr[123] and mixed Y/Pr[123]. A detailed theoretical analysis has determined that the true valence is Pr^{3+} and the reasons for the loss of superconductivity are considered in light of this. The refined CEF parameters are listed and are used to calculate both the magnetic susceptibility and specific heat of Pr[123].

Zn/Ga have been shown to substitute onto the Cu-O planes/chains of Y[123]. T_c reduces more rapidly with doping for Zn than for Ga. High resolution NMR was used to determine the changes in shift and relaxation time of the ^{89}Y resonance for a range of doping of each element. The two sets of data are in sharp contrast and the analysis of the results indicates that Zn doping on the planes produces fluctuating, localised magnetic moments which may be linked to the marked suppression of superconductivity.

INTRODUCTION

Since the initial discovery of High T_c Superconductivity in the La-Ba-Cu-O system (Bednorz and Müller 1986), the number of compounds which display it has risen greatly. This thesis is concerned with studies undertaken on only a few of these. The principal technique used was neutron scattering although the results of a nuclear magnetic resonance (NMR) experiment are also presented.

The common aim of the studies was to gather information about the underlying mechanism for superconductivity in these new materials. This mechanism is thought to be different from that of conventional superconductors (as discussed in Chapter 1) which are well described by the BCS theory (Bardeen et al 1957). There has thus been much theoretical speculation over the last four years as to its exact nature. Present theories can be put into three broad categories based on the proposed pairing mechanism:

(a) Phonon Models

(b) Electronic Models

(c) Magnetic Models

The relative merits of the various models are discussed in Chapter 1. No single theory can yet explain all the features of the new compounds and therefore the requirement for experimental evidence is paramount if any acceptable equivalent to BCS is to be formulated.

The materials studied were all pseudo-perovskites from two main groups: $Ln_{2-x}M_xCuO_{4-y}$ [214] (Ln = La for M = Ba, Ln = Nd for M = Ce) and $YBa_2Cu_3O_{7-\delta}$ [123] (with Pr doping on the Y site or with Zn/Ga doping on the Cu site). The former group consists of compounds with maximum superconducting transition temperatures (T_c's) in the region of 30K whereas for the latter the limit is just above 90K.

Common to all these compounds is some form of Cu-O plane structure. It is assumed that this attribute is essential for their superconductivity. Other features are also required and some of these may be peculiar to a given material. In 123, Cu-O chains are present and their influence (if any) on the properties of the superconducting and normal states is still unresolved.

The existence of the superconducting state has been shown to depend on oxygen stoichiometry (in certain cases) and the concentration and nature of dopants on the various sites. In 214 values of x near 0.15 give the maximum T_c for a particular dopant, M. For M=Sr, increasing x above 0.2 increases the oxygen vacancies and T_c is reduced. Tokura et al (1989b) have shown that the fall in T_c for high x (up to 0.4) is independent of the oxygen stoichiometry for samples annealed under pressure that have no oxygen vacancies. In 123 an oxygen deficiency, δ, as close to zero as possible is desirable. Substitution for Cu by other elements in increasing amounts lowers T_c. This may be a slight effect for some dopants (such as Ga) or extreme for others (especially Zn) — see for example Xiao et al (1988a). Not long after the discovery of 123 (Wu

et al 1987) it was found that replacement of Y by other rare earths did not destroy the superconductivity — in fact T_c changed by only a few degrees K (Hor et al 1987 and Maple et al 1987). There are three exceptions to this: Ce, Tb and Pr. The first two do not form the 123 phase (Le Page et al 1987 and Yang et al 1987); Pr does but the resulting material is a semiconductor. This lead to the study which forms Chapter 9.

There are other interesting features of these new superconductors (isotope effect, flux lattice etc.) which require further investigation. Not the least of these is the anomalous normal state (Anderson and Zou 1988); most marked by a linear temperature dependence of resistivity above T_c (Micnas et al 1987). Any satisfactory theory must therefore deal with both the superconducting and normal states. The formulation and testing of any such theory requires, for each high T_c compound, an accurate determination of the structural and magnetic phase diagrams, the band structure and a clear understanding of the local environment of the constituent atoms. Neutron scattering and NMR are both excellent tools for investigating solid state materials and a brief introduction to each will be given in later chapters (neutron scattering: Chapters 3,4 and 5, NMR: Chapter 6).

The wide interest in these compounds has in part been roused by the fact that on the whole they are relatively easy to fabricate as polycrystalline ceramics. This form is acceptable for most studies (especially if the crystallites in a sample can be aligned) even if single crystals would be preferred. This has allowed many researchers to

make valuable contributions to the field using quite common equipment. The methods used for each of the samples in this study are summarized in the relevant chapters. After preparation of samples it is essential to check the quality of the material and, where applicable, determine the value of T_c. Sample characterization techniques are explained in Chapter 2.

CHAPTER 1

HIGH Tc SUPERCONDUCTIVITY

Introduction

The initial discovery of superconductivity in Hg at 4K by Kammerlingh Onnes in 1911 has been followed by the continuing search for materials with higher T_c's. Progress up until 1986 was slow; the highest T_c being at about 23K in Nb_3Ge (Gaveler 1973). The breakthrough came with the discovery by Bednorz and Muller (1986) of a superconducting transition in the La-Ba-Cu-O [214] system. The T_c was confirmed by resistance and magnetic measurements to be near 30K. This was soon followed by the significant jump to T_c's above the boiling point of liquid nitrogen (77K) in the 90K superconductor $YBa_2Cu_3O_{7-\delta}$ [123] produced in 1987 (Wu et al 1987). In 1988 the trend continued with the discoveries in the Bi-Sr-Ca-Cu-O [BSCCO] (Chu et al 1988, Hazen et al 1988, Maeda et al 1988 and Wang et al 1988) and Tl-Ba-Ca-Cu-O [TBCCO] (Parkin et al 1988a, Parkin et al 1988b and Sheng et al 1988) compounds leaving the maximum recorded T_c to date near 125K in $Tl_2Ba_2Ca_2Cu_3O_{10}$.

Each new discovery has prompted research into many related compounds some of which have also been found to be superconducting. The terms "High T_c Superconductor" and "High Temperature Superconductor" are generally applied to the post 1986 oxide materials

which have T_c's above 20K. More recently they have been applied to some of the C_{60} fullerines — Cs_2RbC_{60} has a T_c of 33K (for a general review of these compounds see Prassides and Kroto 1992). There is however an argument for considering some of the pre 1986 oxide superconductors, such as Ba-Pb-Bi-O (T_c = 13K) as members of this group. This is based on the fact that these materials, besides having relatively high T_c's, have many other features in common with the new compounds such as structure and the density of carriers. They also do not exhibit normal BCS characteristics (Micnas et al 1990) — Ba-Pb-Bi-O is an extreme type II superconductor with a low density of carriers and a very short coherence length (these terms are defined below in § 1.1.1). It is thus conceivable that they all share a common, novel, superconducting mechanism. The possible nature of this mechanism is explored in section 1.2. Conventional (BCS) superconductivity is the subject of the next section.

Section 1.1 Conventional Superconductors

1.1.1 Basic Features

The phenomenon of superconductivity manifests itself by a transition of a material to a state of zero d.c. resistance at a characteristic temperature, T_c. It is mainly associated with metals and metallic compounds. The phase transition is second order; there is a sharp discontinuity in the specific heat and no latent heat. There is also an expulsion/exclusion of magnetic flux from the bulk of the material below T_c if a field is applied before/after cooling below T_c. The expulsion

is known as the Meissner effect. The exclusion results from shielding due to induced supercurrents at the surface.

The superconducting state can be destroyed by heating the material to a temperature above T_c, applying a magnetic field stronger than a characteristic strength, H_c (the critical field) or by passing an electrical current greater than a limiting value, I_c (the critical current). These parameters vary greatly between materials and samples. I_c is therefore normally not quoted but instead the critical current density, J_c, is used.

Superconductors are generally classified as belonging to one of two groups:

(a) Type I, in which there is a direct passage from the totally flux excluding state to the normal state as applied magnetic field is increased above H_c. This group includes all pure metal superconductors (excluding V and Nb).

(b) Type II, in which flux begins to penetrate the material above a certain magnitude (H_{c1}) but in which the normal state is not restored until a greater value (H_{c2}). Between H_{c1} and H_{c2} the material is said to be in the "mixed state": the flux is quantised and has a lattice structure.

T_c, H_c and J_c are not of course independent. H_c depends on temperature such that it is zero at T_c and tends to a constant value H_0 at $T=0$ approximately (in BCS theory — § 1.1.2) as:

$$H_c = H_0\left(1-\left(\frac{T}{T_c}\right)^2\right) \qquad (1.1)$$

Any current flowing in the material will have an associated magnetic field. If this field (plus any external field) exceeds H_c then the

superconductivity will be destroyed. J_c is thus defined in the absence of an external field.

Although flux will be excluded from the bulk of a sample of material in the superconducting state, there will be a region inside its surface in which the flux dies away. This can be modeled by an exponential decay with a characteristic distance known as the "penetration depth", λ.

The superconducting state has for a long time been envisaged as one of long range order with correlation between pairs of carriers (ie. electrons). The distance over which this holds is called the "coherence length",ξ. A fuller description of ξ is given in § 1.1.4 below.

1.1.2 BCS Theory

A very successful microscopic theory of superconductivity was put forward in 1957 by Bardeen, Cooper and Schrieffer (BCS). Only an outline will be given here and the interested reader is referred to the fuller introductions given elsewhere such as that of Tilley and Tilley (1990a). The theory builds on the earlier work of Cooper (1956) in which it was shown that two electrons could pair ("Cooper pair") through a net attraction resulting from the exchange of phonons. The binding energy of a Cooper pair is dependent on the Debye temperature of the phonons and on the electron - phonon coupling constant.

BCS theory considers the whole electron system using a simple model. The main points are given following the notation of Tilley and Tilley (1990a), which should he assumed to be the source unless otherwise stated. The pairing interaction takes place between two electrons initially in a state with wave vectors $\mathbf{k}$ and $\mathbf{k}'$ which

(exchanging a phonon) scatter into a new state $\mathbf{k}_1$ and $\mathbf{k}_1'$. This can only happen if the new states are available and thus electrons well inside the Fermi Sphere are forbidden from taking part by the Pauli exclusion principal. Pairing is therefore only considered near the Fermi Surface within an energy range determined by the Debye energy of the phonons ($\hbar\omega_D$, where ω_D is the Debye frequency). The interaction is strongest for electrons of equal and opposite momenta (ie. $\mathbf{k}' = -\mathbf{k}$). The wavefunction of the pair depends on $|\mathbf{k}|$, the magnitude of $\mathbf{k}$ and hence it is symmetric for exchange of positions but antisymmetric for the spins. The electrons in the pair therefore have opposite spin. The energy of the ground state (g.s.) is calculated using the variational principle. The construction of the g.s. wave function (Φ) assumes that a pair is either fully occupied (denoted by $|11\rangle$) with probability $|v_{\mathbf{k}}|^2$ or unoccupied ($|00\rangle$) with probability $|u_{\mathbf{k}}|^2$ ($v_{\mathbf{k}}$ and $u_{\mathbf{k}}$ are just the variational amplitudes). Thus :

$$\Phi = \prod_{\mathbf{k}} \psi_{\mathbf{k}} \tag{1.2}$$

where,

$$\psi_{\mathbf{k}} = u_{\mathbf{k}}^*|00\rangle + v_{\mathbf{k}}|11\rangle \tag{1.3}$$

($u_{\mathbf{k}}^*$, the complex conjugate of $u_{\mathbf{k}}$, is used by convention in the literature).

The Hamiltonian ($\mathbf{H}$) is constructed from the sum of kinetic and potential energy terms in the usual manner. The potential of a pair ($V_{\mathbf{k}\mathbf{k}'}$) in the simple model is just a constant: $V_{\mathbf{k}\mathbf{k}'} = -V$ for $|\varepsilon_{\mathbf{k}}|$ and $|\varepsilon_{\mathbf{k}'}| < \hbar\omega_D$, and zero otherwise. The expectation value of $\mathbf{H}$ is then minimized with respect to variations of $v_{\mathbf{k}}^*$.

Consideration of excited states shows that they must have at least some minimum energy, Δ, above the g.s. This is known as the "energy gap". Δ corresponds to a broken pair ($|10\rangle$ or $|01\rangle$) and is thus just the energy required to excite one electron.

It can be shown that for weak coupling ($N(0)V << 1$, where $N(0)$ is the density of states of energy at the Fermi surface):

$$\Delta = 2\hbar\omega_D \exp[-1/N(0)V] \tag{1.4}$$

It should be noted that in more complex models Δ may depend on $\mathbf{k}$, and that (1.4) only applies at $T = 0$ (where T is temperature in Kelvin). Excited states must be allowed for when considering temperature dependence of the interaction. In this case the free energy (F) rather than just $\mathbf{H}$ must be minimized. At T_c, by definition of the superconducting state, $\Delta = 0$ and it can be shown, again for weak coupling, that:

$$k_B T_c = 1.14\hbar\omega_D \exp[-1/N(0)V] \tag{1.5}$$

and thus, taking Δ from (1.4), at $T = 0$:

$$2\Delta = 3.52\, k_B T_c \tag{1.6}$$

where 2Δ can be taken as the energy required to excite a pair out of the g.s. and is the quantity normally measured by tunneling experiments. ("Weak coupling" can also be taken to be $T_c/\theta_D << 1$ where θ_D, the Debye temperature, is $\hbar\omega_D/k_B$ — this can be obtained from 1.5 if it is assumed that $N(0)V<<1$).

The BCS temperature variation of Δ (plotted as $\Delta(T)/\Delta(T=0)$ against T/T_c) is illustrated by Tilley and Tilley (1990f) and Rosenberg (1978). The

latter also compares this with the values obtained for Sn, Ta, Pb and Nb from electron tunneling experiments.

Equation (1.5) may be refined by taking into account the screened Coulomb potential (repulsive), V_c. Here (after Poole et al 1988) a Coulomb constant μ is defined, for the average Coulomb interaction $\langle V_c \rangle$, as:

$$\mu = N(0)\langle V_c \rangle \qquad (1.7a)$$

and the pseudo potential, μ^*, is :

$$\mu^* = \frac{\mu}{1 + \mu \ln(E_F/E_D)} \qquad (1.7b)$$

where E_F and E_D are the Fermi and Debye energies respectively.This is then subtracted from N(0)V in the denominators of (1.4) and (1.5), leaving (1.6) unchanged but modifying the estimates of Δ and T_c. ($\mu^* = 0.13$).

In the case of strong coupling and an anisotropic band gap the Eliashberg formulation (Eliashberg 1960) must be used. This deals explicitly with the electron - phonon coupling strength and averages it over the phonon density of states.

Another important prediction of BSC theory is the form of the energy (E) dependence of the density of states, N(E), for excitations above the ground state. At T=0:

$$N(E) = 0 \quad \text{for } |E| < |\Delta|$$

$$N(E) = \frac{N(0)E}{\sqrt{E^2 - |\Delta|^2}} \quad \text{for } |E| > |\Delta| \qquad (1.8)$$

(illustrated by Tilley and Tilley 1990a). There should thus be a noticeable difference between N(E) for a material in the superconducting state and

the same material in the normal state (where levels are available for single particle excitations with $|E| < |\Delta|$).

BCS theory explains the observed "isotope effect": the change in T_c of a material due to the substitution by isotopes (of different mass number, M). This empirically follows:

$$T_c \propto M^{-\alpha} \tag{1.9}$$

where $\alpha \leq 0.5$. In the simple model used to derive equation 1.5, V is a constant (independent of M) and hence this equation gives $T_c \propto \omega_D$. If the vibrating lattice is assumed to be a simple harmonic oscillator then the frequency of the vibrations (ω_D) is proportional to $(K/M)^{1/2}$. Assuming that the elastic constant (K) is the same for different M then $\omega_D \propto M^{-1/2}$ and hence $T_c \propto M^{-1/2}$ ($\alpha = 0.5$).

It also predicts: (i) that that the flux through a superconducting ring should be quantised in units of h/2e (= 2.07×10^{-15} Wb) and (ii) that the discontinuity in the electronic contribution to the specific heat (C) is (after Poole et al 1988):

$$\frac{C_s - C_n}{C_n} = 1.43 \tag{1.10}$$

where the subscripts s and n refer to the superconducting and normal states respectively.

1.1.3 The London equation

A straightforward approach to understanding the Meissner effect is to consider the London equation. This is a relationship between the electric current density (J_s), the macroscopic wavefunction of the

superconducting state (ψ) and **A**, the magnetic vector potential (after Tilley and Tilley 1990b):

$$\mathbf{J_e} = \frac{-2e^2}{m} |\psi|^2 \mathbf{A} \qquad (1.11)$$

(e and m are the usual electronic charge and mass) $|\psi|^2$ is equated to n_c, the density of Cooper pairs by the normalisation of ψ. It is simple to show (by taking the curl of (1.11) and replacing curl $\mathbf{J_e}$ using the curl of the Maxwell equation: curl $\mathbf{B} = \mu_0 \mathbf{J_e}$, remembering that curl curl = grad div - ∇^2,curl **A**=**B** and div **B** = 0) that:

$$\nabla^2 \mathbf{B} = \mathbf{B}/\lambda^2 \qquad (1.12)$$

where $\lambda^2 = m/2e^2\mu_0 n_c$. For a field parallel to a plane surface the solution is just:

$$\mathbf{B} = \mathbf{B}_0 \exp(-x/\lambda) \qquad (1.13)$$

where x is the distance below the surface and λ can be identified as the "penetration depth" of the field into the superconductor. As n_c falls to zero as T increases to T_c, then λ increases as T_c is approached. (λ can be extended to anisotropic materials by replacing it with a 2nd rank tensor).

1.1.4 Ginzburg-Landau theory

A thermodynamic approach to the superconducting state was taken by Ginzburg and Landau (GL) in 1950 which built upon the previous work of Landau on the theory of Second-Order phase transitions. The following is just a summary (after Tilley and Tilley 1990c).

Landau theory introduced an order parameter ϕ to characterise the transition from an ordered to a disordered state. It concentrated on

minimizing the Helmholtz free energy (F) in a small temperature region about T_c and demonstrates how F varies with ϕ over this range. For certain systems (including superconductors) it can be shown that F is minimum (F_{min}) for $\phi = 0$ and $T>T_c$. Below T_c $\phi = 0$ becomes a local maximum. F_{min} is found to occur at larger values of ϕ as T is further reduced.

GL theory assumes that the macroscopic superconducting wavefunction $\psi = \phi$. This means that ψ must now be complex and spatially varying (which allows for the inclusion of a kinetic energy term $\propto |\nabla\psi|^2$). It must also include the relationship between $\mathbf{J_e}$ and $\mathbf{B}$. A stable state for a superconductor in a magnetic field ($\mathbf{H_0}$) and at a given T is then found by minimizing the Gibbs free energy:

$$G(T,\mathbf{H_0}) = U - T\Sigma - \mathbf{H_0}\cdot\mathbf{M} \qquad (1.14)$$

where U is the internal energy, Σ is the entropy and $\mathbf{M}$ is the magnetization. (Note that H_0 is the applied field and not the total field (H) — the sum of H_0 and the field from supercurrents.)

It predicts the temperature dependence of λ (see § 1.1.3) near T_c to be:

$$\lambda \propto (1 - t)^{-1/2} \qquad (1.15)$$

where $t = T/T_c$. A more general version of this was given in the earlier "two fluid" model of superconductivity (Gorter and Casimir 1934a,b,c) in which:

$$\lambda \propto (1 - t^4)^{-1/2} \qquad (1.16)$$

This works well over a large range of T and reduces to (1.15) for $t \approx 1$.

The inclusion of $|\nabla\psi|^2$ in the free energy (see above) prevents ψ from changing quickly as this would cause the energy to rise. The coherence length ξ (which is also a function of temperature) is thus a characteristic distance over which changes can occur (its value is determined by a ratio of coefficients in the GL expression for the free energy). ξ in general must not be confused with another coherence length ξ_0. This is defined in a more general (less "local") form of the London equation, the Pippard equation, and can be identified as the radius of a Cooper pair. Pippard's equation applies well to pure metals but not to alloys where impurities sharply reduce the mean free path of carriers (l). ξ and ξ_0 are related by (after Tilley and Tilley 1990d):

$$\xi = 0.85\,(\xi_0 l)^{1/2}\left(\frac{T}{T - T_c}\right)^{1/2} \qquad (1.17)$$

Often the ratio $\lambda/\xi = \kappa$ (the "GL Parameter") is given as it is useful in the classification of type I/II superconductors. This stems from the fact that the G for a superconductor in a magnetic field must be minimized for the whole sample. Therefore in the mixed state, (type II) where there are superconducting (s) and normal (n) regions, the free energy in each region will be the same: $G_s = G_n$. However, near the boundary between two regions (s and n) G may fluctuate to give either positive or negative surface energy. This is due to:

(i) circulating currents in s causing G to increase — this effect is dominated by λ.

(ii) the increase in G due to (i) is cancelled over the bulk of the sample exactly by the decrease in G due to electron pairing — but this is dominated by ξ. When $\lambda > \xi$, G is initially reduced more rapidly, as s is

entered, than it rises due to circulating currents. The exact criteria for Type II is (after Tilley and Tilley 1990d):

$$\kappa > \frac{1}{\sqrt{2}} \tag{1.18}$$

In the next section various microscopic models for superconductivity in the new materials are discussed. It should be remembered however that thermodynamic approaches such as GL can still be very useful irrespective of the exact mechanism involved (see for example Bulaevskii et al 1988).

Section 1.2 High Tc Superconductors

1.2.1 Common Features

There are a number of distinguishing characteristics of the new high T_c superconductors which when taken together, make them both fascinating and difficult to deal with in a theoretical framework.

The most obvious of these is their range of high T_c's, which at the lower end is well within the maximum T_c predictions of conventional BCS theory (30 - 40 K) and which at the higher end (125 K) is far in excess. The estimates of a maximum T_c depend on the model used — a problem explored in depth by Carbotte (1990).

The most notable common crystallographic feature is the presence of two dimensional structures (usually Cu-O planes). This may in part explain why the normal state conductivity and the superconductivity are both anisotropic. In the normal state the

conductivity is greatest along directions parallel to the planes and in the superconducting state the coherence length (ξ) is longer parallel to the planes (see for example Friedel 1989 and references therein and also Kes 1992). A fairly complete structural review is given by Yvon and François (1989).

The existence of superconductivity tends to be sensitive to oxygen stoichiometry/dopant concentration, and all the compounds lie close to a metal - insulator transition. The formation of Cooper - type pairs has been indicated by flux quantisation measurements (for example Gough et al 1987) and tunnelling (Estève et al 1987). These appear to be strongly coupled as various gap measurements give large values of Δ (ie. Warren et al 1987, Imer et al 1989). Geerk et al (1988) have reported that the size of the gap (in Y123 —using tunnelling) is almost independent of temperature — unlike that of BCS theory (see § 1.1.2). These measurements are difficult to make without large single crystals and the main methods used are tunnelling, infra-red absorption and Raman scattering (see Tilley and Tilley 1990b for an explanation of the first two methods and 1990f for the last). A fuller comparison of various recent gap measurements and a discussion of the results is given by Tilley and Tilley (1990e). Strong coupling supports the short coherence lengths (~1 nm) measured in these compounds (Dinger et al 1987, Worthington et al 1987, Moodera 1988, Lea et al 1989) which, relative to the penetration depths give $\kappa >> 1$, ie. classifying them as extreme type II (see end of § 1.1.4).

An indication that phonons may not play the pre-eminent role they do in conventional superconductivity comes from the small isotope effects measured in these compounds (for a good review see Yosida et al 1988 and the references made there to previous reports). However, this

idea is based on the predictions of a BCS model which assumes three dimensions, weak coupling and phonon mediated coupling. The expected relationship between T_c and M is given by equation 1.9 as $T_c \propto M^{-\alpha}$ with α=0.5. For materials in which the first two assumptions may not hold, it is not obvious that the measured isotope effect should be as large as predicted by this model. Hence a small (or zero) isotope effect cannot alone rule out phonon mediated coupling. In fact the new compounds are not the first superconductors to depart from the expected α=0.5. Several elemental superconductors (Zr, Ru, Os and Mo) have values of α much lower than 0.5 and Ba-Pb-Bi-O (mentioned in the introduction to this chapter) has a value of α=0.25 (Pickett 1989). Friedel (1989) attempts to take account of the "quasi-two dimensional" character of these compounds whilst retaining phonon mediated coupling and concludes that smaller values of α are to be expected.

The apparently close link between antiferromagnetism, found in the insulating versions of the high T_c materials, and superconductivity has still to be resolved but it has inspired many theories (see § 1.2.4).

The normal state of these compounds is metallic — marked (in good samples) by a linear temperature dependence of resistance from T_c (well below θ_D) up to quite high temperature. This is seen as too wide a range by some (ie. Micnas et al 1987), but others feel that it may not be too difficult to explain (Civale and Martinez 1988).

Band structure calculations for the new materials also do not appear to support a conventional BCS phonon mediated mechanism. A quite complete review of the methods used to date and the results obtained are given by Pickett (1989).

NMR spin lattice relaxation time (see chapter 6) measurements in Y123 (Warren et al 1988) and BSCO phases (Howes 1992) indicate the onset of pairing may be above T_c; a phenomenon which is not predicted by BCS theory.

In the introduction the present microscopic theories were crudely grouped into (i) phonon, (ii) electronic, and (iii) magnetic models. This was done mainly to show the width of thinking on the topic. The reality of the situation is more complex as there are overlaps between groups (in which the coexistence of mechanisms is envisaged), there are also various refinements (to some of the basic ideas) which fit into different groups, and there are exotic theories which fit into none. The following sections will therefore present the "basic ideas" and mention some of the experimental evidence for/against the resulting theories where appropriate. They will also serve, for the "uninitiated", as an introduction to some of the terminology used in the literature.

1.2.2 BCS Type Models

These all rely on phonon mediated pairing. There is a case for the new high T_c's being explained using only conventional weak coupling BCS which is argued well by Friedel — he takes "a conservative view" of the problem. His review article (1989) is extensive (giving over 300 references) and is recommended to any reader who thought that BCS had gone out of fashion. The only refinement to the theory he sees as necessary is to take into account the two dimensionality of the new materials.

There is evidence from Infra Red and Raman studies that the electron - phonon coupling is strong (see Pickett 1989 and references

therein). Attempts have been made to use a standard strong - coupling (Eliashberg) formulation in three dimensions to account for the observed small isotope effects and the high T_c's. These may work at the lower end of the T_c range but cannot predict T_c's ~90 K (Barbee et al 1988). Some success has been claimed using two dimensional models (Zacher 1987, Labbé and Bok 1987). Full details of Eliashberg theory estimates of maximum T_c values are given by Carbotte (1990).

When the magnetic ordering and fluctuations are also brought in there exists the possibility of heavy fermion superconductors and spin triplet pairing (p-wave: spins parallel — rather than s-wave: spins antiparallel (BCS)) by analogy with liquid ^{3}He. This is discussed by Tilley and Tilley (1990e) who also give a good introduction to the basic theories of Fermi liquids, spin triplets, and heavy fermion superconductivity. A fuller review of the latter (as applied to the new materials and other systems) is given by Fulde et al (1988). Some heavy fermion models retain phonons (to become extensions of BCS theory) whilst others rely on purely electronic mechanisms for pairing. The name "heavy fermion" is invoked because the interactions result in an electron (or other "quasi-particle") effective mass hundreds of times that of a free electron.

Very strong electron - phonon coupling results in the formation of polarons and the breakdown of the adiabatic approximation of BCS theory (ie. that the lattice cannot respond rapidly to the electron motions). When the coupling is so strong that the lattice responds instantaneously to the electron motions it is said to be in the "anti-adiabatic limit". This is dealt with in the next section.

1.2.3 Local Pairing

Many different microscopic models have at their core the idea of "local pairing" as opposed to the extended (in real space) Cooper pairs. This results from strong electron coupling to a "bosonic field" (see Micnas et al 1990). The interactions of the electrons with this field (polarization/distortion) results in the formation of new "quasi-particles pairs". The bosonic excitations may be phonons, excitons, plasmons, polarons or solitons etc.). Phonon types are applicable to heavy fermion systems as mentioned above.

A polaron also arises due to the electron - phonon interaction. In this case it is the name given to the electron (or hole) and its associated cloud of lattice polarization and distortion. Polarons can be classified as "small" or "large" depending on the degree of carrier localization. The former are more applicable to local pairing theories (see Micnas et al 1990 and Fisher et al 1989 (definition of polaron types)). The distortions of the lattice linked to polarons can result in an attractive interaction between them which may cause them to pair — forming a "bipolaron". If the binding energy of the bipolaron is not too large (ie. small compared to the band width) then the effective polaron - polaron interaction is treated like the BCS effective electron - electron interaction. In this case however all the states contribute to the superconductivity; not just the band within E_D (the Debye energy) of E_F as in BCS. This is called "polaronic" superconductivity (after Alexandrov 1983). When the binding energy is large the bipolarons behave like bosons which condense into a superfluid state at low temperature. These "bipolaronic" superconductors would show a decrease in T_c as the binding energy (and effective mass) is increased and, at a simple level, predict no band

gap. Many of the high T_c theories predict maximum T_c's at the change over between the polaronic and bipolaronic regimes (where the calculations are most difficult!). The observation of a band gap is a difficulty for these models but attempts have been made to explain it — ie. with the inclusion of charge density waves (CDW) (Fisher et al 1989).

The Jahn Teller effect (Jahn Teller 1937) has also been invoked to deal with the high T_c compounds. This is just the distortion of a lattice which lowers the total energy and symmetry by removing orbital degeneracy. An excitation formed by a charge carrier plus such a distortion is called a Jahn - Teller polaron and is a type of soliton — ie. a wave which retains its shape throughout interactions in a medium (Fisher 1989, Pickett 1989, Poole et al 1988). The increased energy available for this effect results in tightly bound bipolarons in the superconducting ("superfluid") state (de Jongh 1988).

The motivation for considering non - phonon pairing mechanisms comes from a consideration of equation (1.5). If the Debye energy ($\hbar\omega_D$) is replaced by higher value, such as that which would result from a different mediator, then T_c is increased accordingly. An "exciton" (or "plasmon") is just a charge carrier plus an associated lattice polarization cloud. Interactions between excitons can be attractive and lead to pairing. Exciton energies (~2 eV) are about 40 times bigger than typical Debye energies and this makes them ideal for raising T_c's (Phillips 1989a, Poole et al 1988, Ruvalds 1988). Y123 provides a fertile candidate for exciton theories in which charge carries in the planes couple to polarization of the chains (Freeman et al 1988).

Some of the important general predictions of local pairing which fit the new compounds, (after Micnas et al 1990) regardless of the mechanism for pairing, are:

(a) Extreme type II superconductivity — indicating that all the charge carries are involved.

(b) Superconductivity in multiphase samples — analogous to superfluidity in a porous medium.

(c) Indications from NMR measurements of pairing above T_c (as mentioned in § 1.2.1).

Other NMR evidence (ie. a Knight Shift (see chapter 6) which disappears below T_c and in insulating phases — as would be expected when conduction electrons are not available) is interpreted by Friedel as showing that the "pairs" are fermions and thus no kind of superfluid boson condensate can be the high T_c state (Friedel 1989). A full account of local pairing in various systems (esp. the high T_c materials) is given in the review by Micnas et al (1990). This also explains another pairing mechanisms (ie. "dangling bonds").

1.2.4 Magnetic Models

The intimate relationship between magnetism and the new superconductors has sparked interest in a number of "magnetic" theories. One which has gained much support is the Resonating Valence Bond (RVB) model originally proposed by Anderson (1987). It also, in part, helps to explain why Cu seems so important for high T_c's — many of the theories discussed above are not specific and imply that

any transition metal could be used in place of Cu. To see this consider a main feature of the new materials; the Cu-O planes:

In a two dimensional Cu-O plane network the Cu 3d orbitals hybridize with the O 2p leading to σ antibonding bands. If the bands are fitted in a tight binding approximation then $E_{3d}(Cu) = E_{2p}(O)$ (within 0.2 eV). This is known as the Mattheiss Relation (Phillips 1989a) and may be the reason why Cu is special in such a network. If all the Cu is 2+ then antiferromagnetic ordering is favoured (neighbouring spins antiparallel). The spins become localized (at each Cu site) if it is energetically unfavourable to form Cu 1+ or Cu 3+ (ie. for a carrier to jump to the next site) — this is called a Mott insulator, and results purely from the strong binding of the charge carriers to the lattice.

In the RVB g.s. the antiferromagnetic order is lost and spins on neighbouring sites are paired as "spin singlets" (called "dimerization") in all possible combinations in a disordered fashion. As it is equally probable that the singlet may be in $|\downarrow\uparrow>$ or in $|\uparrow\downarrow>$ (with no net spin) no spin may be assigned to either site and the singlets are bosons. The g.s. is thus a liquid condensate of bosons. The fundamental excitations of this state are the two kinds of solitons which result from the separation of charge and spin degrees of freedom (Anderson and Zou 1987): "holons" (charged bosons) and "spinons" (neutral fermions). The "resonating valence" of the RVB model concerns the charge transfers of the holons allowing oscillation of Cu valence between 1+ and 3+.

There are other <u>non-resonant</u> magnetic models which rely on spin density waves (SDW) originally proposed by Schrieffer et al (1988). They use an extended Hubbard model in a weak coupling (electron - phonon) regime with a nested Fermi surface (see for example Nago et al

1990). The superconductivity results from fluctuations induced by the SDW. Fermi surface "nesting" occurs when large areas of the Fermi surface are nearly parallel and results in soft (nearly zero frequency) phonons (Phillips 1989a). The Hubbard model (Hubbard 1963, 1964) describes magnetic energies between tightly bound electrons, on the same site, using only two parameters: U for the intrasite attraction, and t for the transfer energy (one electron band width or "electron hopping amplitude") (Phillips 1989a). This has been extended by others (see Micnas et al 1990 and references therein) to include W, the intersite interaction. Localized pairing can result when the intrasite attraction (negative U) dominates the the intersite repulsion (positive W). This is often quoted as a "negative - U Hubbard model" and is used by many local pairing theories to produce a superconducting state as discussed in § 1.2.3. Other Effective Hamiltons are suggested by Sigmund and Stevens (1988) for use with the high T_c compounds.

1.2.5 Discussion

It is impossible to deal with all proposed models ("fractons" for instance have not been considered — see Poole et al 1988) or to do justice to any in a limited space.

Although there is evidence from Infra Red, optical spectra etc.(Poole et al 1988) for excitons and plasmons it is not clear if they are really the main mechanism for superconductivity or just co-exist with it.

Magnetic models may have problems explaining the lack of any unusual magnetism in the Bizmuthates (Phillips 1989a) which pre-date the present compounds (see the Introduction to this chapter). The RVB model assumes and solves the problem of coexistence of the superconducting, metallic and antiferromagnetic states — a problem

which may not exist. In fact, considering the phase diagrams the antiferromagnetic state appears to be detrimental to superconductivity. Picket (1989) also sees the existence of Cu 3+ as very doubtful.

The situation at present is that most models seem to be able to explain most of the experimental evidence given sufficient "adaptation". The problem is neatly summarized in three quotations:

"Despite the underlying mechanism the possible unifying phenomenological model is superfluidity of charged bosons ..."(Micnas et al 1990).

" ... the carriers which condense in Cooper pairs are fermions. It rules out superfluidity by condensation of bosons ..." (Friedel 1989).

" ... there is no room to doubt that it is lattice instabilities and not magnetism that produce high T_c superconductivity just as much in the cuprates as in the intermetalic compounds." (Phillips 1989b).

CHAPTER 2

CHARACTERISATION OF SAMPLES

Introduction

It is essential when preparing the high T_c superconductors to ensure that the intended phase has formed and that there are minimal amounts of any secondary phases. Furthermore, if a superconductor was the expected result, T_c must be determined and the superconductivity shown to be from the bulk of the sample. There exist a number of standard techniques which can be employed for characterisation of these samples. The simplest test for the 90K [123] compounds is to check for diamagnetism by cooling the sample in liquid nitrogen and attempting to float a small magnet above it (or some other variation on the same theme). Whilst this proves to be a fascinating demonstration it at best provides qualitative information on the superconducting sample and is of no use for non-superconducting related compounds. X-Ray powder diffraction on the other hand can be used on all samples. It provides the required information with regards to phase purity and can in principal (although not in these studies) be used for the determination of structure. T_c can be quantified using resistivity, magnetic susceptibility or specific heat measurements. Thermogravometric analysis (TGA) can be employed for determination of oxygen content and for optimising processing conditions.

The following sections deal with the main techniques used to characterize samples in this study: X-ray diffraction, D.C. resistance and A.C. magnetic susceptibility.

Section 2.1 X-ray Diffraction

X-ray powder diffraction was carried out at room temperature using a Phillips PW 2273/20 diffractometer with graphite monochromator for Cu Kα radiation. Each sample was prepared by smearing silicone grease on $^1/_3$ of a glass slide and then mixing in roughly 100mg of fine ground powder from the material to be studied. The mixing, and final smoothing of the surface of the slurry, was done using a second slide. 2θ scans were performed over a variety of ranges, step intervals and counting times. For a general check on sample phase purity 5° to 70° with 0.05° steps counting for 6 sec/step was found to be adequate. Shorter scans over reduced ranges with longer count times were used when looking for the main peaks of particular secondary phases at intermediate stages of sample preparation. The silicone grease contributed only a broad featureless background which was most intense at low angles ($2\theta < 10^\circ$) and thus did not interfere with the interpretation of patterns.

The data were stored using a computer which also controlled the diffractometer. Peak positions were converted to d-spacing for comparison with published data using Bragg's Law:

$$2d \sin\theta = \lambda \qquad (2.1)$$

where d is the interplanar spacing, 2θ the angle of diffraction and λ is the wavelength (in this case $\lambda = 0.1542$ nm). A typical diffraction pattern is shown in figure 2.1 for a sample of Y123.

X-ray diffraction is a very widely used tool for structural studies and many useful guides have been published. One which covers all aspects in some depth is that by Klug and Alexander (1974).

Section 2.2 D.C. Resistance

The resistance of samples over the temperature range 4 - 300K was determined by the standard four terminal technique in an Oxford Instruments helium gas flow cryostat. A small bar (roughly $1mm^2$ x 5mm) was cut from the sintered pellet of each sample and was mounted on a specially designed printed circuit board (PCB) using shellac as an adhesive. Four electrical contacts were made to the sample from copper tracks on the PCB with conductive silver paint (see figure 2.2). The PCB was fixed to a copper block at the end of the cryostat sample stick and four leads (a pair for both voltage and current) were soldered on. Dry helium (boil-off) gas, at reduced pressure (~30 kPa), was used as a heat exchange medium in the cryostat sample space.

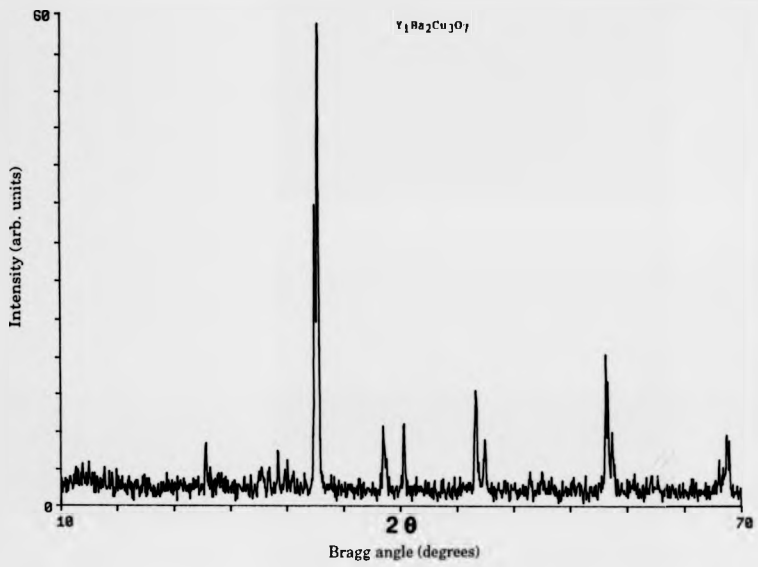

Figure 2.1 X-ray powder diffraction pattern of Y123.

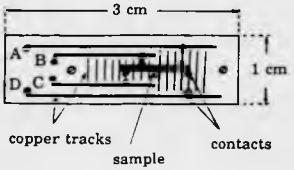

Figure 2.2 PCB used for resistance measurements showing sample position and contacts.

Resistivity measurements were controlled using an Apricot microcomputer via an IEEE bus. Current was supplied from a Keithley 244 constant current source, and the voltage dropped across the sample was read from a Keithley 184 nanovoltmeter. Sample temperature was measured using a calibrated gold-iron:chromel thermocouple monitored by a Phillips multimeter. Resistance was calculated from the average of 30 voltmeter measurements (15 for each of the two current directions) with a fixed current magnitude. The current was reversed so as to eliminate any thermal emf's (at the contacts or leads) from the calculation of sample resistance.

The onset of the superconducting transition was defined to be the point at which the resistance deviated from the extrapolated high temperature behaviour (see figure 2.3). T_c was taken to be the temperature at which the resistance had fallen to half the onset value. The width of the transition, ΔT_c, was defined to be the temperature difference between 10% and 90% of the onset resistance.

Section 2.3 A.C. Magnetic Susceptibility

As explained in chapter 1, when a superconductor is cooled below its transition temperature it becomes diamagnetic. This can be exploited by susceptibility measurements not only for determining T_c but also for quantifying the fraction of superconducting phase present.

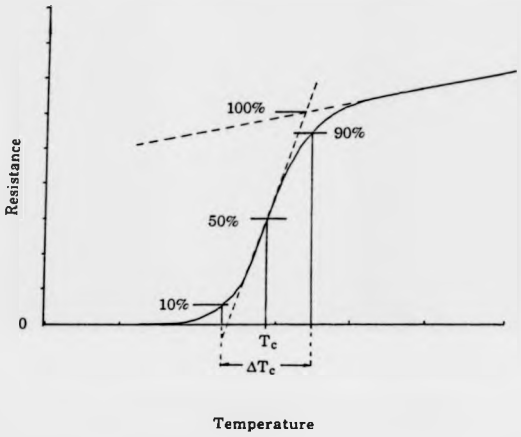

Figure 2.3 Convention for T_c and ΔT_c measurements.

For these measurements the same gas flow cryostat was employed as that for d.c. resistance (section 2.2). A separate probe was constructed with a system of coils at the lower end as shown in figure 2.4. An a.c. voltage of 1v at 86.4 Hz was supplied to the primary coil from an EG&G Princeton Applied Research two phase lock-in analyzer (PSD). The difference of the induced voltages in the two secondary coils was measured on the PSD with the phase set to give χ' and χ'' on separate channels. Samples were normally fine powders (100-200mg) although for quick checks of a sample small lumps were often used. These were contained in standard 5mm (dia.) quartz NMR tubes screwed to the end of a thin walled stainless steel tube. This allowed samples to be changed without removing the coil assembly from the cryostat. Temperature at the sample position was monitored using a calibrated Southampton miniature diode (calibration: better than ±0.1K in the temperature range of interest) supplied with 10μA constant current. As in the resistance measurements data were collected on an Apricot microcomputer.

It was noticed that the measured signal was sensitive to any rapid changes in cooling/heating rate and that marked hysteresis occurred when these rates were too high. The former problem is believed to result from changes in the temperature gradient between the two secondary coils whereas the latter is assumed to be caused by the necessarily poor thermal contact between the coil system (where temperature was measured) and the sample. Acceptable results were obtained by heating at a constant rate of 0.2 $Kmin^{-1}$ (or less) from well below T_c. At this rate any hysteresis was found to be negligible (< 0.5 K).

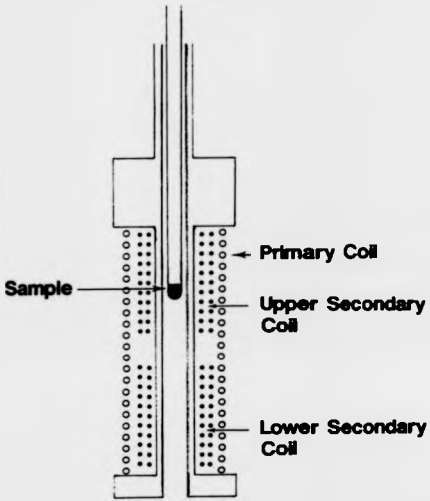

Figure 2.4 Schematic layout of coils on the a.c. magnetic susceptibility probe.

Recently Chen et al (1990) have investigated the problems involved in making quantitative measurements of a.c. susceptibility in the High-T_c Superconductors. They compare samples from both cut sintered pellets and ground powders. The relevance of weak link models to explain the low J_c is discussed and they propose a "grain-cluster" model. In the present study the a.c. susceptibility measurements were used primarily to determine Tc and to monitor sample quality — a "good" sample has a single sharp transition associated with a large change in susceptibility.

CHAPTER 3

NEUTRON SCATTERING

Introduction

Neutron Scattering is of major importance when investigating matter on the atomic scale. This results from a number of useful properties of the neutron:

(a) it interacts only weakly with matter making it a good probe of the bulk of a sample and allowing the interaction to be treated correctly as a first order perturbation on the system being studied (Williams and Lovesey 1989);

(b) available neutron energies and wavelengths are of the same orders of magnitude as the characteristic energies and amplitudes of atomic motions in solids;

(c) the neutron possesses a magnetic moment which allows for investigations of magnetic order and crystal fields in suitable samples.

The scattering can be separated into two broad categories: elastic and inelastic. Elastic scattering is the concern of diffraction experiments which are invaluable for the determination of crystal structures. Inelastic scattering, where energy is transferred between the neutron and the sample, provides details of the energy spectrum in crystalline

materials. Magnetic scattering may occur in both cases. Magnetically ordered structures can give rise to additional intensity/peaks in diffraction patterns which allows the nature of the ordering to be determined in an analogous way to crystal structure. The crystal electric field in the vicinity of a magnetic ion lowers the degeneracy of the magnetic ground state. Neutrons can be used to investigate the splitting of the ground state multiplet and transitions to higher states.

This chapter will outline the basic principles common to all neutron scattering experiments (section 3.1). It will deal with practical details of just one technique, Time of Flight (TOF) measurements (section 3.2), as the results reported in this study were all obtained using TOF machines. Specific details of diffraction and inelastic methods and the instruments involved will be given in the following chapters (4 and 5 respectively).

Section 3.1 Neutron Scattering Cross Sections

The aim of a neutron scattering experiment is to measure the scattering probabilities or cross sections as a function of scattering vector **Q** and energy transfer $\hbar\omega$.

$$\mathbf{Q} = \mathbf{k} - \mathbf{k}' \qquad (3.1)$$

where $\mathbf{k}$ and $\mathbf{k}'$ are the incident and outgoing neutron wave vectors respectively. The energy transferred to the sample is given by:

$$\hbar\omega = \frac{\hbar^2}{2m}(k^2 - k'^2) \qquad (3.2)$$

where m is the neutron mass and $k = |\mathbf{k}|$ etc. If the neutron gains energy then $\hbar\omega$ is negative (called 'neutron energy gain"). This is the normal convention for neutron experiments.

Neutrons are removed from the incident beam by two processes: absorption and scattering. The former is generally undesirable as it prevents neutrons reaching the detectors. It is significant however, provided the sample is thin enough, only for certain elements (B, Cd, Gd etc.) and even then the problem is often overcome by substitution with a less absorbing isotope. The latter process provides the neutrons of interest — those which have interacted with the sample but have emerged with a possibility of being detected.

The ability of an element to absorb/scatter neutrons, its "cross section"(σ), is given the dimensions of area. The commonly used unit is the barn ($1b = 10^{-28}$ m^2). The cross section can be related to a quantity equivalent to a "radius" for the interaction called the "scattering length"(b) (Gunn 1988) as:

$$\sigma = 4\pi b^2 \qquad (3.3)$$

It is also just the sum of the absorption (σ_a) and scattering (σ_s) cross sections:

$$\sigma = \sigma_a + \sigma_s \qquad (3.4)$$

The information gained from measuring σ is limited and it is more useful to measure the angular dependence of the scattering into

some solid angle $d\Omega$. This is defined as the differential cross section (d.c.s):

$$\frac{d\sigma}{d\Omega}(\theta,\phi) = \frac{\text{no. of neutrons scattered into } d\Omega/\text{sec}}{I_0 \times d\Omega} \qquad (3.5)$$

Where I_0 is the incident neutron flux, and θ and ϕ are the usual polar angles ("(θ,ϕ)" is usually inferred and therefore omitted). The d.c.s is ideal for elastic experiments as they assume no change in neutron energy. It is in fact an integral of the partial differential cross section (p.d.c.s.) over scattered energy — see below.

Where a full analysis of the scattering is required the partial differential cross section (p.d.c.s) is defined. It is similar to the d.c.s but with the additional proviso that the neutrons scattered into $d\Omega$ also have a final energy (E') in a range dE':

$$\frac{d^2\sigma}{d\Omega dE'} = \frac{\text{no. into } d\Omega/\text{sec with energy } E' \text{ to } E'+dE'}{I_0 \times d\Omega \times dE'} \qquad (3.6)$$

At this point it is useful to define the "scattering function" (or "scattering law" or "dynamic structure factor"), $S(\mathbf{Q},\omega)$ which is related to the p.d.c.s by :

$$\frac{d^2\sigma}{d\Omega dE'} = \frac{k'}{k} S(\mathbf{Q},\omega) \qquad (3.7)$$

This neatly separates the valuable information from the sample (held in $S(\mathbf{Q},\omega)$) from the details of the neutron motion (k'/k). The type of scattering interaction determines the form of $S(\mathbf{Q},\omega)$ such that it is large for those points in $\mathbf{Q},\omega$ space at which the neutron initiates/absorbs characteristic excitations of the crystal (ie. phonon or magnon). Whilst the transition probability from one state to a higher state must be the same as for the reverse transition, the higher state will be less populated

according to $\exp(-\hbar\omega/k_BT)$,the Boltzmann factor. This is taken into account by the principal of Detailed Balance which gives:

$$S(-\mathbf{Q},-\omega) = \exp(-\hbar\omega/k_BT)\, S(\mathbf{Q},\omega) \qquad (3.8)$$

Most systems studied have a centre of symmetry and thus :

$$S(-\mathbf{Q},\omega) = S(\mathbf{Q},\omega) \qquad (3.9)$$

Hence detailed balance considerations need only apply to energy loss/gain. In practice other terms are taken out of this "$S(\mathbf{Q},\omega)$" — constants, form factor etc. — to give a more restricted version. The importance of $S(\mathbf{Q},\omega)$, especially for magnetic inelastic scattering, is discussed further in chapter 5.

Section 3.2 Measurement of a Time of Flight (TOF) Spectrum

TOF measurements can be made using neutrons from any source as all that is required is a well defined pulsed beam. A reactor provides a continuous polychromatic beam which can be converted to a monochromatic pulsed beam by means one or more rotating choppers. The beam from a spallation source (where neutrons are produced by striking a target with a beam of protons) is intrinsically pulsed, as explained below, but it is polychromatic and of very high energy (of the order of 100's of MeV). It must therefore be moderated to the energy range required for neutron scattering experiments (to the order of 10's - 100's of meV) and may also be made monochromatic using a chopper as required. The pulsed nature of the beam is due to the method of obtaining the proton beam. A linear accelerator injects H- ions into a

synchrotron ring through a stripper foil which removes the two electrons (per ion) to give bare protons. These protons are accelerated for a short time (the acceleration cycle) to the desired proton energy. During the acceleration cycle the strength of the magnetic field in the ring is gradually increased to keep the beam radius constant. The protons are then extracted (by a magnet) down a beam line that ends at the target. The higher the proton energy, the higher the neutron yield. The process is continually repeated to give a stream of proton pulses with a repetition rate which depends on the length of the acceleration cycle.

All TOF data reported in this thesis were collected at the spallation source ISIS, Rutherford Appleton Laboratory, UK (see figure 3.1). The neutron pulse is initiated by the impact, on a depleted ^{238}U target, of a short (~400 ns) pulse of 800 MeV protons extracted from a synchrotron. A number of different moderators are then used with the aim of maximizing the flux, whilst retaining a sufficiently narrow pulse (1 to 100 μs), for the individual spectrometers. The average pulsing frequency is 50 Hz. A fuller description of ISIS is given by Williams and Lovesey (1989).

In a given spectrometer the energy (E)/wavelength (λ) of neutrons arriving at the detectors is determined by measuring the time taken (T) for the neutrons to traverse a known flight path (L) as:

$$E = \frac{m}{2}\left(\frac{L}{T}\right)^2 \qquad (3.10)$$

where m is the neutron mass, and using the de Broglie relation:

$$\lambda = \frac{h}{m}\left(\frac{T}{L}\right) \qquad (3.11)$$

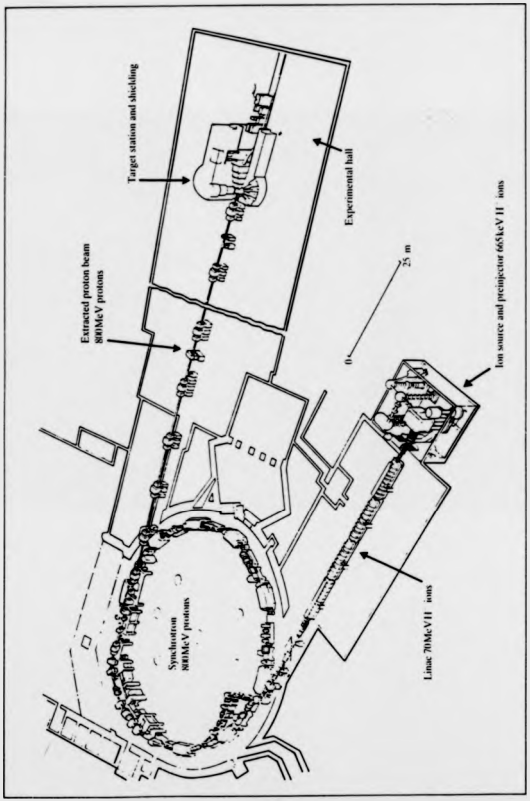

Figure 3.1 Schematic layout of the ISIS pulsed neutron source, Rutherford Appleton Laboratory.

The exact details of the flight path depend on the type of instrument but the start (at T=0) is taken to be origin of the pulse in the moderator. Resolution is thus limited in the first instance by the uncertainties in L and T (ie. exactly where and when the pulse was born in the moderator).

Each spectra is recorded by dividing the acquisition into frames of fixed duration and synchronizing these with the pulse. Neutrons which strike the detectors are only counted if they have a TOF inside the frame limits (the lower limit may be T > 0). Each detector is regarded as an array of elements of finite area which subtend solid angles at the sample position. The time of arrival of each neutron is recorded for the individual elements. The time can only be measured to a finite precision so the neutron counts are considered to be "binned" into small time elements (~ 1 μs). Thus the basic TOF spectrum consists of neutron counts over a specified TOF range for each element (which has a known position relative to the sample). It is common to group detector elements so as to suit the type of experiment. For example in powder diffraction, where only the Bragg angle is required (see chapter 4), elements which all lie at the same angle to the unscattered beam may be grouped (such that they form a ring — ie. the intersection of the detectors with the Debye-Scherrer cone).

Elastic experiments assume no change of neutron energy and thus the wavelengths of the recorded neutrons are found according to (3.11). Inelastic experiments use a monochromatic beam which allows neutron energy transfer to be calculated according to (3.10).

An accurate determination of the p.d.c.s. (or just the d.c.s. for elastic scattering) requires that certain corrections be made to the measured spectra. The number of counts registered by the detector

elements does not equal the number of neutrons scattered once by the sample, which are the ones of interest. They will also detect neutrons scattered from the sample container (sample can, cryostat, etc.), those scattered more than once by the sample (multiple scattering), radiation from the neutron source — but not the incident beam ("source on"), electronic noise and external radiation such as cosmic rays ("source off").

Normally instrument shielding renders the "source on/off" contributions negligible but even when this is not the case they only tend to add a flat background. The contribution from the sample container can be quite significant. It can be determined, however, by repeating the experiment with the can empty and also with the sample replaced by a strong neutron absorber (ie. Cadmium or Boron Nitride). The container is then considered in two parts: C1, that which scatters the beam directly; C2, that which scatters the beam after it has passed through the sample (and is thus reduced in intensity by a factor equal to the sample transmission (α)). The run with the neutron absorber (AR) will produce scattering only from C1 (assuming zero transmission). The empty can run (ER) gives the total scattering from C1 and C2. The sample run (SR) will have an intensity I_{SR} which is expressed as:

$$I_{SR} = I_S + I_{C1} + \alpha I_{C2} \tag{3.12}$$

where I_S, I_{C1} and I_{C2} are the intensities from the sample and the two container regions. Note that $I_{C1} = I_{AR}$ and I_{C2} is found from:

$$I_{C2} = I_{ER} - I_{AR} \tag{3.13}$$

Thus combining 3.12 and 3.13 the sample only scattering is just:

$$I_S = I_{SR} - I_{AR} - \alpha (I_{ER} - I_{AR}) \tag{3.14a}$$

or:

$$I_S = I_{SR} - \alpha I_{ER} - (1+\alpha) I_{AR} \qquad (3.14b)$$

Multiple scattering is more difficult to allow for but it can be minimized by careful experimental design. Given that it is not significant, I_S as given above represents the rate of detection of neutrons which have been scattered once by the sample. Two more corrections must be applied to find the actual rate of scattering by the sample. Firstly scattering occurs over the entire sample: not just at a single point. Any neutron entering the sample may thus be absorbed before being scattered. If it survives and is scattered it has a certain probability (<1) of exiting without absorption and further scattering. This is all determined by the average number of atoms per unit volume, the average cross section for the atoms, the sample geometry and the neutron energy. It is expressed in the "absorption and self shielding factor" which for most sample shapes can only be calculated numerically. Secondly the count rate of the detector must be corrected for its efficiency (always <100%), which is a function of energy.

The detector efficiency and any other instrument dependent parameters (which may be functions of monitor efficiency or beam intensity profile for example) can be found from a spectrometer calibration run. For this a standard scatterer replaces the sample and the experiment is repeated. Normally Vanadium is used as its scattering is virtually all elastic, isotropic and incoherent. Its d.c.s (before any absorption or multiple scattering corrections) is simply:

$$\frac{d\sigma}{d\Omega} = \frac{\sigma_{inc}}{4\pi} \qquad (3.15)$$

Where σ_{inc} is the incoherent scattering cross section for vanadium (σ_{inc} = 4.98 b/atom compared to a coherent cross section, σ_{coh} = 0.02 b/atom).

It should also be remembered that detector efficiency is a function of the neutron energy and also depends on the type of detector. It is thus possible to obtain this parameter from the relevant tables which have been calculated for different detector types at various energies (see Windsor 1981).

CHAPTER 4

NEUTRON DIFFRACTION

Introduction

Diffraction techniques are vital to crystallography and are most valuable when used in the study of single crystals. They are also applied to polycrystalline powders of most materials with success. This is the case when the full information contained in a single crystal study is not required or when sufficiently large crystals cannot be grown. An example of the former case is given in chapter 2 where it is explained how X-ray powder diffraction can be used for checking sample quality during and after processing. The latter case applies to the neutron diffraction work presented in this thesis.

The main draw-back of powder diffraction is the loss of the three dimensional information contained in single crystal studies. In a powder diffraction spectrum peaks arise only as a function of inter-planar spacing (d-spacing) and may thus represent the combined intensities of Bragg reflections with different sets of Miller indices. A relevant example of this is Pr-123 (chapter 9) which is tetragonal with 3a = c. As a result, the principal (XRD) peak contains the (1 1 0), (1 0 3) and (0 1 3) reflections. The main advances in powder diffraction have thus been in the increased resolution of instruments (to separate closely

spaced peaks) and in the improvement of analytical techniques such as Rietveld profile refinement (section 4.3).

All the neutron diffraction data in this study were collected on the High Resolution Powder Diffractometer (HRPD) at ISIS (see figure 4.1) and thus the rest of this chapter will deal specifically with this instrument. Magnetic neutron diffraction, although possible on HRPD, will not be discussed as it is not relevant to the work done.

Section 4.1 Collection of Spectra

HRPD is a TOF spectrometer which obtains its high resolution ($\Delta d/d \sim 4 \times 10^{-4}$) principally from the length of its flight-path (~100m). It can be shown (Williams and Lovesey 1989) that the resolution is:

$$\frac{\Delta d}{d} = \left(\left(\frac{\Delta T}{T} \right)^2 + (\cot \theta \, \Delta\theta)^2 \right)^{1/2} \qquad (4.1)$$

where T is the total TOF and θ is the Bragg angle.The uncertainties ΔT and $\Delta\theta$ arise from moderation time of the neutron and the beam divergence respectively. For back-scattering ($\theta = 90°$) this reduces to:

$$\frac{\Delta d}{d} \sim \frac{\Delta T}{T} \qquad (4.2)$$

T is related to the length (L) of the flightpath and the neutron wavelength (λ) by equation (3.11). Thus for a given λ :

$$\frac{\Delta T}{T} = \frac{\Delta L}{L} \qquad (4.3)$$

where $\Delta L \sim 0.04$ m for HRPD; hence its long flightpath.

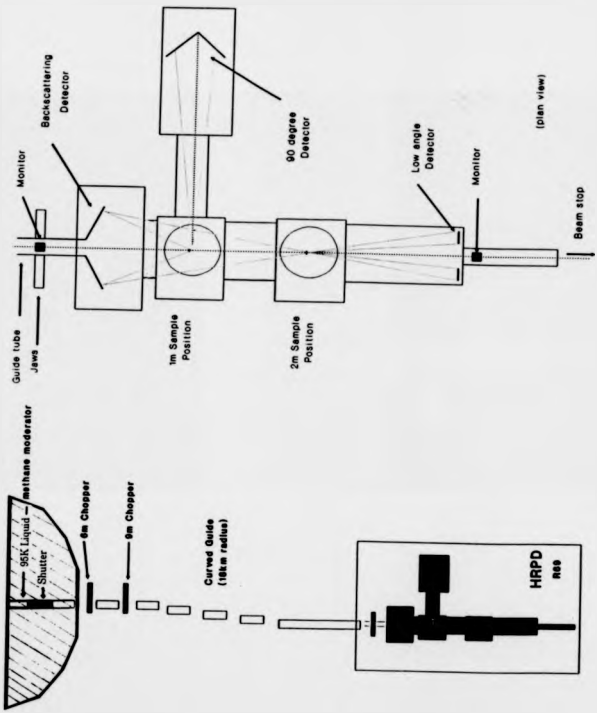

Figure 4.1 The High Resolution Powder Diffractometer HRPD at ISIS.

In diffraction all the scattering is elastic so only the d.c.s (chapter 3) is considered. The beam need not be monochromatic as λ can be calculated from the neutron TOF at fixed values of θ (the detector positions). Equation (3.1) therefore reduces to:

$$Q = \frac{4\pi \sin\theta}{\lambda} \qquad (4.4)$$

where $Q = |\mathbf{Q}|$ and $\lambda = 2\pi/|\mathbf{k}|$. In practice a fully polychromatic beam results in "frame overlap". This occurs when the slower neutrons from one frame arrive after the start of the next, mixing with its fast neutrons (frames are synchronized to the ISIS pulse at 50 Hz). To eliminate this effect, discrete wavelength "windows" are selected by the use of two beam choppers. These are situated at about 6 m and 9 m from the moderator. The first operates at 50 Hz and the second is slower at 50/n Hz (where n is an integer). The phasing of these two choppers, relative to the initial pulse, and the value of n determine the mean λ and the size of the window (0.4 Å for n=1, up to 2.0Å for n=5). The neutrons travel between the instrument and the moderator along a nickel plated glass tube which guides the neutrons by multiple reflections. A large section of the guide is gently curved (18 km radius) which eliminates the direct line of site to the moderator (and hence short time γ's) and removes neutrons too fast to be reflected ($\lambda \leq 0.5$ Å).

As the beam enters the instrument its intensity is monitored. The sample can be positioned at 1m (as for all the work presented here) or at 2m (for maximum resolution) from the back-scattering detector. The 1m position is chosen when the extra flux (four times greater) is more essential than very high resolution — ie. when studying many samples over a wide range of temperature in a limited time. The transmitted

beam is monitored just past the low angle detector. Data are only stored ("good" frames) when the 6 m chopper is correctly synchronized with the synchrotron pulse. This condition is checked by the Front End Monitor (FEM); a microVax(II) computer (which is also used to initially store the data and to control the instrument).

Section 4.2 Correction and Normalization of Raw Data

Usually the back-scattering detector elements are grouped into 20 concentric rings (as mentioned in chapter 3). The spectra from these can then be summed (allowing for the different θ) to give a "raw" spectrum consisting of neutron counts as a function of TOF over the selected window. On HRPD the TOF (in μs) is roughly 50555.5 x d-spacing (in Å) for back-scattering (David 1988).

All spectra are first normalized to the same number of monitor counts (using the transmitted beam monitor) so that they can be directly compared. They are then calibrated by comparison with a Vanadium standard (as outlined in chapter 3).

The corrected files are then converted to a data format which can be read by the various analysis software available at ISIS. Further corrections are applied during the refinement process which is described in the following section.

Section 4.3 Refinement of Structure

The method of structural determination used for all the HRPD data reported in this thesis was that of Rietveld profile refinement (Rietveld 1967,1969). Unlike previous methods, this attempts to fit the entire diffraction profile (by least squares) so as to make full use of the information contained in it. The Rietveld method was originally developed for use with single λ neutron diffraction in which the peak shape may be assumed to be Gaussian. The nature of the pulse-production/moderation at ISIS (and similar sources) results in a more complex peak shape which is modelled by a combination of functions. Wavelength dependant absorption and extinction corrections must also be applied to TOF data. The principles of the refinement are the same in all cases.In the single λ case the function to be minimized is:

$$\rho = \sum_i w_i \left(Y_i^{obs} - Y_i^{calc}\right)^2 \qquad (4.5)$$

where i denotes a position $2\theta_i$, $w_i = \sigma_i^{-2}$ and the Y_i are the observed and calculated intensities at each position respectively such that:

$$Y_i^{calc} = \sum_k y_{ik} \qquad (4.6)$$

and the y_{ik} are the contributions to the intensity from given reflections, k, at position i. These may be calculated from:

$$y_{ik} = \alpha j_k L_k S_k^2 \left(\frac{2\sqrt{\ln 2}}{H_k\sqrt{\pi}}\right) \exp\left[-4\ln 2\,((2\theta_i - 2\theta_k)/H_k)^2\right] \qquad (4.7)$$

where α is a constant, S_k^2 is the quadrature sum of the nuclear and the magnetic structure factors, j_k is the multiplicity of reflection, L_k is the Lorentz factor, $2\theta_k$ is the calculated peak position and H_k is the full width at half-height (which depends on a number of instrument parameters).

The quality of a refinement ("goodness of fit") is naturally expressed in the chi-squared parameter:

$$\chi^2 = \frac{1}{N-P+C} \sum_i w_i \left(Y_i^{obs} - Y_i^{calc} \right)^2 \qquad (4.8)$$

where N, P and C are the number of observations, variables and constraints respectively and the sum is over the number of degrees of freedom. Normally however the goodness of fit is considered with respect to the four residuals: Weighted Profile (R_{WP}), Profile (R_P), Integrated Intensities (R_I) and Expected (R_E). These are defined as:

$$R_{WP} = \sqrt{\frac{\sum_i w_i \left(Y_i^{obs} - Y_i^{calc} \right)^2}{\sum_i w_i \left(Y_i^{obs} \right)^2}} \qquad (4.9)$$

$$R_P = \left(\frac{\sum_i \left(Y_i^{obs} - Y_i^{calc} \right)}{\sum_i \left(Y_i^{obs} \right)} \right) \qquad (4.10)$$

$$R_I = \left(\frac{\sum_k \left(I_k^{obs} - I_k^{calc} \right)}{\sum_k \left(I_k^{obs} \right)} \right) \qquad (4.11)$$

$$R_E = \sqrt{\frac{N - P + C}{\sum_i w_i \left(Y_i^{obs} \right)^2}} \qquad (4.12)$$

The relationship of these to χ^2 ($\chi = R_{WP}/R_E$) means that for a nearly perfect refinement $R_{WP} - R_E$ (the value expected from the statistics).

The HRPD data presented in later chapters were refined using the TF12LS code. This describes the peak shape as Voigt functions and fits the background to a 5th order Chebyshev polynomial (see David et al 1988).

Space does not permit the full details of such a structural refinement to be given here but the interested reader is referred to the worked examples for $La_2SrCu_2O_6$ (HRPD users guide 1988) and Al_2O_3 (David 1988).

CHAPTER 5

INELASTIC NEUTRON SCATTERING

Introduction

The ability of the neutron to probe the excitations of condensed matter has been exploited for many years with great success. Recently it was used to study intermultiplet transitions in Pr (Taylor et al 1988) showing that it can now complement the well established groundstate intramultiplet work. Inelastic experiments are performed on all types of sources but those which obtain neutrons by spallation, such as ISIS, have the advantage of possessing a large number of epithermal and fast neutrons. This enables scattering with energy transfer up to ~1000 meV to be investigated. All the inelastic data presented (Chapter 9) were collected on the High Energy Transfer spectrometer (HET) at ISIS (Taylor et al 1987). This chapter will deal specifically with HET but in doing so will also cover some general features common to this kind of work.

Section 5.1 Collection of Spectra

There are two main types of inelastic spectrometers: Direct and Indirect Geometry. HET is an example of the former; incident energy (E) is selected by a beam chopper before the neutrons reach the sample. In the latter kind the energy selection takes place after scattering with the incident neutron energy being found from the total TOF.

On HET (see figure 5.1) a Fast Fermi Chopper (rotating at 600 Hz — phase locked to the synchrotron pulse) is used to select E over a range 100-1000 meV with a resolution ($\Delta E/E$) better than 1%. It has three main detector banks which cover low angle (2θ = 3 - 7°), medium angle (2θ = 10 - 30°), and high angle (movable over: 2θ = 80 - 140°). The detector banks are positioned at 4m, 2m and 4m from the sample position respectively. The resolution ($\Delta\hbar\omega/E$) is best when the energy transfer ($\hbar\omega$) is close to the incident energy. In this case it can be given to a rough approximation (after Williams and Lovesey 1989) as:

$$\frac{\Delta\hbar\omega}{E} = 2\sqrt{\left(\frac{\Delta T_c}{T_c}\right)^2 + \left(\frac{\Delta T_o}{T_c}\right)^2} \qquad (5.1)$$

where T_o and T_c are the start time of the pulse at the moderator (T=0) and the time the neutrons (with energy E) reach the chopper. ΔT_o and ΔT_c are the respective uncertainties in these times. Thus when examining the spectrum of a sample which has features of interest over a wide range of energy transfer a number of runs at different E must be performed.

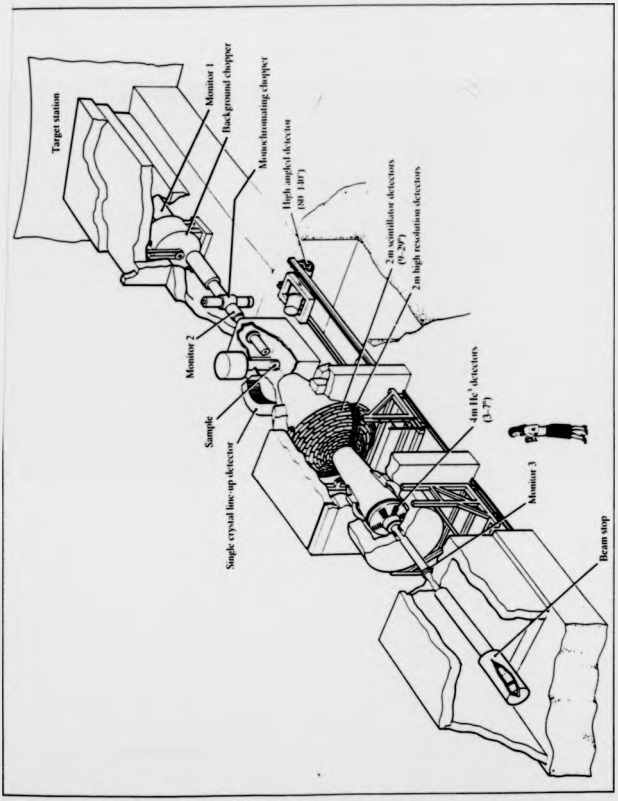

Figure 5.1 The High Energy Transfer chopper spectrometer HET at ISIS.

The main instrument control/data collection is performed via a microVax(II) computer (as for HRPD — described in chapter 4) which allows the build up of a spectrum to be viewed in real time. The detection at different angles allows spectra to be compared at different **Q** without changing E. This is particularly important for identifying magnetic scattering as is explained in the next section.

Section 5.2 Assessment of Data

5.2.1 Introduction

This section is not intended as a general guide to all inelastic data analysis, rather it is specific to inelastic scattering of unpolarised neutrons (as used for the study of Pr-123 reported in Chapter 9).

All spectra are converted to p.d.c.s. against energy transfer, as explained in Chapter 3, by normalising to the same monitor count and calibrating with respect to a Vandadium standard. At this stage it is useful to consider the "master formula" for the p.d.c.s. which covers the general case of neutron scattering. It is given, for unpolarised neutrons, (after Marshall and Lovesey 1971a) as:

$$\frac{d^2\sigma}{d\Omega dE'} = \frac{k'}{k}\left(\frac{m}{2\pi\hbar}\right)^2 \sum_\lambda p_\lambda \sum_{\lambda'} |\langle k\lambda'|V|k\lambda\rangle|^2 \, \delta(\hbar\omega + E_\lambda - E') \qquad (5.2)$$

where p_λ is the thermal occupation probability of the state λ and V is the neutron - target interaction potential.

This expression is just the sum of the p.d.c.s.'s for coherent and incoherent scattering. Each of these is the sum of elastic and inelastic terms and each term is the sum of nuclear and magnetic components.

When working on a spectrometer such as HET, the main features of the spectrum (besides the large elastic peak resulting from all the elastic terms situated at zero energy transfer) result from inelastic scattering; nuclear and (where appropriate) magnetic.

5.2.2 Nuclear Inelastic Scattering

Both the coherent and incoherent contributions are discussed. The former, which is the scattering from dynamic variations unrelated to any inherent inhomogeneity in the sample, is of most interest. Interference effects are seen because of a correlation between positions of nuclei at different times.

Marshall and Lovesey (1971b) give the inelastic coherent p.d.c.s. (in the harmonic approximation) as:

$$\left(\frac{d^2\sigma}{d\Omega dE'}\right)^{inel}_{coh} = \frac{\sigma_c}{4\pi}\frac{k'}{k}\frac{1}{2\pi\hbar}\int_{-\infty}^{\infty} dt \exp[-i\omega t]\exp[-2W(\mathbf{Q})]\, x$$

$$x \sum_{\lambda\lambda'} \exp[-i\mathbf{Q}\cdot(\mathbf{l}-\mathbf{l}')]\,[\exp[\langle \mathbf{Q}\cdot\hat{\mathbf{u}}(\mathbf{l},0)\,\mathbf{Q}\cdot\hat{\mathbf{u}}(\mathbf{l}',t)\rangle] - 1] \qquad (5.3)$$

where $\mathbf{l}$ is the position vector of the l^{th} nucleus (at time zero), $\mathbf{l}'$ is the position vector of the l'^{th} nucleus (at time t), $\hat{\mathbf{u}}$ is the displacement operator (for the nuclei). The Debye - Waller factor ($W(\mathbf{Q})$) is introduced

to represent the effects of thermal vibrations of nuclei form their equilibrium positions. At low temperatures it can be taken as unity.

If the exponential containing the displacement correlation function is expanded then the first non-zero terms give the one-phonon p.d.c.s., the second the two-phonon p.d.c.s. etc. If the one-phonon process is considered (Marshall and Lovesey 1971c) a sum of two delta functions occurs — one represents the creation of a phonon, the other the annihilation of a phonon. The delta functions arise from the Harmonic approximation and the necessary conservation of energy and momentum:

$$E' = E + \hbar\omega_j(\mathbf{q}) \quad \text{and} \quad \mathbf{k}' = \mathbf{k} + \mathbf{q} - \tau \qquad (5.4)$$

where $\mathbf{q}$ is the phonon wave vector, τ is just a reciprocal lattice vector (such that $\mathbf{q}$ and $\mathbf{q}+\tau$ give the same displacement) and the subscript j is used to designate each of the normal modes. The "dispersion relation" ($\omega_j(\mathbf{q})$ as a function of $\mathbf{q}$) is thus obtained from the one-phonon p.d.c.s.

The incoherent inelastic p.d.c.s. gives scattering with a continuous energy distribution proportional to the normalized vibrational density of states as energy is conserved but not momentum.

If anharmonic terms (resulting from phonon - phonon and electron - phonon interactions) are introduced then the delta functions are replaced by a spread in energy due to finite phonon life times.

As E is increased, more phonons can become involved — "multiphonon processes". Fortunately, in cases where the main interest is not in the phonons (as in the present study), multiphonon processes do not generally contribute sharp features to the spectra. This is recognized in Planczek's incoherent approximation (see Marshall and

Lovesey 1971d) which roughly states that when two or more phonons are involved the conservation of energy and crystal momentum are not restrictive. Hence the multiphonon scattering tends to be a smoothly varying function of scattering angle and incident energy.

5.2.3 Magnetic Inelastic Scattering

Magnetic scattering results from interactions between the neutron magnetic moment and the magnetic field due to unpaired electrons in the crystal. This contributes the usual dipole potential to the neutron energy.

The magnetic moment of the neutron is anti-parallel to its spin with a magnitude proportional to the nuclear magneton, μ_N , similar to the relationship of the electron moment to the Bohr magneton, μ_B .

Following the argument of Marshall and Lovesey (1971e), the magnetic part of the p.d.c.s. can be obtained by: (i) writing down the expression for the field due to a single moving electron,(ii) expressing the dipole potential of a neutron in terms of this field, and (iii) replacing V in the master formula (5.1) by the sum of all such interactions.

The resulting expression can then be simplified (after Marshall and Lovesey 1971f) to give:

$$\frac{d^2\sigma}{d\Omega dE'} = \frac{k'}{k}\left(\frac{\gamma e^2}{m_e c^2}\right)\sum_{\alpha\beta}(\delta_{\alpha\beta} - \bar{q}_\alpha\bar{q}_\beta)\, x$$

$$x \sum_{\lambda\lambda'} p_\lambda \langle\lambda|M_\alpha|\lambda'\rangle\langle\lambda'|M_\beta|\lambda\rangle\, \delta(\hbar\omega + E_\lambda - E_{\lambda'}) \qquad (5.5)$$

where $\gamma = -1.91$, e, m_e and c have their usual meanings and the $\bar{q}$ are the unit vectors ($\mathbf{Q}/|\mathbf{Q}|$). The sum over α,β (cartesian coordinates) and the

term $(\delta_{\alpha\beta} - \hat{Q}_\alpha \hat{Q}_\beta)$ results from writing the p.d.c.s. in terms of the cartesian components (M_α, M_β) of the Fourier transform of the magnetization density, $\mathbf{M}(\mathbf{Q})$.

At this stage many introductory accounts go on to consider just the scattering due to electron spins. This is not helpful in the case of the rare earths, however, due to strong spin - orbit coupling. In this case it is best to re-write $\mathbf{M}(\mathbf{Q})$ in terms of the total angular momentum, $\mathbf{J}$. In the dipole approximation (see Marshall and Lovesey 1971g) this is given as:

$$\mathbf{M}(\mathbf{Q}) = {}^1/_2 \, g \, F(\mathbf{Q}) \, \mathbf{J} \tag{5.6}$$

where $F(\mathbf{Q})$ is the form factor for magnetic scattering (as defined by Marshall and Lovesey 1971h), which generally falls off rapidly as $\mathbf{Q}$ increases, and g is the Lande' splitting factor. The factor of "$^1/_2$" arises in the formulation of the dipole approximation.

Equation 5.5 can be simplified (after Lovesey 1984) when written in units of mb sr^{-1} meV^{-1} and introducing the Debye - Waller factor, as in 5.3 above, as:

$$\frac{d^2\sigma}{d\Omega dE'} = 72.5 \, \frac{k'}{k} \, F^2(\mathbf{Q}) \, \exp\{-2W(\mathbf{Q})\} \, S(\mathbf{Q},\omega) \tag{5.7}$$

The response function, $S(\mathbf{Q},\omega)$, has been used to represent all the scattering that is determined entirely by the temperature and eigenfunctions of the system (see §3.1). It is just:

$$S(\mathbf{Q},\omega) = \sum_{\lambda\lambda'} p_\lambda \, | \langle \lambda' | \hat{\mu}_\perp | \lambda \rangle |^2 \; \delta(\hbar\omega + E_\lambda - E_{\lambda'}) \tag{5.8}$$

where $|\lambda\rangle$ and $|\lambda'\rangle$ are the initial and final eigenfunctions of the system corresponding to the eigenvalues E_λ and $E_{\lambda'}$ and $\hat{\mu}_\perp$ is the component of the magnetic moment operator perpendicular to $\mathbf{Q}$.

$S(\mathbf{Q},\omega)$ is shown by linear response theory (see Marshall and Lovesey 1971i) to be related to the imaginary part of the generalized susceptibility, $\chi(\mathbf{Q},\omega)$ as (after Fulde and Loewenhaupt 1985):

$$S(\mathbf{Q},\omega) = \frac{1}{1 - \exp(-\hbar\omega/k_B T)} \, \mathrm{Im}\chi(\mathbf{Q},\omega) \qquad (5.9)$$

$\chi(\mathbf{Q},\omega)$ is just the response of a magnetic system to a temporally and spatially varying magnetic field (as would be created by the passage of a neutron through the system). Hence $\mathrm{Im}\chi(\mathbf{Q},\omega)$ may be determined from an inelastic neutron spectrum. In principal the $\mathrm{Re}\chi(\mathbf{Q},\omega)$ may also be calculated using the Kramers - Kronig relation if $\mathrm{Im}\chi(\mathbf{Q},\omega)$ is measured over all ω, or else the static susceptibility $\chi(\mathbf{Q})$ may be calculated (see Rainford 1988).

Consideration of 5.8 and 5.9 would indicate that $\mathrm{Im}\chi(\mathbf{Q},\omega)$ is just a series of delta functions. In a real inelastic spectrum they will be seen as peaks — broadened by finite lifetime effects (see for example Fulde and Loewenhaupt 1985 or Rainford 1988) as for the phonon spectra (§ 5.2.2). For samples in which there is long range magnetic order, there can be coherent magnetic scattering from magnons in a similar fashion to the phonon scattering discussed in §5.2.2.

5.2.4 Summary

An inelastic scattering spectrum from a polycrystalline sample (as used in this study) will thus have an elastic peak centred about $\hbar\omega$ = 0 (zero energy transfer) and other features to each side. There will be an

incoherent nuclear background which generally dies away with ω. Depending on the choice of E, phonon peaks may be visible and (if the sample is magnetic) magnetic intensity/ peaks may also be present. At T = 0 features can only appear for positive energy transfer (there are no excitations for the neutron to annihilate). As T is increased negative energy transfer also begins to be populated.

The magnetic scattering can be identified by looking at the **Q** dependence of any features. Those of a magnetic origin will be prominent at low **Q** (small scattering angles on HET) but not at high (see previous section). It can be separated from nuclear scattering by a number of methods. The simplest (where possible) is to use a non-magnetic "blank", a compound which is structurally similar to that being investigated but containing no magnetic ions. A fit to the magnetic data can then be made using 5.7 or a more sophisticated version which allows for lifetime effects (see Fulde and Loewenhaupt 1985).

Section 5.3 Crystal Electric Field Spectra

5.3.1 Introduction

This section is concerned with the treatment of magnetic scattering resulting from magnetic rare earth ions in a crystal lattice.

A magnetic ion in a crystal will not respond in the same way as a free ion due to its coupling to the lattice and electronic/ magnetic interactions with other ions. The exact nature of the interactions can often be ignored and the total effect may simply be expressed as an

interaction with the electrostatic field of nearby ions — the Crystal Electric Field (CEF). This has the same symmetry as the surrounding ions and thus, for rare earth ions, it may partially or completely lift the 2J+1 degeneracy of the g.s. wavefunctions. Transitions between levels may thus be observed using inelastic neutron scattering providing E is chosen to be of the same order as the spread in the levels.

A simple example of a calculation of the transition matrix elements for Pr^{3+} is given by Marshall and Lovesey (1971j). In general, however, when the exact nature of the CEF is not known and/ or the valence (and thus J) is not known an attempt must be made to fit the measured spectrum to a suitable model — in practice this may not be easy.

At low temperature (near 2K), and with the correct choice of E, the only magnetic peaks in the spectrum will be those corresponding to excitations from the ground state to higher levels of the ground state multiplet. These will be seen in neutron energy loss — positive energy transfer. Any thermal population of the higher levels is negligible. As temperature is increased, thermal population of the higher levels becomes more significant. Peaks begin to appear in negative energy transfer corresponding to ground state levels and the peak intensity of the lowest levels reduces.

In cases where the CEF splitting of the g.s. is comparable to the energy separation to the next J multiplet, significant admixture of the higher J states should be expected. This is the case for the work on Pr123 presented in Chapter 9. The model used to fit this data is explained below.

5.3.2 The Crystal Electric Field Model

The theoretical model used to analyse the data collected in the HET experiments described in Chapter 9 has been described in detail elsewhere (see Boothroyd et al 1992 a,b). The main points are as follows:

The CEF Hamiltonian is written as:

$$H_{CEF} = \sum_{kq} B_q^k \; C_q^k \qquad (5.10)$$

where the C_q^k is the q^{th} component of a spherical tensor of rank k and the B_q^k are the corresponding CEF parameters (note that the B_q^k are related to the similar parameters in the Stevens' operator formulation (Stevens 1952) by numerical scaling factors — tabulated by Kassman (1970)). In the first approximation the B_q^k can be expressed as the product of two factors:

$$B_q^k = \langle r^k \rangle \; A_q^k \qquad (5.11)$$

where $\langle r^k \rangle$ is the k^{th} moment of the 4f radial wavefunction and the A_q^k are the intrinsic CEF parameters independent of the R ion. Equation 5.11 allows the CEF parameters of various R doped into the same compound (ie. R123) to be estimated. The point group symmetry of the crystal structure determines which of the B_q^k are non-zero. For the D_{2h} symmetry of the R site in R123 there are nine (see Walter 1984): B_0^2, B_0^4, B_0^6, B_2^2, B_2^4, B_2^6, B_4^4, B_4^6, and B_6^6.

Weak magnetic interactions may also take place between the ions and to account for these a molecular field term (MF) is introduced into the Hamiltonian:

$$H_{MF} = -\mu_B \, \hat{\mu} \cdot \mathbf{B}_{MF} \qquad (5.12)$$

This represents the energy of the R ion in an effective MF, $\mathbf{B}_{MF}$, from neighbouring ions. The terms $\hat{\mu}$ and μ_B are the magnetic moment operator and the Bohr magneton respectively. In Pr123 the spins in the ordered phase lie parallel to the CEF quantisation axis (Li et al 1989) — the [0 0 1] direction — and hence 5.12 is simplified to:

$$H_{MF} = -h_{MF} \hat{\mu}_z \tag{5.13}$$

where h_{MF} is a molecular field parameter with dimensions of energy and $\hat{\mu}_z$ is the z-component of $\hat{\mu}$. The MF interaction is expected to be much smaller than the CEF splitting in the compounds studied and was thus treated by perturbation theory including terms to second order in h_{MF}.

The Hamiltonian of this system can thus be taken as:

$$H = H_0 + H_{at} + H_{CEF} + H_{MF} \tag{5.14}$$

where H_0 is the one-electron Hamiltonian, H_{at} accounts for inter-atomic interactions (mainly due to Coulomb repulsions and spin-orbit coupling), H_{CEF} and H_{MF} are given by 5.10 and 5.14 respectively. The data analysis in Chapter 9 used programs based on those developed at Argonne described by Soderholm et al (1991) and Goodman et al (1991) and (with modifications) by Boothroyd et al (1992a,b). The basic method used is to estimate h_{MF} from experimental parameters (see Chapter 9), take the free ion parameters as constants and adjust the CEF parameters by a weighted, least squares, fitting routine until the best agreement is obtained between the calculated and observed transition energies and intensities. The eigenfunctions (perturbed by H_{MF}) are then used to calculate transition probabilities, magnetic susceptibility and ordered moments.

CHAPTER 6

NUCLEAR MAGNETIC RESONANCE

Introduction

This chapter is intended as a short introduction to the basic principals of Nuclear Magnetic Resonance or "NMR". It is included as a guide for the reader, unfamiliar with the technique, to some of the terms used in Chapter 10. More definitive information may be obtained from the many books on the subject, for example those of Abragam or Slichter (see Bibliography).

Nuclei with non-zero nuclear spin (**I**) possess a magnetic moment (μ_N). The degeneracy is lifted in the presence of a magnetic field ($\mathbf{B}_0$) to give $2(I+1/2)$ discrete energies for the dipole interaction ($\mu_N \cdot \mathbf{B}_0$). It is possible to drive transitions between these levels by the application of an oscillating magnetic field ($\mathbf{B}_1$) perpendicular to $\mathbf{B}_0$. At a specific frequency (ω) the process is resonant. This is the classical Larmor frequency:

$$\omega = \gamma B_0 \qquad (6.1)$$

where γ is the nuclear magnetogyric ratio. The value of γ depends on the nucleus involved but for a typical nucleus ω = 10 MHz for a field of one Tesla. $\mathbf{B}_1$ is thus referred to as the RF (radio frequency) field. The individual magnetic moments may be pictured as precessing about $\mathbf{B}_0$ at a frequency ω. Spin $1/2$ nuclei, for example, will precess on one of two

cones with axes parallel or anti-parallel to $\mathbf{B}_0$. Strictly ω is the magnitude of a vector, ω, anti-parallel to $\mathbf{B}_0$ and hence 6.1 can be written as:

$$\omega = -\gamma \mathbf{B}_0 \qquad (6.2)$$

It is found that the above expression holds only for a bare nucleus; normally the effective field at the nucleus ($\mathbf{B}_{eff}$) differs from $\mathbf{B}_0$ because of secondary fields set up by its own electrons and neighbouring atoms.The resonant frequency determined in a material will thus be different to that expected for a bare nucleus. It is normal to put all measurements on a dimensionless scale. For a selected nucleus in a sample the resonant frequency is expressed as a "shift",δ, relative to the same resonance in a reference compound. The shift is then normalised to the field strength, B_0. As shifts tend to be of the order of 10^{-6} they are usually expressed in parts per million (ppm).

Section 6.1 Relaxation Times

In equilibrium the populations of the different levels obey Boltzmann statistics and there is thus a slightly larger population in the lower energy states than in the higher. When $\mathbf{B}_1$ is applied the number of transitions to the higher states will be larger than the reverse transitions (which individually have the same probability) solely because of the population imbalance. There will thus be a net change in magnetisation of the sample which constitutes the NMR signal (see §6.2). This dies away rapidly as the populations approach parity. The

removal of $\mathbf{B}_1$ allows the thermal equilibrium to be restored. This is achieved by various "relaxation" mechanisms.

The direction of $\mathbf{B}_0$ is normally taken as z' — the z-axis of a reference frame rotating at the resonant frequency, ω. The RF field, $\mathbf{B}_1$, is applied at ω along the x-axis of the laboratory reference frame, x. The oscillating RF field acts like two counter-rotating fields of fixed magnitude. One component will rotate in the same sense as ω and will thus be stationary in the rotating frame (lying along the x' axis) — the other component will rotate at 2ω in this frame (well off resonance) and can be ignored. Initially the net magnetisation ($\mathbf{M}$) of the sample lies in the z-direction with the individual magnetic moments precessing in a cone about $\mathbf{B}_0$. If $\mathbf{B}_0$ is applied for long enough the moments can be pictured as being aligned with $\mathbf{B}_0$ to give a maximum value of $\mathbf{M}$ (see figure 6.1). The effective field in the rotating frame is given by:

$$\mathbf{B}_{eff} = \mathbf{B}_0 + \omega/\gamma \qquad (6.3)$$

but substituting for ω using 6.2 reduces $\mathbf{B}_{eff}$ to zero. Hence when $\mathbf{B}_1$ is applied along x', $\mathbf{B}_{eff} = \mathbf{B}_1$ and $\mathbf{M}$ precesses about $\mathbf{B}_1$ in the y'-z' plane (ie. coplanar with $\mathbf{B}_0$) — see figure 6.2.

6.1.1 Spin-Lattice Relaxation

The neighbouring atoms constitute the "lattice" with which a given nucleus may exchange energy. It does this by the interaction of its magnetic moment with those of its neighbours or with fluctuating magnetic fields set up by their thermal motions. The lifetime of a nucleus in a particular state is thus determined by the ease with which these processes may occur and is known as the "spin-lattice" relaxation time, T_1. This may be of the order of days in certain solids, but is

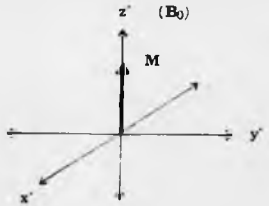

Figure 6.1 The net magnetisation lying in the z′-direction in the rotating frame.

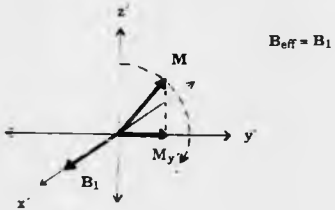

Figure 6.2 The precession of **M** in the y′-z′ plane when $\mathbf{B}_1$ is applied.

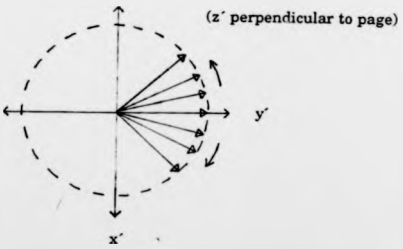

Figure 6.3 Individual moments drift out of phase and spread out in the x′-y′ plane.

normally in the range 10^{-3} to 10 seconds. The relaxation rate, T_1^{-1}, in general depends on the strength (E) and the life-time (τ) of the interaction as follows:

$$T_1^{-1} = E^2 F(\tau) \qquad (6.4)$$

where $F(\tau)$ is some function of τ.

When $\mathbf{B}_1$ is removed, $\mathbf{M}$ gradually (in a time dependent on T_1) returns to its alignment with $\mathbf{B}_0$. In the laboratory frame $\mathbf{M}$ precesses about $\mathbf{B}_0$ while this takes place but in the rotating frame $\mathbf{M}$ is confined to the y'-z' plane and the angle between $\mathbf{B}_0$ and $\mathbf{M}$ decreases with time. The component of $\mathbf{M}$ in the y'-direction ($M_{y'}$) normally forms the NMR signal. $M_{y'}$ rotates at ω in the x-y plane of the lab frame and the magnetisation is detected by a coil along the y-axis. The signal thus varies sinusoidally and decays with time. This is called the "Free Induction Decay (FID)".

6.1.2 Spin-Spin Relaxation

$M_{y'}$ may decrease more rapidly if the individual moments drift out of phase (ie. they begin to spread out in the x'-y' plane —see figure 6.3). This can result from small local inhomogeneities in the magnetic field inherent in $\mathbf{B}_0$ or due to neighbouring magnetic ions. The timescale over which the moments de-phase is T_2^* and this is inversely proportional to the spread of magnetic field strength, ΔB_0. If the magnet inhomogeneity is made sufficiently small then T_2^* depends only on the interaction with neighbouring ions and is it called the "spin-spin" relaxation time, T_2. Experimental techniques also exist which allow magnet inhomogeneity effects to be removed and T_2 to be determined.

Section 6.2 The NMR Experiment

The basic requirements for a typical NMR experiment are: (i) a stable and uniform DC magnetic field, (ii) an RF transmitter and suitable receiver connected to a coil assembly (in which the sample sits) and (iii) a means of storing/ displaying data.

Data may be collected by "Continuous Wave (CW)" or "Fourier Transform (FT)" spectroscopy (also called "pulsed NMR") — only the latter will be discussed here. The FT method involves the transmission of a short (~50μs) intense RF pulse. This has a large bandwidth (ie. 5KHz) and excites all sensitive nuclei. A signal proportional to the net magnetisation, $M_{y'}$ (in the rotating frame), is observed which has components of frequency equal to the difference between the pulse centre and ω for the nuclei. This decays exponentially with time (as explained above in § 6.1.2) — "Free Induction Decay (FID)". The FT is then taken to produce a spectrum of absorption intensity against frequency with the appropriate resonance peaks.

Normally various combinations of pulse length and repetition rate are used to maximize the information from the sample. Initially the magnetization is all in the direction of $\mathbf{B}_0$ (the z-axis), but the application of $\mathbf{B}_1$ causes it to rotate away to an angle proportional to the pulse length. A "90° pulse" is thus one which rotates the magnetization into the x-y plane and is the one usually used to observe the FID. Just after the pulse $M_{y'} = |\mathbf{M}|$. Proper use of pulse sequences allows accurate determination of T_1 and the sample dependent contribution to $T_2^* — T_2$.

One method involves the use of a "saturating comb" of 90° (or almost 90°) pulses followed by a sampling pulse. The comb pulses are separated by a time τ_1 (such that $T_2^* < \tau_1 << T_1$) and following the comb M_z will be zero. The comb may consist of 6 to 14 pulses depending on how close the pulse width is to a 90° pulse. After the comb the magnetisation begins to recover ($M_z > 0$). A final 90° pulse is applied after a time $\tau >> \tau_1$ to sample the extent of the recovery by tipping M_z into the x-y plane. The sequence in then repeated (often after a longer delay determined by the maximum allowed output power of the transmitter) many times so as to maximise the signal to noise ratio. T_1 is determined from a number of such measurements covering a range of τ values. The interested reader is referred to the texts mentioned above (in the introduction to this chapter) and especially that of Fukushima and Roeder (see Bibliography) for further information on such techniques.

Section 6.3 Shifts

There are a number of mechanisms which result in the local field at a nucleus being different to $\mathbf{B}_0$ and which therefore produce shifts in the resonant frequency. The principal ones are: (i) the Dipole - Dipole interaction, (ii) Chemical Shift, (iii) Spin - Spin Coupling, (iv) the Contact interaction and (v) the Quadrupolar interaction. All these interactions can also cause spin relaxation because they alter $\mathbf{B}_{eff}$ at individual nuclei.

(i) The Dipole - Dipole interaction is always present and acts between the magnetic moments of neighbouring nuclei. This results in

an angular dependant correction to $\mathbf{B}_0$ at each nucleus which has the form $(1 - 3\cos^2\theta)$, where θ is the angle of a pair of nuclei to $\mathbf{B}_0$. The random orientation of such pairs leads to broad resonances in most samples. This effect is eliminated by spinning samples on a axis set at 54.7° to $\mathbf{B}_0$ — the so called "Magic Angle" at which the angular dependant term becomes zero. The technique is therefore referred to as Magic Angle Spinning or "MAS".

(ii) The Chemical Shift (σ) is a consequence of the chemical environment of the nuclei (ie. their electron clouds and bonds with other atoms) which shields them from the full applied field ($\mathbf{B}_{eff} < \mathbf{B}_0$). Fields which oppose $\mathbf{B}_0$ are set up by the precession of the electron charge clouds and by the orbital moments of unfilled shells. In solids the local chemical environment of equivalent nuclei may be anisotropically orientated to $\mathbf{B}_0$ and this produces wide resonances. Spinning the sample, as in MAS, reduces this broadening.

(iii) Spin - spin coupling between neighbouring nuclei results in a splitting of resonance lines (dependent on the values of I for each nucleus) which is independent of the applied magnetic field.

(iv) The spin relaxation time for unpaired electrons is much shorter than that of nuclei. The "contact" interaction between electron and nuclear spins is therefore simplified to a shift in the resonance position due to the nucleus experiencing the time averaged field from the electron spin motions. Where this occurs (ie. in metals) it much larger than the chemical shift and is known as the Knight shift (K). It is found to be proportional to the electron spin (or "Pauli") susceptibility (χ_P) and the density of states at the Fermi Level ($N(\epsilon_F)$):

$$K = \frac{2}{3} \chi_P \Omega |\psi(0)|^2 \qquad (6.5a)$$

$$\chi_P = \mu_0 \beta^2 N(\varepsilon_F) \qquad (6.5b)$$

where Ω is the atomic volume (assuming one conduction electron per atom), $\psi(0)$ is the electronic wave-function at the nucleus and β is the Bohr Magneton.

The Knight Shift is related to the spin-lattice relaxation time (T_1), in simple metals, by the Korringa (1950) relation:

$$K^2 T_1 T = \text{constant} \qquad (6.6)$$

where T is the sample temperature in Kelvin. This can be used to predict T_1 values as a function of temperature. The relation assumes only one relaxation mechanism so if more than one acts then the actual T_1's will be shorter than predicted.

For the high Tc superconductors in the normal (metalic) state the shift (S) is mainly due to the chemical shift and the Knight shift, thus:

$$S = K + \sigma \qquad (6.7)$$

(v) Quadrupolar nuclei with non-symmetric charge distributions tend to align themselves with the crystal electric field to minimize free energy. Their interaction with this field, the "Quadrupolar Interaction", results in a splitting of resonance lines which is independent of $\mathbf{B}_0$ and may be observed by applying only an RF field.

CHAPTER 7

STRUCTURAL PHASE TRANSITIONS IN $La_{2-x}Ba_xCuO_4$

Introduction

The doped La_2CuO_4 oxides were the first of the new high T_c compounds to be discovered (Bednorz and Müller 1986) and have thus been subjected to extensive experimental study and theoretical speculation ever since. Superconductivity can be induced in the parent compound by doping with Ba, Sr or Ca or by increasing the oxygen content above 4 (Beille et al 1987). The maximum T_c in the $La_{2-x}Ba_xCuO_4$ system occurs near x = 0.15, falling off for higher or lower x, with an anomalous dip near x = 0.12 (Suzuki and Fujita 1989 and Axe et al 1989a). The basic crystal structure is that of the undoped parent compound which is a layered perovskite. This has been shown previously (Grande et al 1977) to be tetragonal (I4/mmm) at high temperatures and orthorhombic (Abma) below 500 K (see figure 7.1). To be consistent with the literature the former will be referred to as the "high temperature tetragonal" or HTT phase and the latter as the "low temperature orthorhombic" or LTO phase. The main structural features are staggered planes of CuO_6 octahedra (see figure 7.2). The LTO phase is referred to in the literature variously as Abma, Bmab and Cmca. These are equivalent crystallographic descriptions which differ only by the choice of axes. A full explanation of this is given by Pickett (1989).

Jorgensen et al (1987), in early neutron diffraction work, confirmed the room temperature LTO phase space group in La_2CuO_4 and also concluded that for Ba doping of x = 0.15 the compound retained

$La_{2-x}\ Ba_x\ Cu\ O_4$

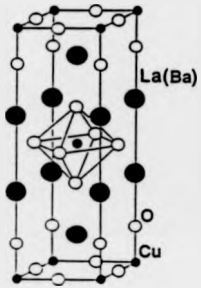

Figure 7.1 The structure of $La_{2-x}Ba_xCuO_4$ — note the CuO_6 octahedra.

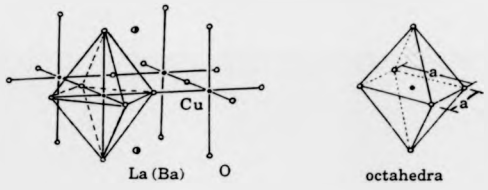

Figure 7.2a CuO_6 octahedra in tetragonal $La_{2-x}Ba_xCuO_4$.

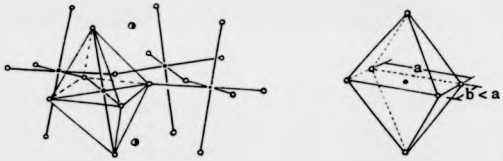

Figure 7.2b The staggered planes of CuO_6 octahedra in orthorhombic $La_{2-x}Ba_xCuO_4$.

the HTT phase down to 10 K. This conclusion was shown to be incorrect in later work by Paul et al (1987) in which the HTT to LTO phase transition was observed to occur below 180 K in a continuous manner similar to that of the parent compound. Below 75 K the orthorhombic splitting was seen to decrease so as to be unresolved by 50 K. This further transition towards a nominally tetragonal structure has resulted in the label "low temperature tetragonal" or LTT phase in more recent literature.

Jorgensen et al may have failed to observe these transitions because they only collected "several" spectra in the range 292K - 10K. This means that they were probably using 50K steps. All the spectra would have looked similar (ie. tetragonal) down to 10K except the one at about 100K (assuming one was recorded near this temperature). For $x = 0.15$ orthorhombic splitting should have been visible near 100K but they did not observe it perhaps because:

(a) No spectrum was actually recorded between 50K - 150K.

(b) A spectrum was recorded near 100K but the splitting was not noticed.

(c) The Ba content of the sample was not $x = 0.15$ but greater (ie. ~0.17). They state that the sample used had a T_c less than that of their "best" sample (33K onset rather than 35K) which supports the idea of $x \neq 0.15$. The phase diagram in figure 7.3 (from Axe et al 1989a) shows that if $x < 0.15$ they would be more likely to see the HTT - LTO transition, but if $x > 0.15$ the temperature range over which they were likely to see it reduces drastically with increasing x.

For whatever reason the HTT - LTO transition was missed, once it was missed then it becomes improbable that they should notice the slight broadening of some of the LTT phase peaks (and realize the significance)

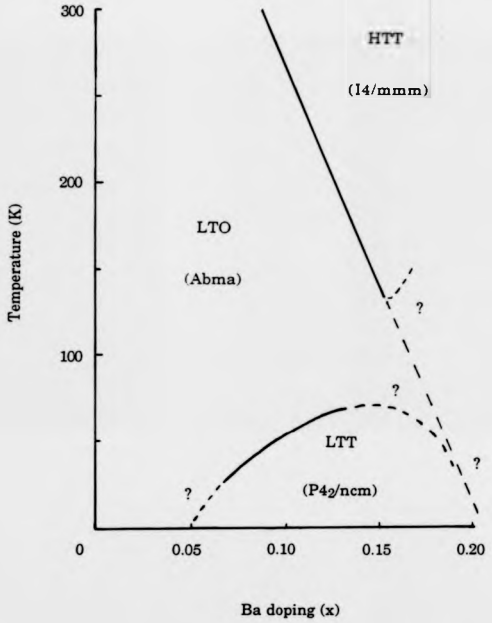

Figure 7.3 The phase diagram for $La_{2-x}Ba_xCuO_4$.

in a sample which appears to undergo no phase changes over this temperature range.

The original aim of the study presented here was to identify the LTT phase and to determine the temperature dependence of the LTO - LTT transition as a function of Ba doping. Recently Axe et al (1989a and 1989b), using high resolution X-ray and neutron diffraction, determined the structural phase diagram and reported space group $P4_2/ncm$ to be the best fit for the LTT phase. The data collected are thus examined in light of these findings. The possible role of the low temperature phase transition in the superconducting mechanism has been considered by Markiewicz (1990) and these ideas will also be discussed.

Section 7.1 Sample Preparation and Experimental Details

A range of compositions, with x values 0, 0.06, 0.1, 0.15 and 0.2, was chosen for the study. To ensure sufficient amounts for characterisation and for the neutron work, 40 g of each composition was made (Note that the x = 0.15 sample had been prepared earlier, by G. Balakrishnan for a previous study, using a similar route (Paul et al 1987)).

All the samples were prepared by a solid state reaction method. The starting materials used were high purity (at least 4 9's) powders of La_2O_3, $BaCO_3$ and CuO. For each sample, appropriate stoichiometric proportions of these were weighed out and then ground together in a mortar until a fine, uniform, grey powder was achieved. This powder was then transferred to an alumina crucible and calcined in a furnace

at 1100°C for 16 Hrs. The resulting black cake was then thoroughly re-ground and pressed into 16mm diameter pellets (roughly 3 g each). These were placed into alumina boats and sintered at 1100°C for 18 Hrs. Following this a quality check by X-ray diffraction showed insufficient phase purity. The pellets were thus re-ground, re-pelletized, and re-sintered at the same temperature for 24 Hrs. The end product was a polycrystalline ceramic material.

The sample quality was again checked using X-ray diffraction and T_c was determined by d.c. resistance (see Chapter 2 for details). A single pellet was kept for the resistance measurements but the rest of the pellets were ground to a fine powder for the X-ray and neutron diffraction work. All the samples bar the x=0 parent compound were found to superconduct with T_c's of 20, 30, 35 and 23 K respectively by d.c. resistance (ΔT_c was 5 K for all but the 0.06 sample (ΔT_c = 10 K)). The X-ray patterns showed mainly single phase materials with small impurity peaks less than 5%.

The neutron diffraction experiment was performed on HRPD (see Chapter 4 for details). Various temperature ranges were used for the different samples as determined by a number of factors. Firstly the x = 0.15 material had been studied previously by other members of the group (Paul et al 1987) over the range 10 to 200 K in 5 K steps using short (30 min.) spectra times. This work had identified the structural anomaly below 75 K and thus in the present study a restricted range (10 to 65 K in mainly 2 K steps) was used (with longer counting times) to examine this in more detail. Secondly, the parent compound had been studied extensively by others (see Jorgensen et al 1987 and references therein) so only a room temperature run was performed as a structural check. Thirdly, the present work was unfortunately broken into two parts. The

initial work was cut short by a target failure of the ISIS source. Only the work on the $x = 0.15$ sample was completed as planned. Data on the $x = 0.2$ sample were collected from 8 to 24 K (2 K steps) before loss of the beam. The second part of the work was performed after the work of others became known (for example Oh-ishi et al 1988 and especially Axe et al 1989a). The resulting knowledge of the probable phase diagram for the system (see Axe et al 1989a), and the time available, made further work on the $x = 0.2$ seem unprofitable. Thus most of the time was given over to a detailed study of the $x = 0.1$ sample (between 10 K and room temperature). Work on the $x = 0.06$ sample commenced at 5 K, the anticipated region of interest, but again the beam was lost before other temperatures could be reached. Room temperature runs were completed on all but $x = 0.15$.

Room temperature runs were performed with the samples in cylindrical vanadium cans (1cm diam. x 5cm) whilst the rest of the work was performed in rectangular cans (5cm x 3cm x 0.5cm) which were fitted with standard RAL heaters and thermometers. The front and rear surfaces of the latter were vanadium and the sides aluminium. Cooling was done in a pumped helium cryostat; the tail of which was constructed with vanadium windows specifically for neutron work. All data were obtained at the 1 m sample position in a TOF window of 30 ms to 130 ms.

Section 7.2 Results and Discussion

The present results confirm the reported phase diagram (Axe et al 1989a) for this system. The HTT - LTO and LTO - LTT phase transitions were both observed in the x = 0.1 sample (see figure 7.4). In the x = 0.06 sample the onset of the latter transition was not seen to be imminent even at 5 K as there was still a large orthorhombic splitting. It was seen, as expected, for x = 0.15 but for x = 0.2 no resolvable phase changes occurred over the ranges studied.

Rietveld profile refinement of the spectra indicated a satisfactory phase purity (see the example spectra of $La_{1.9}Ba_{0.1}CuO_4$ at 300 K figure 7.5). In Table 7.1 the χ^2 values for refinements in different space groups for each sample at selected temperatures are presented. Tables 7.2 to 7.6c give the full refined parameters at specific temperatures for some of the samples.

In the similar analysis of Axe et al (1989b) the LTT phase was refined using the tetragonal space group $P4_2/ncm$ with the lattice parameter constraint a = b removed to obtain a better fit to the anomalously broad peaks. In the present analysis this was not done as it did not seem to be justified for such a space group. The best fits for this phase therefore were all obtained at the lowest temperatures at which the LTO phase is only just resolvable (figure 7.6).

This kind of phase transition was first observed (Arend et al 1973) in $(CH_3NH_3)_2MnCl_4$. It has also been seen in the other related oxides: single crystal La_2CoO_4 (Yamada et al 1989) and the nickelates Nd_2NiO_4, Pr_2NiO_4 and La_2NiO_4 (Rodriguez-Carvajal et al 1990a and 1990b). In the

Table 7.1 Chi-Squared Values of Refinements of $La_{2-x}Ba_xCuO_4$ Spectra for Various Space Groups at Selected Temperatures.

Sample (x value)	Temp./K	Space Group	Chi-Squared
0	300	Abma	6.51
0.06	300	Abma	1.38
---	5	---	1.18
0.10	300	I4/mmm	1.07
---	250	Abma	1.35
---	200	---	1.30
---	100	---	1.57
---	50	---	1.56
---	25	---	1.64
---	---	$P4_2/ncm$	1.84
---	5	Abma	1.81
---	---	$P4_2/ncm$	1.92
0.15	65	Abma	3.79
---	---	$P4_2/ncm$	34
---	50	Abma	2.91
---	30	---	4.81
---	---	$P4_2/ncm$	6.60
---	20	Abma	3.32
---	---	$P4_2/ncm$	4.27
---	10	Abma	8.00
---	---	$P4_2/ncm$	10.83
0.20	300	I4/mmm	1.52
---	---	Abma	1.48
---	24	---	1.80
---	---	I4/mmm	1.88
---	---	$P4_2/ncm$	1.86
---	16	Abma	2.24
---	8	---	2.29

Table 7.2 Crystallographic data for $La_{1.9}Ba_{0.1}CuO_4$ at 300K

Atom	Wyckoff Symbol	x/a	y/b	z/c	B*(Å^2)	Site
La	4e	0	0	0.3617(1)	-1.50(4)	0.95
Ba	4e	0	0	0.3617(1)	-1.50(4)	0.05
Cu	2a	0	0	0	-1.38(4)	
O1	4c	0	1/2	0	-0.85(6)	1.02
O2	4e	0	0	0.1820(1)	-0.46(3)	1.00

tetragonal: space group I4/mmm (no. 139)
a=3.7897(1) c=13.2522(4) Å
* Isotropic temperature factor
Ri=25.93% Rp=15.81% Rwp=18.37% Re=17.76% χ^2=1.07

Table 7.3a Crystallographic data for $La_{1.9}Ba_{0.1}CuO_4$ at 5K (Abma)

Atom	Wyckoff Symbol	x/a	y/b	z/c	B*(Å^2)	Site
La	8f	0	0	0.3617(1)	-1.78(4)	0.95
Ba	8f	0	0	0.3617(1)	-1.78(4)	0.05
Cu	4a	0	0	0	-1.89(5)	
O1	8e	0	0	0.1828(1)	-0.79(5)	0.94
O2	8f	1/4	1/4	0	-1.99(3)	0.81

orthorhombic: space group Abma (no. 64)
a=5.3620(1) b=5.3493(1) c=13.2051(3) Å
* Isotropic temperature factor
Ri=21.07% Rp=13.02% Rwp=14.63% Re=10.87% χ^2=1.81

Table 7.3b Crystallographic data for $La_{1.9}Ba_{0.1}CuO_4$ at 5K ($P4_2/ncm$)

Atom	Wyckoff Symbol	x/a	y/b	z/c	B*(Å^2)	Site
La	8i	0.0043	0.0043	0.3613(1)	-2.41(6)	0.95
Ba	8i	0.0043	0.0043	0.3613(1)	-2.41(6)	0.05
Cu	4d	0	0	0	-2.39(5)	
O1	4e	1/4	1/4	0.0085(1)	-2.60(5)	1.03
O2	4a	3/4	1/4	0	-3.52(7)	0.59
O3	8i	-0.0227	-0.0227	0.1837(1)	-2.16(4)	0.95

tetragonal: space group P42/ncm (no. 138)
a=5.3557(1) c=13.2064(3) Å
* Isotropic temperature factor
Ri=22.00% Rp=13.82% Rwp=15.97% Re=11.30% χ^2=2.00

Table 7.4 Crystallographic data for $La_{1.94}Ba_{0.06}CuO_4$ at 5K (Abma)

Atom	Wyckoff Symbol	x/a	y/b	z/c	B*(Å^2)	Site
La	8f	0	0	0.3618(3)	-1.96(5)	0.97
Ba	8f	0	0	0.3618(3)	-1.96(5)	0.03
Cu	4a	0	0	0	-1.91(5)	
O1	8e	0	0	0.1816(2)	-1.05(3)	0.92
O2	8f	1/4	1/4	0	-0.65(3)	1.12

orthorhombic: space group Abma (no. 64)
a=5.3947(3) b=5.3342(3) c=13.1675(7) Å
* Isotropic temperature factor
Ri=27.5% Rp=15.45% Rwp=19.47% Re=17.93% χ^2=1.18

Table 7.5a Crystallographic data for $La_{1.85}Ba_{0.15}CuO_4$ at 10K (Abma)

Atom	Wyckoff Symbol	x/a	y/b	z/c	B*(Å^2)	Site
La	8f	0	0	0.3604(2)	-1.05(4)	0.925
Ba	8f	0	0	0.3604(2)	-1.05(4)	0.075
Cu	4a	0	0	0	-1.35(4)	
O1	8e	0	0	0.1833(1)	0.03(6)	1.00
O2	8f	1/4	1/4	0	-1.09(3)	0.94

orthorhombic: space group Abma (no. 64)
a=5.353(2) b=5.350(2) c=13.3201(2) Å
* Isotropic temperature factor
Ri=13.73% Rp=7.09% Rwp=8.51% Re=3.01% χ^2=8.00

Table 7.5b Crystallographic data for $La_{1.85}Ba_{0.15}CuO_4$ at 5K ($P4_2/ncm$)

Atom	Wyckoff Symbol	x/a	y/b	z/c	B*(Å^2)	Site
La	8i	0.0042	0.0042	0.3605(2)	-1.43(4)	0.925
Ba	8i	0.0042	0.0042	0.3605(2)	-1.43(4)	0.075
Cu	4d	0	0	0	-1.49(4)	
O1	4e	1/4	1/4	0.0058(1)	-1.38(5)	1.09
O2	4a	3/4	1/4	0	-1.88(6)	0.72
O3	8i	-0.0241	-0.0241	0.1832(1)	-1.22(4)	0.97

tetragonal: space group P42/ncm (no. 138)
a=5.35541(2) c=13.206543(5) Å
* Isotropic temperature factor
Ri=10.83% Rp=8.13% Rwp=10.72% Re=3.06% χ^2=12.30

Table 7.6a Crystallographic data for $La_{1.8}Ba_{0.2}CuO_4$ at 24K (Abma)

Atom	Wyckoff Symbol	x/a	y/b	z/c	B*(Å^2)	Site
La	8f	0	0	0.3600(3)	-1.08(3)	0.9
Ba	8f	0	0	0.3600(3)	-1.08(3)	0.1
Cu	4a	0	0	0	-1.21(4)	
O1	8e	0	0	0.1819(2)	-0.47(3)	0.96
O2	8f	1/4	1/4	0	-0.92(4)	0.97

orthorhombic: space group Abma (no. 64)
a=5.34253(5) b=5.33875(5) c=13.28201(7) Å
* Isotropic temperature factor
Ri=12.54% Rp=7.65% Rwp=7.81% Re=5.82% χ2=1.80

Table 7.6b Crystallographic data for $La_{1.8}Ba_{0.2}CuO_4$ at 24K ($P4_2/ncm$)

Atom	Wyckoff Symbol	x/a	y/b	z/c	B*(Å^2)	Site
La	8i	0.0023	0.0023	0.3604(3)	-1.25(4)	0.9
Ba	8i	0.0023	0.0023	0.3604(3)	-1.25(4)	0.1
Cu	4d	0	0	0	-1.24(4)	
O1	4e	1/4	1/4	0.0041(1)	-0.70(3)	1.12
O2	4a	3/4	1/4	0	-2.38(7)	0.68
O3	8i	-0.010	-0.010	0.1814(2)	-0.86(3)	0.92

tetragonal: space group P42/ncm (no. 138)
a=5.34062(3) c=13.28199(7) Å
* Isotropic temperature factor
Ri=12.16% Rp=7.91% Rwp=8.08% Re=5.92% χ2=1.86

Table 7.6c Crystallographic data for $La_{1.8}Ba_{0.2}CuO_4$ at 24K (I4/mmm)

Atom	Wyckoff Symbol	x/a	y/b	z/c	B*(Å^2)	Site
La	4e	0	0	0.3600(2)	-1.11(3)	0.9
Ba	4e	0	0	0.3600(2)	-1.11(3)	0.1
Cu	2a	0	0	0	-1.24(4)	
O1	4c	0	1/2	0	-0.90(3)	0.98
O2	4e	0	0	0.1819(1)	-0.45(3)	0.97

tetragonal: space group I4/mmm (no. 139)
a=3.77640(2) c=13.28203(6) Å
* Isotropic temperature factor
Ri=12.68% Rp=7.81% Rwp=8.00% Re=5.82% χ2=1.89

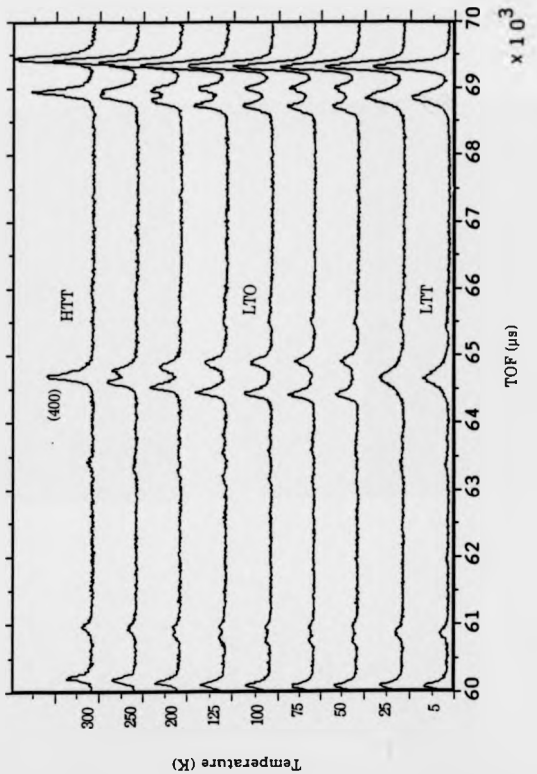

Figure 7.4a The HTT - LTO and LTO - LTT phase transitions in $La_{1.9}Ba_{0.1}CuO_4$ — note the broad peaks of the LTT phase.

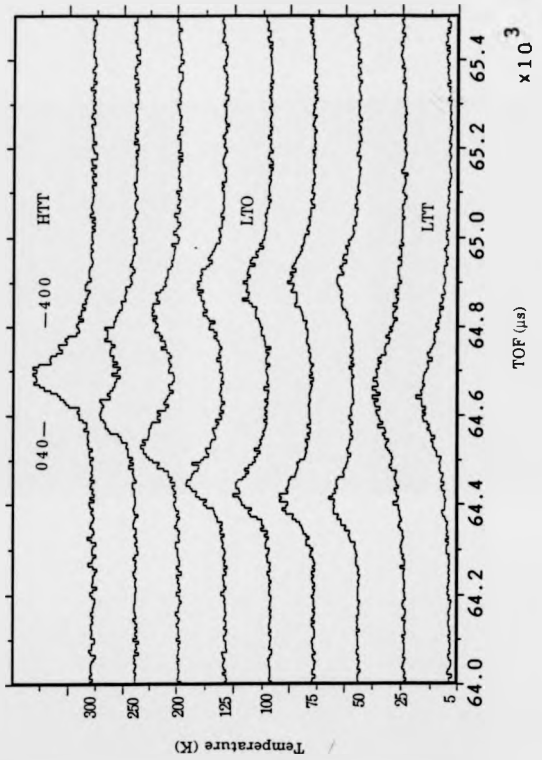

Figure 7.4b As for 7.4a but over a resticted range of TOF to concentrate on the 040/400 splitting.

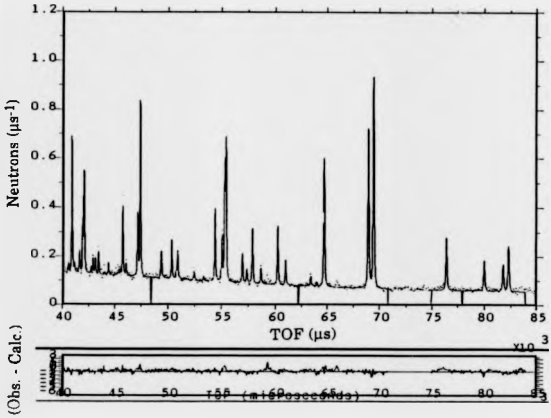

Figure 7.5 Rietveld profile refinement of $La_{1.9}Ba_{0.1}CuO_4$ at 300K. The solid line is the fit to the observed data (points). The difference (Obs. - Calc.) is given below.

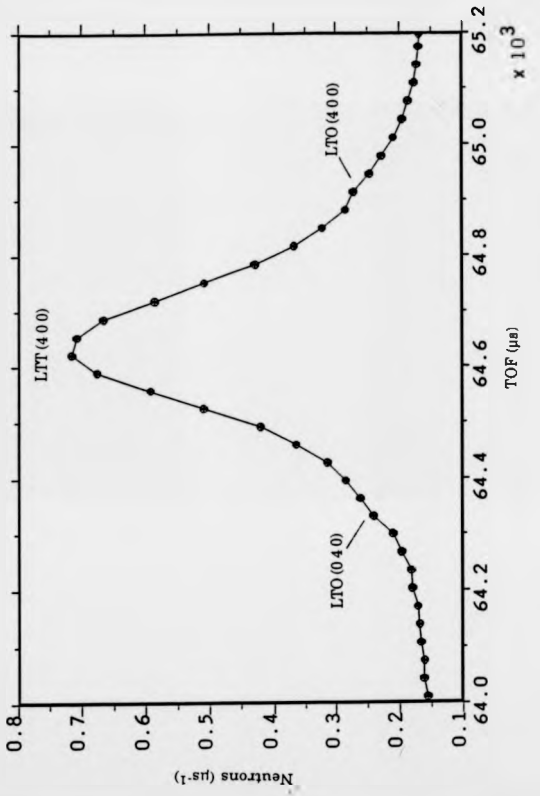

Figure 7.6 $La_{1.85}Ba_{0.15}CuO_4$ at 10K concentrating on the 400 peak of the LTT phase with the LTO phase just resolved. The points are observed data — the line is only a guide for the eye.

latter case the strong anisotropic peak broadening in the neutron diffraction pattern of the LTT phase has been described by Rodriguez-Carvajal et al (1990b) as resulting from frozen-in microstrains which accompany the transition from the LTO phase. They give details of a simple model for fitting the broadening in the refinement process which involves the addition of only one extra parameter. In this model the local cells are orthorhombic but the average fluctuations of a and b about the mean tetragonal cell parameter (a_T) are the same in both the x- and y-directions to give an overall tetragonal symmetry. This method would almost certainly improve the fit for the $P4_2/ncm$ space group in the samples of this study, however there is a coexistence of the LTO phase seen in the spectrum. The refinement software is "single phase" and would thus not do justice to the improved method of fitting one of the two phases present.

The orthorhombic strain for x = 0.1 over the range 5 - 300 K was found to be in agreement with the results of Axe et al (1989b) indicating that the onset of the LTO - LTT phase transition for this compound is near 60 K. A similar behaviour was previously observed for x = 0.15 by Paul et al (1987) and was also seen in this study. In both cases the onset (decrease in orthorhombic strain) occurs well above T_c but the the new LTT phase is seen to become dominant in the region of T_c (see figures 7.7 and 7.8).

For the other two superconducting compositions the situation is not as clear. Moss et al (1987) examined the x = 0.2 system using high resolution X-ray diffraction and concluded that there was a coexistence of two tetragonal phases of very similar lattice parameter and that a good fit to the data could not be made using a single phase. At low temperatures (10 K) they also introduced a monoclinic distortion to

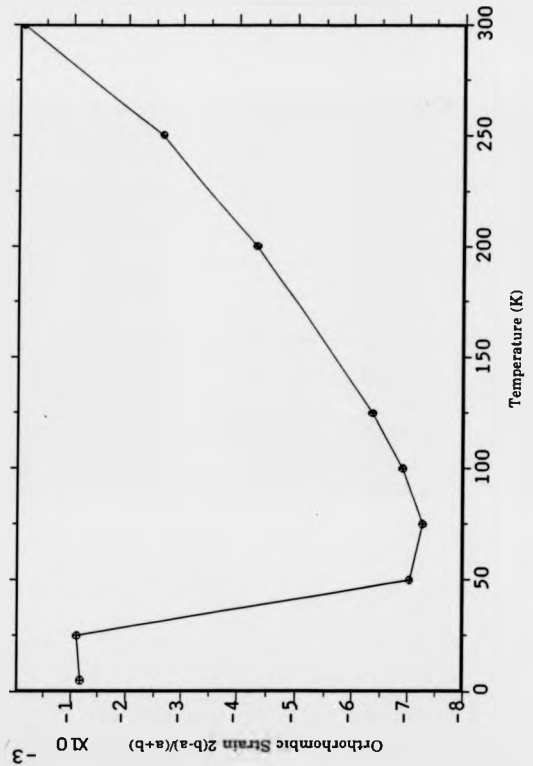

Figure 7.7 Orthorhombic strain as a function of temperature for $La_{1.9}Ba_{0.1}CuO_4$.

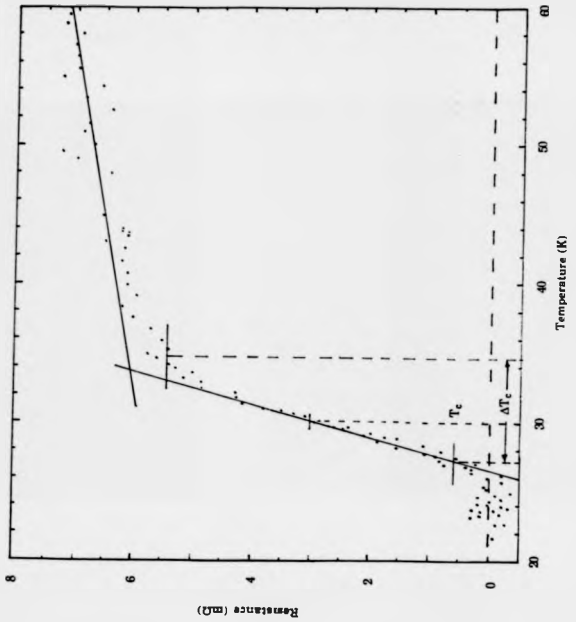

Figure 7.8 Resistance against temperature (showing T_c) for $La_{1.9}Ba_{0.1}CuO_4$.

account for the increased peak widths. In the present study attempts to refine profiles as I4/mmm, Abma and $P4_2/ncm$ all gave similar (reasonably good: $\chi^2 \sim 1.8$) results which did not indicate the presence of the two phases or the low temperature distortion. Fortuitously the single low temperature spectrum collected for x = 0.06 at 5 K (figure 7.9) showed no sign of the LTT phase and thus puts a tight upper limit on the LTO - LTT transition in this sample (if there is one).

A more recent high resolution XRD study of this system over the range x=0.088 to x=0.14 (Momono et al 1991) confirms that the LTO and LTT phases coexist at low temperatures for these doping levels.

The HTT - LTO transition is accompanied by a change of axes; the LTO a-b axes are designated by the HTT [110] directions. The two LTO variants are formed by the rotation of the corner shared CuO_6 octahedra about the (110) or (1-10) HTT axes. The primitive LTO cell also contains two formula units rather than one. The LTO - LTT transition retains the same axes but is accompanied by a further doubling of the number of formula units in the primitive cell.

The phase transitions in this system are described by Axe et al (1989a,b) using a Landau-Ginzburg free-energy function. They construct this using primary order parameters Q_1 and Q_2, and secondary order parameter, η. The orthorhombic strain $\eta = (a-b)/(a+b)$, and the Q's are the amplitudes of a degenerate pair of soft phonons in the HTT phase along the (110) and (1-10) axes respectively. In a simple analysis they minimise the function for temperatures below the transition and find only two stable regions in (u,v) space. The first corresponds to the LTO phase: $v < 0$, $(u+v) > 0$ and Q1 or Q2 separately non-zero (giving the twin modifications of the LTO structure). The second corresponds to the LTT

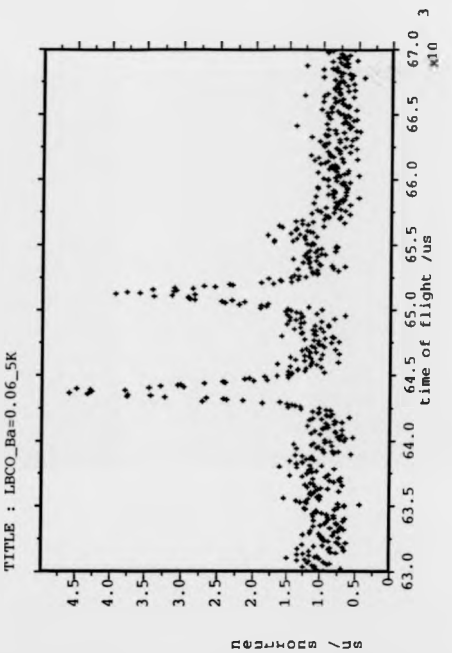

Figure 7.9 $La_{1.94}Ba_{0.06}CuO_4$ at 5K. This spectrum clearly resolves the orthorhombic splitting of the 040/400 LTO peaks and shows no sign of the LTT phase.

phase: $v > 0$, $(2u+v) > 0$ and $|Q1|=|Q2|$. This represents a coherent superposition of the LTO twins.

A more precise analysis is used (Axe et al 1989b) when they consider the LTO - LTT phase boundary (where $v \rightarrow 0$) in more detail. For this they include higher order anisotropy terms ($\sim Q^8$). They show that the transition may be first order (discontinuous) but do not rule out that the boundary may be split by a new phase — identified as Pccn (a subgroup) of both the LTO and LTT phases). This would be stable over a limited range of v and the LTO - Pccn and Pccn - LTT transitions would both be continuous. The recent work (mentioned above) of Momono et al (1991) supports the idea of the formation of a Pccn phase and suggests that its orthorhombicity may depend on Ba concentration.

While the HTT - LTO transition is present in the closely related compound $La_{2-x}Sr_xCuO_4$ (see Day et al 1987, Fleming et al 1987 and Onoda et al 1987) the LTO - LTT transition is not seen (however the orthorhombic distortion does decrease below 20K for (Sr) $x = 0.15$ (Day et al 1987)). The maximum T_c as a function of Sr doping occurs at $x = 0.15$ (for example see Oh-Ishi et al 1988) but no "dip" in the T_c against x curve is present as it is for La-Ba-Cu-O (Axe et al 1989a, Suzuki and Fujita 1989). It may not be coincidence that both the LTT phase and the dip in T_c are present only in the Ba system. Axe et al (1989a) have determined that the maximum concentration of the LTT phase coincides with the T_c minima near $x = 0.125$, and they conclude the formation of this phase is detrimental to the superconductivity. They give some possible explanations ranging from substantial changes in electronic structure to changes in the interplanar magnetic coupling (possibly responsible for the superconducting pairing).

The role of the LTT phase is considered in depth by Markiewicz (1990). He builds on his earlier work (1989a) in which he proposes an excitonic model for superconductivity in the high - T_c - oxides. It relies on the existence of a van Hove singularity (VHS) in a single band (the CuO_2 - antibonding band of the planes). The VHS occurs at the point where the Fermi Surface touches the Brillouin zone boundary and leads to a separation of the Cu - O_2 plane carriers into "heavy holes" (a high density of states (DOS) region near the Brillouin zone boundaries) and "light holes" (a low DOS region over the rest of the Brillouin zone). The heavy holes are localised into a charge density wave (CDW) and the virtual excitations across the CDW gap result in the pairing of the (superconducting) light holes. The model does not demand long range CDW order but only the presence of short range CDW order.

In his consideration of La - (Ba, Sr) - Cu -O, Markiewicz (1990) points out that when the VHS is exactly at the Fermi level (for the Cu -O_2 antibonding band) the situation is a 2-dimensional analogue of the Bilbro - McMillan (1976) model of superconductivity in the A15 compounds. Their model showed that there could be competition between superconductivity and the formation of CDW's (onset of a structural instability) with both energy gaps competing for a common portion of the Fermi Surface. The establishment of long range CDW order was shown to destroy the superconductivity. Markiewicz (1990) concludes that the CDW would have the smallest gap in the material (for La - Ba - Cu - O) making it ideal for the pairing he suggested previously (1989a). With reference to Axe et al (1989a) he notes that the LTO - LTT transition disrupts the spatial symmetry of the oxygen atoms in the CuO_2 planes and thus splits the VHS. This leads to the formation of long range CDW

order (owing to a partial dimerisation of the apical oxygens) and thus to the reported reduction in T_c.

In the case of La - Sr - Cu - O there is no transition to a LTT phase but, as stated above, there is a reduction of the orthorhombic distortion at low temperature (Day et al 1987) which would be demanded by the strong short range CDW order of Markiewicz's model. His theory is an interesting variation of the idea of excitonic mediated pairing. It helps to explain much of the experimental data for these compounds (for a more detailed discussion see Markiewicz 1989a, 1990) and helps to build a more general picture of the behaviour of the high T_c and related compounds. However, as with most other high T_c theories convincing calculations of T_c are yet to be made (Markiewicz 1989b) and it is unclear how well it can be applied to the other families of the high T_c Oxides.

Very recently Wu et al (1992) have proposed a possible mechanism for structural phase transitions in $La_{2-x}M_xCuO_4$ (M = Ba, Sr). This considers the influence of electron correlations on the Jahn-Teller induced structural phase transition and seems to account for the general features observed in this system to date. They do not, however, exclude the possibility of a magnetic fluctuation - induced structural instability and conclude that the real mechanism for the HTT - LTO transition in LBCO is still to be determined.

Conclusions

The existence of a LTT phase for $La_{2-x}Ba_xCuO_4$ is confirmed for $x > 0.06$ and $x < 0.2$. Below its onset, the LTT phase coexists with the LTO phase and becomes dominant at lower temperatures. The best fit to the LTT phase is space group $P4_2/ncm$. This is concluded despite the slightly better χ^2 for Abma (for low temperature spectra: x=0.1) because the calculated Abma profiles give clearly split peaks in contrast to the single (but broad) peaks observed. The anomalously broad tetragonal peaks are almost certainly due to frozen-in microstrain (analogous to the La - nickelates — Rodriguez-Carvajal et al 1990b).

La_2CuO_4 is confirmed to be orthorhombic (space group Abma) at room temperature. $La_{2-x}Ba_xCuO_4$ undergoes a HTT to LTO phase transition for $x \geq 0.06$ and $x < 0.2$ in the range 300K - 5K. The onset temperature decreases with increasing Ba substitution. The space groups are confirmed to be I4/mmm and Abma for the HTT and LTO phases respectively.

At temperatures below the HTT - LTO transition the onset of a second, LTO - LTT, transition occurs for $x > 0.06$ and $x < 0.2$. After the onset of this transition the LTO and LTT phases coexist with the LTT phase becoming dominant as temperature is reduced. The maximum onset temperature for the LTO - LTT transition observed in this study occurred for $x = 0.15$; the sample with the highest superconducting transition temperature (35K). This finding alone would suggest that the LTT phase has a beneficial effect on the superconductivity in these materials. However it could be reasoned that it is not crucial to the

superconductivity as the LTT phase is not observed at 5K in the $x = 0.06$ sample which has a T_c of 20K.

The results of this study are supported and extended by the later work of others (see especially Axe et al 1989a,b and Suzuki and Fujita 1989). The most interesting observation reported is the sharp dip in T_c for $0.1 < x < 0.15$ — the region in which the LTO - LTT onset temperature is highest. This indicates that the LTT phase is detrimental to superconductivity. An explanation of why this is so is given by Markiewicz (1990).

The fact remains that this sequence of transitions has been observed in other (non-superconducting) compounds (see § 7.2) and that there is not a definite relationship between superconductivity and the presence/absence of the LTT phase in La-Ba-Cu-O. When the LTT phase is not present samples may still have relatively high T_c's (20K for $x = 0.06$) and when it is, the T_c's may be high or low. It can be concluded from the evidence that both the LTO and LTT phases are superconducting.

CHAPTER 8

THE CRYSTAL STRUCTURE OF $Nd_{2-x}Ce_xCuO_4$

Introduction

The initial reports (Tokura et al 1989 and Takagi et al 1989) of superconductivity in the Ce doped Nd_2CuO_4 system aroused great interest as it was claimed that this was the first high T_c material in which the carriers had negative charge (n-type). There are some resemblances to the doped La_2CuO_4 superconductors (see Chapter 7); the optimum T_c (near 24K) is attained for a doping level of $x \sim 0.15$ and the structure again includes Cu-O planes in a similar unit cell. However, the range of doping which produces superconductivity is more restricted ($x = 0.14$ to $x = 0.18$), the samples must also be annealed in a reducing (argon) atmosphere and the superconducting transition is sharper in magnetic susceptibility measurements. It is reported that T_c is relatively insensitive to changes in oxygen deficiency (y) between 0.02 and 0.22 in $Nd_{1.85}Ce_{0.15}CuO_{4-y}$ (Degiorgi et al 1989).

The structure is not identical to the La-Cu oxides however. This fact was reported for the parent compound in 1975 (Muller-Bushbaum and Wollschlager). Nd_2CuO_4 was identified as having the same tetragonal symmetry (space group I4/mmm) as the HTT phase of La_2CuO_4 but it lacks the apical oxygens associated with the Cu-O planes (see figure 8.1). This structure is referred to as the "T' phase" in the

$Nd_{2-x}\ Ce_x\ Cu\ O_4$

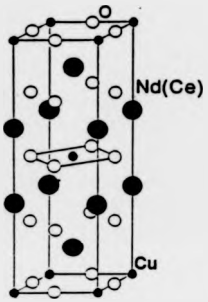

Figure 8.1 The structure of $Nd_{2-x}Ce_xCuO_4$ (T' phase). Note the lack of apical oxygens on the Cu-O planes — contrast with figure 7.1.

literature (Tokura et al 1989). It has been suggested by Emery (1989) that these oxygens, with negative charge, help to trap holes in the Cu-O planes in other oxide superconductors (p-type). Their absence in the Nd compounds might therefore be expected if they really are n-type. This feature has not gone unquestioned in the literature and the argument is commented upon by Takahashi et al (1990) who conclude in favour of n-type superconductivity.

This chapter is concerned with the results of a high resolution neutron diffraction study of the $Nd_{2-x}Ce_xCuO_{4-y}$ system. The work was undertaken to search for any structural changes which may be associated with the onset of superconductivity/ level of doping, as have been reported in the doped La-Cu oxides (see Chapter 7).

Section 8.1 Sample Preparation and Experimental Details

The samples for this study were prepared by S. M. Doyle and D. S. Misra, by a solid state route described elsewhere (Boothroyd et al 1990), with a range of compositions: $x = 0$, 0.12, 0.15, and 0.2. X-ray powder diffraction indicated high phase purity and a maximum T_c (for $x = 0.15$) of 21K (Boothroyd et al 1990).

Neutron diffraction was performed on all the samples using HRPD. Roughly 8g of powder was loaded into rectangular cross section cans which were cooled in a cryostat, as required, from room temperature to 5K (all as described in §7.1). Room temperature spectra were collected to cover an extensive range in d-spacing using two TOF windows (12 - 112ms and 95 - 195ms) for both of the extreme

compositions, x = 0 and x = 0.2, to enable a proper comparison between the doped and undoped structures to be performed. For the intermediate compositions only the shorter TOF window was used. For the low temperature runs a more restricted window (25 - 65ms) was chosen so as to maximize the resolution, for the planned number of spectra, in the time available.

The sample of greatest interest was naturally that with the highest T_c (x = 0.15). This was allocated the largest proportion of time and spectra were collected from 5 - 120K in 5K steps allowing 12μA beam for each. The other two doped samples were given less time. For x = 0.2 only 8μA per spectra was allotted for a similar survey ending at 75K. The x = 0.12 sample was again given 12μA per spectra but over the restricted range 5 - 35K. The undoped compound was not studied at low temperatures.

Section 8.2 Results and Discussion

The only clear difference between samples was the slight change in lattice parameters with Ce doping, as all displayed the same T′ structure as the parent (x = 0) compound. It was found that **a** became longer while **c** became shorter as Ce doping was increased. The samples all had a high degree of phase purity estimated to be better than 99% (see figures 8.2a,b for example spectra). All the spectra were refined as space group I4/mmm and selected results are given for each compound in tables 8.1 to 8.3. No phase changes were observed in any sample over the temperature ranges studied and the lattice parameters, **a** and **c**,

Table 8.1a Crystallographic data for $Nd_{1.8}Ce_{0.2}CuO_4$ at 5K

Atom	Wyckoff Symbol	x/a	y/b	z/c	B*(Å^2)	Site
Nd	4e	0	0	0.3530(1)	-0.46(2)	0.9
Ce	4e	0	0	0.3530(1)	-0.46(2)	0.1
Cu	2a	0	0	0	-0.44(2)	
O1	4c	0	1/2	0	-0.42(2)	0.87
O2	4d	0	1/2	1/4	-0.30(1)	0.92

tetragonal: space group I4/mmm (no. 139)
a=3.9411(1) c=12.0229(4) Å
* Isotropic temperature factor
Ri=75.57% Rp=12.02% Rwp=13.31% Re=11.75% χ2=1.28

Table 8.1b Crystallographic data for $Nd_{1.8}Ce_{0.2}CuO_4$ at 75K

Atom	Wyckoff Symbol	x/a	y/b	z/c	B*(Å^2)	Site
Nd	4e	0	0	0.3528(1)	-0.39(1)	0.9
Ce	4e	0	0	0.3528(1)	-0.39(1)	0.1
Cu	2a	0	0	0	-0.29(1)	
O1	4c	0	1/2	0	-0.18(1)	0.94
O2	4d	0	1/2	1/4	-0.19(1)	0.97

tetragonal: space group I4/mmm (no. 139)
a=3.9416(2) c=12.0241(5) Å
* Isotropic temperature factor
Ri=66.79% Rp=13.64% Rwp=14.99% Re=14.91% χ2=1.01

Table 8.2a Crystallographic data for $Nd_{1.85}Ce_{0.15}CuO_4$ at 4K

Atom	Wyckoff Symbol	x/a	y/b	z/c	B*(Å^2)	Site
Nd	4e	0	0	0.3526(1)	-0.48(2)	0.925
Ce	4e	0	0	0.3526(1)	-0.48(2)	0.075
Cu	2a	0	0	0	-0.25(1)	
O1	4c	0	1/2	0	-0.36(1)	0.88
O2	4d	0	1/2	1/4	-0.24(1)	0.96

tetragonal: space group I4/mmm (no. 139)
a=3.9400(1) c=12.0536(3) Å
* Isotropic temperature factor
Ri=51.10% Rp=11.27% Rwp=12.15% Re=11.62% χ2=1.09

Table 8.2b Crystallographic data for $Nd_{1.85}Ce_{0.15}CuO_4$ at 20K

Atom	Wyckoff Symbol	x/a	y/b	z/c	B*(Å^2)	Site
Nd	4e	0	0	0.3526(1)	-0.47(2)	0.925
Ce	4e	0	0	0.3526(1)	-0.47(2)	0.075
Cu	2a	0	0	0	-0.28(1)	
O1	4c	0	1/2	0	-0.32(1)	0.91
O2	4d	0	1/2	1/4	-0.33(1)	0.95

tetragonal: space group I4/mmm (no. 139)
a=3.9400(1) c=12.0535(3) Å
* Isotropic temperature factor
Ri=40.40% Rp=11.42% Rwp=12.15% Re=11.72% χ2=1.07

Table 8.2c Crystallographic data for $Nd_{1.85}Ce_{0.15}CuO_4$ at 120K

Atom	Wyckoff Symbol	x/a	y/b	z/c	B*(Å^2)	Site
Nd	4e	0	0	0.3524(1)	-0.31(1)	0.925
Ce	4e	0	0	0.3524(1)	-0.31(1)	0.075
Cu	2a	0	0	0	-0.20(1)	
O1	4c	0	1/2	0	-0.30(1)	0.87
O2	4d	0	1/2	1/4	-0.06(1)	0.98

tetragonal: space group I4/mmm (no. 139)
a=3.9414(1) c=12.0583(3) Å
* Isotropic temperature factor
Ri=50.04% Rp=11.96% Rwp=12.477% Re=12.08% χ2=1.07

Table 8.3a Crystallographic data for $Nd_{1.88}Ce_{0.12}CuO_4$ at 5K

Atom	Wyckoff Symbol	x/a	y/b	z/c	B*(Å^2)	Site
Nd	4e	0	0	0.3519(1)	-0.63(2)	0.94
Ce	4e	0	0	0.3519(1)	-0.63(2)	0.06
Cu	2a	0	0	0	-0.41(2)	
O1	4c	0	1/2	0	-0.54(2)	0.88
O2	4d	0	1/2	1/4	-0.29(1)	0.99

tetragonal: space group I4/mmm (no. 139)
a=3.9391(1) c=12.0760(3) Å
* Isotropic temperature factor
Ri=45.91% Rp=11.34% Rwp=11.89% Re=11.04% χ2=1.16

Table 8.3b Crystallographic data for $Nd_{1.88}Ce_{0.12}CuO_4$ at 30K

Atom	Wyckoff Symbol	x/a	y/b	z/c	B*($Å^2$)	Site
Nd	4e	0	0	0.3517(1)	-0.78(2)	0.94
Ce	4e	0	0	0.3517(1)	-0.78(2)	0.06
Cu	2a	0	0	0	-0.44(2)	
O1	4c	0	1/2	0	-0.54(2)	0.93
O2	4d	0	1/2	1/4	-0.31(1)	1.02

tetragonal: space group I4/mmm (no. 139)
a=3.9389(2) c=12.0747(5) Å
* Isotropic temperature factor
Ri=12.41% Rp=13.57% Rwp=15.19% Re=14.95% $\chi 2$=1.03

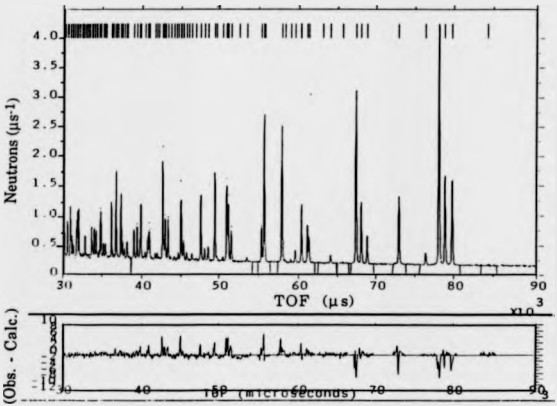

Figure 8.2a Rietveld profile refinement of $Nd_{1.85}Ce_{0.15}CuO_4$ at 300K. The solid line is the fit to the observed data (points). The ticks indicate the peak positions expected from the refinement and the difference (obs. - Calc.) is also given.

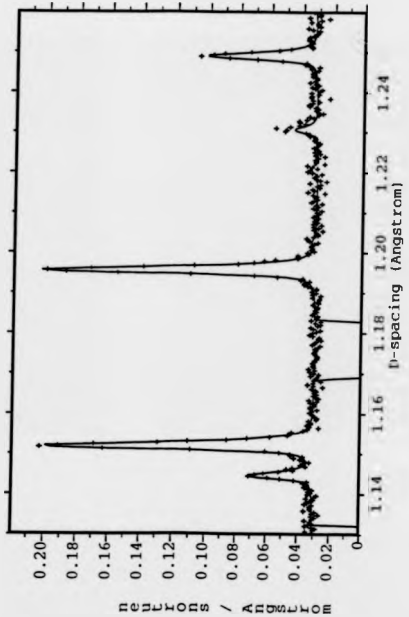

Figure 8.2b Rietveld profile refinement of $Nd_{1.8}Ce_{0.2}CuO_4$ at 75K. The solid line is the fit to the observed data (points).

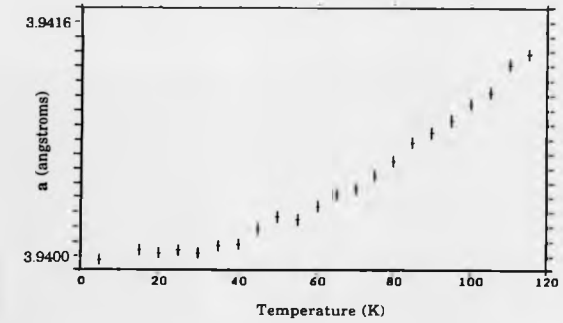

Figure 8.3a Lattice parameter a as a function of temperature for $Nd_{1.85}Ce_{0.15}CuO_4$.

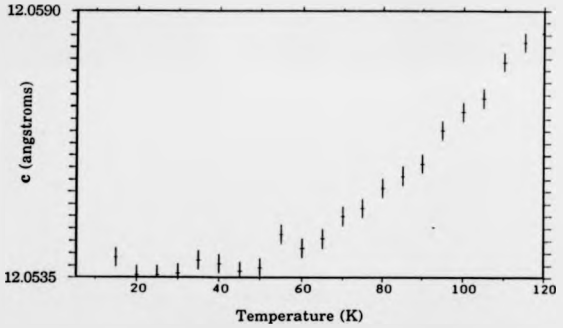

Figure 8.3b Lattice parameter c as a function of temperature for $Nd_{1.85}Ce_{0.15}CuO_4$.

decrease smoothly with reducing temperature (see for example figure 8.3).

It is interesting to note that these results, which contrast this material with doped La_2CuO_4 (Chapter 7), are not the only "null" results for Nd-Ce-Cu-O. Murayama et al (1989) report the absence of any pressure effect on T_c for $Nd_{1.85}Ce_{0.15}CuO_{4-y}$. This is in contrast to the large positive value of the pressure coefficient for the other (p-type) superconductors. They note the main structural difference between Nd-Ce-Cu-O and the other superconductors is the lack of apical oxygens associated with the Cu-O planes and thus conclude that it is changes in the apical oxygen - plane distance which accounts for the pressure effect in the other superconductors.

In later work by Kobayashi et al (1991) on the related compounds, Ln-Ce-Cu-O (Ln = Pr and Sm), it is reported that both **a** and **c** increase with Ce doping at room temperature. This is in contrast to the results of this study at low temperatures.

Some workers have reported that Nd-Ce-Cu-O is subject to phase separation with the only true single phase compositions being x=0 and x=0.165 (see for example Chen et al 1989, Jorgensen et al 1990 and Lightfoot et al 1990). All other nominal dopings are just mixtures of these two phases. The neutron diffraction data presented by the latter group shows this clearly for x=0.13. The validity of these findings has been called into question by others (see Rosseinsky et al 1989 and Rosseinsky and Prassides 1991) who have prepared single phase samples at other values of x (as determined by high resolution neutron diffraction) up to x=0.07. They suggest that single phase samples may be possible at higher x if preparation is performed carefully.

The present study was undertaken before such ideas were published and hence the data collection was not tailored to look for these effects. The results of Lightfoot et al (1990) indicate that the major difference between the two phases is the length of **c** — hence they illustrate the phase separation by concentrating on the splitting of the 0 0 8 peak. The "x=0.165" phase has the smaller **c** and appears as a low intensity shoulder on the small d-spacing side of the main phase peak. The splitting is greatest for small **x** and is unresolved for x>0.165. If phase separation is occurring, then the x=0.12 sample should show the greatest peak separation of those studied. The available hkl reflections with h=k=0 all have relatively low intensity (less than 10% of that of the major peaks) over the TOF window used. The most prominent of these is the 0 0 12 peak which is illustrated in figure 8.4. The expected splitting for this peak would be ~0.003Å based on fig.3b of Lightfoot et al (1990). The low number of counts makes the peak difficult to find without the aid of its calculated profile and it does not provide evidence for/against phase separation. A hint of possible phase separation can be seen in the 2 0 8 peak (chosen because it is quite isolated) when it is compared with the equivalent peaks for x=0, 0.15 and 0.2 — see figure 8.5. The predicted splitting for x=0.12 is ~0.002Å and although no shoulder is resolved on the peak there does appear to be more intensity in the low d-spacing wing (compared to those with other **x**) which might be produced by a second, overlapping, small peak.

It should be noted that the predicted splittings are based on the room temperature spectra collected by Lightfoot et al (1990) and the actual splitting at 30K for x=0.12 may be much less. However if both phases show the same temperature dependence of **c** (a ~0.05% decrease from 300K to 30K) there would not be an appreciable change in splitting.

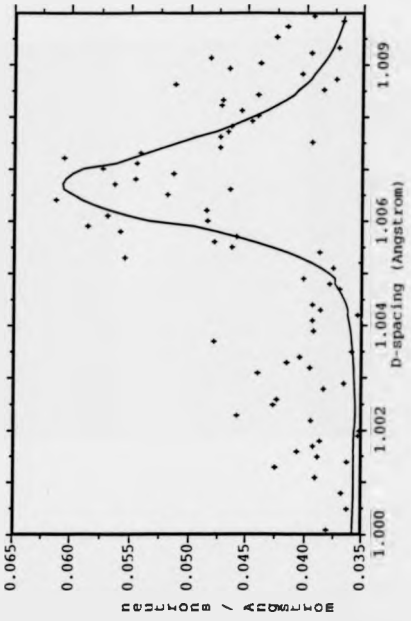

Figure 8.4 The 0 0 12 peak of $Nd_{1.88}Ce_{0.12}CuO_4$ at 30K (+: raw data, —: fit).

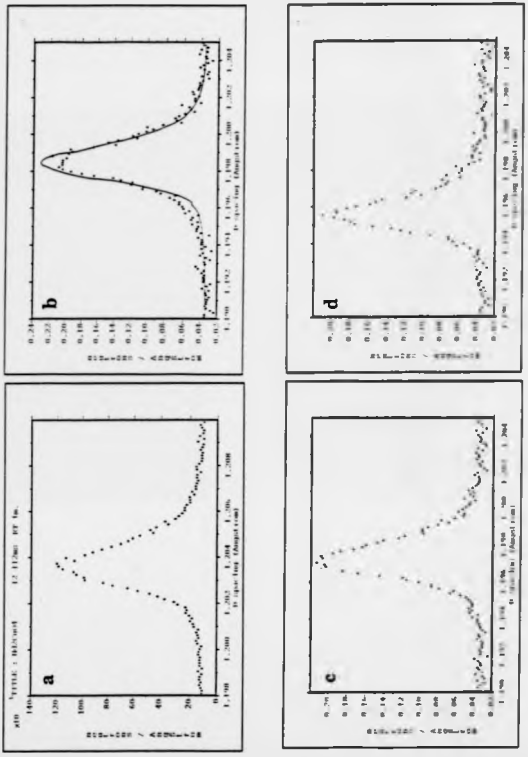

Figure 8.5 The 2 0 8 peak for each sample: (a) x=0 at 300K, (b) x=0.12 at 30K, (c) x=0.15 at 20K and (d) x=0.2 at 75K. Note the more pronounced low d-spacing wing for x=0.12.

The lack of a resolved shoulder on the 2 0 8 peak may thus militate against phase separation.

There have been other recent reports of a local structural change close to T_c in Nd-Ce-Cu-O. Billinge et al (1991) carried out pair distribution function analysis of neutron powder diffraction data (for x=0.165) and found that the local atomic structure is significantly distorted from T'. Evidence was lacking for such changes in a high resolution synchrotron XRD study for a single crystal, with x=0.15, performed by Bordet et al (1991).

Conclusions

It is clear that Ce doped Nd_2CuO_{4-y} does not undergo any resolvable structural changes (except for lattice contraction with cooling),at the values of x investigated, over the low temperature ranges studied. There is no convincing evidence of phase separation in these samples but local structural changes near T_c cannot be ruled out from the results of this study.

At low temperature and room temperature $Nd_{2-x}Ce_xCuO_4$ has the same tetragonal structure as the undoped parent compound: space group I4/mmm.

The amount of Ce doping is definitely crucial to superconductivity (as is oxygen deficiency) however in the range which produces superconducting samples there is little structural difference to the non-

superconducting doped samples. Any theory for superconductivity in these compounds thus needs to account for this.

It is interesting to note that the absence of a pressure effect on T_c indicates a role for the apical oxygen - Cu-O plane distance in the superconductivity of other superconductors (see § 8.2). This makes the the formulation of a general theory for superconductivity in these materials more difficult.

The lack of apical oxygens does not however cause any problems with Markiewicz's theory (1990) for the phase diagram of La-Ba-Cu-O (see Chapter 7). In his theory the apical oxygens play a crucial role in the phase changes in that compound — the lack of any phase change in Nd-Ce-Cu-O would thus be expected given the lack of apical oxygens.

There has been clear evidence of phase separation in similar samples prepared by others (see §8.2 references) and there has also been a preliminary attempt to explain this using a simple Huckle model (Baird and Burdett 1990). The lack of support from other studies (including this one) may indicate that very careful sample preparation is required in this system as is the case for other high-T_c materials.

CHAPTER 9

CRYSTAL FIELD EFFECTS IN $Pr_{1-x}Y_xBa_2Cu_3O_{7-\delta}$

Introduction

As noted in the Introduction to this thesis, Pr is the only rare earth (R) which, when substituted for Y in $YBa_2Cu_3O_7$, forms the single phase 123 structure (see figure 9.1) without also being a superconductor. In fact superconductivity is suppressed completely in the $Pr_{1-x}Y_xBa_2Cu_3O_7$ system when the Y content is reduced below roughly 40%. A clear explanation of why Pr is unique in having this effect may aid the understanding of the general nature of superconductivity in the new materials.

In conventional superconductors the substitution of a magnetic ion, such as Pr, would be expected to disrupt the superconductivity by breaking up the Cooper pairs (the interaction energy with the ion's spin for each member of the pair would be different). The fact that other magnetic R, such as Ho, Nd, Er and Gd, do not noticeably affect the high T_c of the 123 phase indicates that the effect of Pr substitution may be more subtle. A magnetic effect cannot be ruled out however as the decrease of T_c, with increased Pr concentration in Pr/Y-123, does seem to follow the theoretical magnetic pair-breaking model put forward by Abrikosov and Gor'kov (1961). Pr is also seen to order magnetically at a much higher temperature than other magnetic R — 17 K rather than below 2K (Li et al 1989). This, combined with a large electronic specific

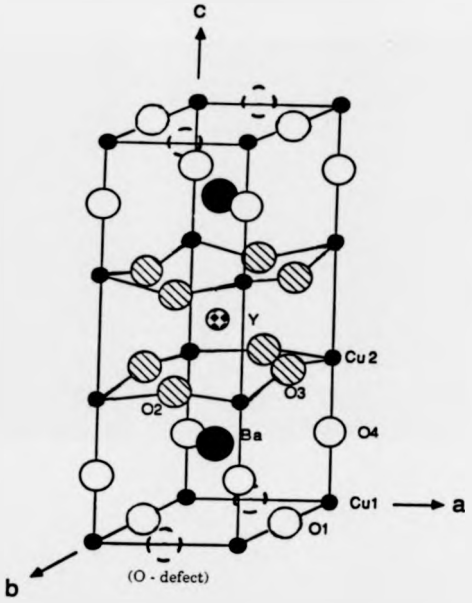

Figure 9.1 The "123" structure of $YBa_2Cu_3O_7$ showing the ordered stacking of Y and Ba along the c-axis.

heat (Jee et al 1989), has been suggested to result from a strong hybridization of the Pr 4f level and the Cu-O conduction band which may not occur for other magnetic R (Jee et al 1989, Kebede et al 1989, Li et al 1989).

The valence of the Pr ion in the 123 structure has also been suggested as a reason for the absence of superconductivity. In all other R-123 compounds the valence of the R ion is 3+, but it is known that Pr does form stable compounds as 4+ ($BaPrO_3$ for example: Tolfield et al 1972). If Pr is tetravalent in 123 then the "extra" 4f electron may eliminate holes in the Cu-O planes thus disrupting the superconducting pair formation (see for example Soderholm et al 1988). There has been some disagreement in the literature over the exact value of the Pr valence. Values close to 3+ are reported from X-ray absorption spectroscopy (Neukirch et al 1988) and structural studies (Soderholm and Goodman 1989, Neumeier et al 1990) but higher values (closer to 4+) are indicated from magnetic susceptibility (Dalichaouch et al 1988) and Hall effect measurements (Matsuda et al 1988).

The main part of the work presented in this chapter (and recently elsewhere: Boothroyd et al 1991) deals with the results of inelastic neutron scattering on the Pr/Y-123 system undertaken to measure the high energy CEF spectrum (see Chapter 5). The form of the spectrum depends on the angular momentum, **J**, of the Pr ion. This is determined by the valence of the ion. The same samples were studied using neutron diffraction and these results are also discussed. An ^{89}Y NMR study of this system and the equivalent Nd doped materials has been presented elsewhere (see Han et al 1991).

Section 9.1 Sample Preparation and Experimental Details

9.1.1 Synthesis of Materials

Although it is possible to make the 123 phase when Pr is substituted for Y in $YBa_2Cu_3O_7$ the preparation of single phase samples is not as straight forward. The melting point of pure Pr -123 was found to be in the region of 930°C rather than the higher 960°C of Y-123. For samples with only partial Pr substitution the melting point was higher (almost 950°C for less than 50% Pr). The reduced processing temperature for Pr-123 is more favourable for the formation of $BaCuO_2$ which is a common impurity in Y-123 material (especially if processed near 900°C). It was found that in nominally stoichiometric Pr-123 the main second phase was always $BaCuO_2$. Once this impurity had formed in a sample it remained very stable — repeated regrinding an re-sintering of pellets (for periods of a few days) did not remove it. Work by Jorgensen and Slaski (1987), who looked at other substitutions for Y in 123, indicated that some Pr may be replacing Ba in the 123 phase making the formation of $BaCuO_2$ more likely. This suspicion appeared to be confirmed in the study of the $Pr_{1+x}Ba_{2-x}Cu_3O_7$ system reported by Okai et al (1988). They found that the maximum amount of $BaCuO_2$ formed for $x = 0$ and that it decreased as x increased. However as x approached 0.05 another stable secondary phase, $BaPrO_3$, began to appear. The concentration of this phase increased with x. This finding was repeated in small test samples and thus a Pr excess of $x = 0.05$ was used for all the Pr-123 samples prepared for the main studies.

Three different compositions were synthesized: (a)$Pr_{1.05}Ba_{1.95}Cu_3O_7$, (b)$Pr_{0.4}Y_{0.6}Ba_2Cu_3O_7$ and (c)$YBa_2Cu_3O_7$. The starting materials were all high purity powders of Pr_6O_{11}, Y_2O_3, $BaCO_3$ and CuO. These were prepared for calcining in the usual manner (see § 7.2) in four separate 25 g batches for each composition. The processing temperatures of the three samples were all different and thus they were calcined in series in the same furnace initially at 900°C (a) and 935°C (b and c) for 19 Hrs. The subsequent procedures did not prove to be straightforward and they are thus dealt with separately for each sample:

Sample (a): X-ray diffraction after the first calcine indicated a high degree (~30%) $BaPrO_3$ formation in this sample. The four batches were ground together and re-calcined for the same time at 920°C. This was repeated once again at 920°C, also at 925°C and at 935°C, with intermediate grinding. Following this, X-ray diffraction (XRD) indicated the concentration of $BaPrO_3$ to be roughly 5% with the addition of a smaller amount of $BaCuO_2$. The ground powder was pressed into thirty (~3 g each) pellets which were sintered at 935°C for 18 Hrs.

Sample (b): The processing of the mixed Y/Pr sample also consisted of a number of stages however final resistance checks of this sample (after oxygen annealing) showed that the bulk of the 123 phase that had formed was Y-123 (Tc = 91 K rather than the expected ~40 K). A second 100 g sample was thus prepared in separate 20 g batches. The calcining (24 Hrs with two intermediate grindings) and sintering (11 Hrs) was all done at 900°C. The final quality of this sample was also poor (~10% impurity phases — mainly $BaCuO_2$ with some $BaPrO_3$) but

resistance measurements gave a broad superconducting transition near 35K. Time did not permit any further processing.

Sample (c): The nominally "pure" Y-123 sample had not reacted well after the first calcine (as indicated by XRD). It was re-ground and re-calcined for 48 Hrs but still appeared to be poorly reacted (multi-phase XRD pattern and visible signs of "green phase" — Y_2BaCuO_5). After re-grinding this stage was repeated for 24 Hrs at 950°C. Following this the powder appeared black but was soft and still showed secondary phases in XRD. The powder was pressed into ~3 g pellets which were sintered for 18 Hrs. at 960°C. The pellets, though nominally heated near to melting point, were still soft and were thus re-sintered at 980°C for 2 Hrs.

The pellets (16 mm diameter and ~3mm thick) of all three samples were cut in half (across the diameter) so as to fit into an adapted sample can (described below). They were then annealed under flowing oxygen for 12 Hrs. at 700°C and slow cooled to 40°C over 200 Hrs. The second batch of the mixed Y/Pr sample was given slightly different treatment: 2 Hrs. at 900°C, 12 Hrs. at 600°C followed by slow cooling as above. Resistance measurements indicated no high temperature (~90 K) transition in the mixed sample; only a broad one at 35 K. In resistance measurements any small regions of a higher T_c phase (ie. Y-123) in the test sample result in a decrease in resistance at 92K. As this was not seen the samples were assumed to be free of this phase. The Y- 123 sample displayed the usual single transition at 92K.

The bulk of the pellets were kept dry by removing them from the annealing furnace whilst still warm and storing them in sealed containers with silica gel.

9.1.2 Diffraction Experiment

The two Pr doped samples were studied on HRPD (see Chapter 4) but not the Y-123 sample as its structure had been determined on the same instrument previously by others (David et al 1987). About 10 g of powder from each was loaded into rectangular cans and cooled to the required temperatures in a cryostat (see § 7.2). Spectra were collected at the 1 m position, with a 12 - 112 ms TOF window, over the range 5 - 60 K (in mainly 10 K steps) for the mixed Y/Pr sample and at 5 K and 30 K for the Pr-123 sample. This was done to include the superconducting transition in the former sample and to compare the structures above and below the ordering temperature in the latter.

9.1.3 Inelastic Experiment

In a preliminary inelastic study of Pr-123 (on HET using a 20 g sample) it had been noticed that multiple phonon scattering was quite intense compared to the weak magnetic peaks — these were very broad and showed no sharp features. For the main work it was decided that the simplest solution to this problem was to increase the sample mass and to adapt the standard HET sample can (5 x 5 x 1.6 cm) by subdividing the sample space into small units using a cadmium "grid". Each unit was the size of a half-pellet with its longest dimension being the thickness of the can (the pellet diameter) — ie. 3 x 8 x 16mm. The grid was built using strips of cadmium plate 0.9mm thick.

The idea behind the grid was as follows: A neutron in the beam that is scattered by a single phonon through a large angle (~90°) would not reach the detectors. However, the further it travelled through the sample (normal to the beam) the greater the probability of a second large

angle scatter (or several small angle scatters) that would direct it into the detectors. The sample in this study needed to be large to give sufficient counts in the time available. To minimise beam attenuation by the sample, the material had to be presented to the beam as a thin slab. This also had the undesired effect of maximising the possible path length of a single phonon scattered neutron through the sample and thus increased the probability of multiple phonon scattering into the detectors. Arranging the sample half-pellets in the grid (as described above) effectively reduced the possible path length by a factor of 10. Phonon scattering simulations indicated that this would give a noticeable reduction in the multiple phonon intensity whilst still allowing for a practical sample arrangement.

The can was loaded with pellets under dry nitrogen in a glove bag and was sealed with a vanadium wire gasket. On insertion into the HET cryostat the alignment of the can with the beam was set carefully. This was done to avoid a loss of scattering intensity, especially at small angles, due to the "Venetian blind" effect of the cadmium grid.

The samples were all studied at 2 K with incident neutron energies of 180meV and 250meV. With these incident energies (E) the resolution of the 4m (low angle) and 2m detectors (see § 5.1) at energy transfers near 60meV (ie. the centre of the region of interest) is 2 - 3meV and 5 - 6meV respectively. This improves as energy transfer approaches E to roughly 1.5meV for both banks (at E=180meV). The spectra obtained were first corrected by subtraction of a time-dependent background and then converted from time-of-flight to energy transfer. Corrections for detector efficiency and the K_f/K_i phase-space term in the p.d.c.s. (see equation 5.7) were then made.

Section 9.2 Results and Discussion

9.2.1 Diffraction Experiment

X-ray diffraction shows the P123 sample to be almost single phase with some (< 5%) $BaPrO_3$ and $BaCuO_2$ present. The neutron diffraction experiment shows other (unidentified) secondary phases which make profile refinement impossible with the present software. Attempts were made to match these secondary peaks to known impurities using LAZY but with no success. Other possible phases were checked (ie. PrO_2, CuO etc.) but again this proved fruitless.

Neutron diffraction also showed that the mixed Pr/Y sample had formed some pure (or nearly pure) Y123 phase but again the lack of multiphase refinement makes the results only qualitative.

9.2.2 Inelastic Experiment

The observed inelastic scattering spectra were generally as expected based on the preliminary study mentioned in § 9.1.3. The use of the "Cd grid" in the sample can had definitely reduced the problem of multiple phonon scattering and the larger samples improved the count rate. Comparison of the two Pr samples' spectra with that of the pure Y123 blank indicated magnetic scattering in both between 40meV and 140meV. This is illustrated in figure 9.2. Here the magnetic scattering intensity has been maximised at the expense of resolution (see § 9.1.3) by summing all detectors over the angular range 3° to 29°. In figure 9.3 the P123 and Y123 samples are compared. Here the data from the high

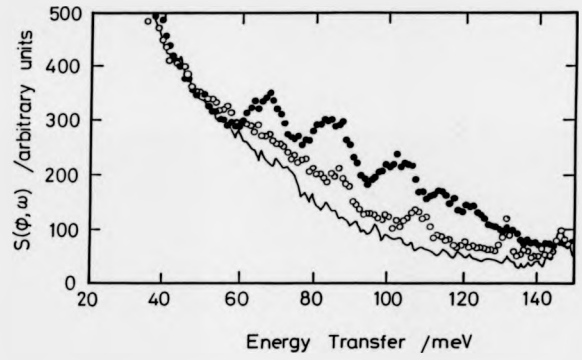

Figure 9.2 The excitation spectra of $Pr_{1.05}Ba_{1.95}Cu_3O_7$ (•), $Pr_{0.4}Y_{0.6}Ba_2Cu_3O_7$ (o) and $YBa_2Cu_3O_7$ (—) with all detectors in the angular range 3° to 29° combined.

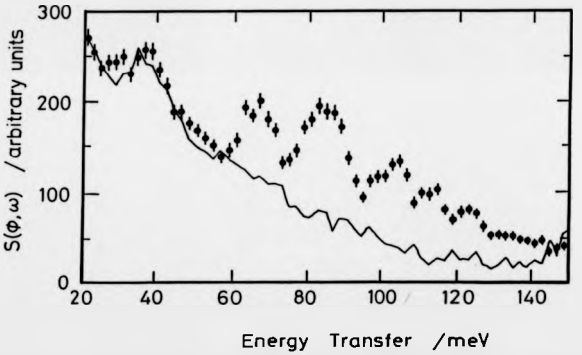

Figure 9.3 The excitation spectra of $Pr_{1.05}Ba_{1.95}Cu_3O_7$ (•) and $YBa_2Cu_3O_7$ (—) measured in the angular range 3° to 7°.

resolution (2 - 3meV) bank are shown which covers the angular range 3° to 7°. Both figures show data collected for 180meV incident neutrons and a sample temperature of 2K.

The mixed Pr/Y sample produced very broad, almost featureless, magnetic scattering with only two resolved peaks at 108meV and 132meV. The latter appears to be too sharp to be consistent with the rest of the spectrum and may therefore be due to an impurity phase. The intensity of the magnetic scattering from the mixed Pr/Y123 phase would have been reduced by the fraction of Y123 present in the sample (see §9.2.1) but this would not affect the peak positions or widths.

The pure Pr123 spectrum has several broad peaks at energy transfers of roughly 65, 85, 105, 113, 123 and 132meV. The last of these is identified mainly on the basis of the additional intensity found between 130 - 140meV in this spectrum as compared to the same region in the Y123 spectrum although in both cases the region seems featureless. It can be seen that a small rescaling of the Y spectrum could eliminate this anomaly (within the uncertainty of the data) without causing too great a problem at lower energy transfer.

The Y123 spectra were rescaled for the comparison with the Pr123 spectra by matching the intensity of the lower energy (non-magnetic) scattering up to 40meV.

9.2.3 CEF analysis of the inelastic data

The single broad magnetic peak seen in the mixed Y/Pr sample makes any quantitative CEF analysis very difficult because many more CEF parameters would be required (as explained below) than could be

obtained from it. It was decided to concentrate on the Pr123 spectrum as this offered a range of resolved peaks.

The uncertainty over the valence of the Pr ion mentioned in the introduction to this chapter (3+ or 4+) can be addressed in simple terms by considering the expected CEF spectra for each valence. The Hund's Rule ground state (g.s.) of Pr^{4+} has $J=5/2$. CEF theory (given in detail by Walter 1984) determines that the spectrum should therefore consist of three doublets. The Pr^{3+} g.s. (J=4) would comprise nine singlets. Previous measurements at small energy transfer (Walter et al 1988) indicated the presence of two energy levels below 10meV and this has recently been confirmed by Jostarndt et al (1991). Adding these two levels to those observed in this study effectively rules out 4+ for the valence of Pr in Pr123.

The CEF spectra of other R^{3+} in R123 have been studied by many groups (see for example Furrer et al 1988, Nekvasil et al 1988, Soderholm et al 1991 and Boothroyd et al 1992a). It can be assumed that the local structural environment of all the R123 compounds is roughly constant throughout the series. Hence it should be possible to predict the CEF levels of Pr^{3+} from the known levels of other R^{3+}. The low symmetry (D_{2h}) of the R site means that the CEF Hamiltonian requires nine CEF parameters (see §5.3.2). It has only been possible to determine these unambiguously for Ho^{3+} (Furrer et al 1988). Scaling the Ho^{3+} parameters to Pr^{3+}, taking account of the different atomic sizes, predicts a Γ_1 g.s. (Γ_i, where i is an integer, is the symmetry assignment derived from the coefficients of the subset of states from within the $^3H_4$ g.s. multiplet — see Furrer et al 1988) with two excited levels below 10meV and six levels at high energy — of which only three have measurable transition probability (see Soderholm et al 1991). A similar

scheme with a smaller overall splitting has been obtained by transferring the CEF parameters for the R containing garnets (see Nekvasil 1988 and Nekvasil et al 1988). Even if the 132meV "peak" is not considered (as suggested in §9.2.2) this still leaves two peaks too many to account for at high energy.

Initial rough fits of the data (by the traditional method of Stevens' operators — Stevens (1952) — and considering only the g.s. intramultiplet transitions) produced only three or four high energy transitions with measurable intensity. It was concluded that the additional observed peaks may be in part due to the presence of some Pr^{4+} ions. Careful analysis has now ruled this out (see later). They may also be the result of a variation in oxygen stoichiometry in the sample (causing singlet levels to appear as multiple peaks — as observed in oxygen deficient Er123 and Ho123 by Allenspach et al 1989) or, because some Pr is doped onto the Ba site, there may be some scattering of sufficient intensity at different energies.

The final fits of the CEF parameters to the Pr123 data followed a method essentially the same as that of Goodman et al (1991). In this approach, the full Hamiltonian for a R ion (in a crystalline environment) is diagonalized in the intermediate coupling scheme, including interactions between states in other J multiplets. This has been extended by Boothroyd et al (1992a), in similar work on Pr_2CuO_4 and Nd_2CuO_4, to include an extra interaction corresponding to the molecular field associated with the exchange interactions between the ions as described in §5.3.

9.2.4 Results of CEF fits and discussion

The starting values of the CEF parameters were taken by scaling those obtained by Boothroyd et al (1992b) for Ho^{3+} to Pr^{3+} (as explained below). In their work, Boothroyd et al have considered all the best available INS data for Ho123 and have fitted both the observed intensities and the transition energies with great confidence. This has lead to a slight difference in the parameter set and level assignments reported earlier by Goodman et al (1991).

The Ho^{3+} CEF parameters were scaled to Pr^{3+} (in accordance with equation 5.11) assuming that the intrinsic CEF parameters remain constant across the R123 series and by using the appropriate radial moments (see Freeman and Watson 1962, Freeman and Desclaux 1979). A constant "rescaling" factor of 0.62 was applied to the scaled Pr^{3+} parameters (in the manner of Goodman et al 1991) so that the range of the calculated g.s. splitting was in rough agreement with the experimental splitting. The rescaling is required to allow for the unequal effective contractions of the 4f wavefunctions in R ions (Boothroyd et al 1992b) and the procedure is now reasonably well proven (see for example Goodman et al 1991 and Soderholm et al 1992). The molecular field parameter, h_{MF}, was determined from the saturated magnetic moment on the Pr ion of $0.74\pm0.08\ \mu_B$ (from neutron diffraction measurements by Li et al 1989).

The results of the fits to the Pr123 data are given in Table 9.1. Also given are the results of earlier works and the starting parameters scaled from Ho^{3+}. The uncertainties of the CEF parameters calculated from the variance given by the fitting software are not independent and cannot be taken as a true measure of the uncertainty in all cases (as explained by

Table 9.1 Crystal Field parameters (B_q^k in meV) for Pr^{3+} as determined in this study and previously.

CEF parameter	This Study	Ref (a) Ho^{3+} scaled	Ref (b)	Ref (c)
B_0^2	38 ± 1	69	- 29	56
B_0^4	- 368 ± 2	- 384	- 420	- 344
B_0^6	142 ±5	129	88	98
B_2^2	16 ± 5	- 7	7	20
B_2^4	- 61 ± 10	- 18	20	2
B_2^6	41 ± 18	- 15	---	- 42
B_4^4	162 ± 5	190	127	185
B_4^6	290 ± 5	343	198	342
B_6^6	39 ± 9	6	---	13
h_{MF}	0.29 ± 0.03			0.47

Ref (a): Boothroyd et al 1992

Ref (b): Nekvasil et al 1991

Ref (c): Goodman et al 1991

Boothroyd et al 1992). The uncertainties quoted in Table 9.1 are generally greater than the calculated values (except for B_0^2 and B_0^4) by a factor of ~5. These were estimated by comparing fits made to the same transition energies but with slightly different peak intensity ratios for the high energy data. The ratios and energies used in the final fit are given in Table 9.2 along with the corresponding values calculated from the B's in Table 9.1. The transition probabilities from each of the lowest three levels are included to allow for comparison with spectra collected at higher temperatures (for example: Gering et al 1988, Goodman et al 1991 and Jostarndt et al 1991). The transitions from i=0 are most relevant to the present study where the data were collected at 2K. The symmetry assignment of each level (Γ_i) is also listed and it should be noted that order of the three lowest levels Γ_4 (g.s.), Γ_2 and Γ_1 differs from that reported by Goodman et al (1991): Γ_1 (g.s.), Γ_4 and Γ_2. The order given in this study is seen to be the better of the two when the magnetic susceptibility is considered. This has been calculated both perpendicular ($\chi_\perp$) and parallel ($\chi_{//}$) to the Cu-O planes as a function of temperature (see figure 9.4). The important result is that $\chi_\perp$ is seen to be greater than $\chi_{//}$ at all temperatures. This agrees with the anisotropy in the susceptibility (in an aligned powder sample) measured at low temperatures by Kebede et al (1989). Goodman et al predict $\chi_\perp < \chi_{//}$ below 100K — opposite to the observed behaviour. This result also explains why the Pr moments in the antiferromagnetic state order along the c-axis (see Li et al 1989): it is the easy direction. The isotropically averaged susceptibility (χ) has also been calculated and is plotted against inverse temperature in the range 0 - 300 K in figure 9.5. A Curie law fit:

$$\chi = \chi_0 + \frac{C}{T} \qquad 9.1$$

Table 9.2 Observed and calculated CEF transitions within the ground state multiplet of Pr123. Transitions grouped together were unresolved.

level j	Γ_j	E_{obs} (meV)	E_{calc} (meV)	I_{obs} *	I_{calc} *	Calculated transition probabilities, $\|\langle j\|\hat{\mu}_\perp\|i\rangle\|^2$ for: i=0	i=1	i=2
0	Γ_4	0.0	0.0		18	0.40	2.72	2.24
1	Γ_2	3.5±0.5	3.6	130±30	121	2.72	0.40	2.18
2	Γ_1	5.0±0.5	5.0	100	100	2.24	2.18	0.00
3	Γ_1	61±2	60.3			0.23	0.54	0.15
4	Γ_3	62±1	62.2	80±20	79	0.24	0.71	0.42
5	Γ_2	67±1	66.9			0.33	0.01	1.31
6	Γ_4		83.1	100	100	0.00	0.16	0.34
7	Γ_3	83±1	83.2			1.01	0.32	0.95
8	Γ_1	103±2	103.4	50±20	51	0.52	0.78	0.00

* Intensity relative to level 1 for levels 0-2 and relative to level 6/7 for levels 3-8.

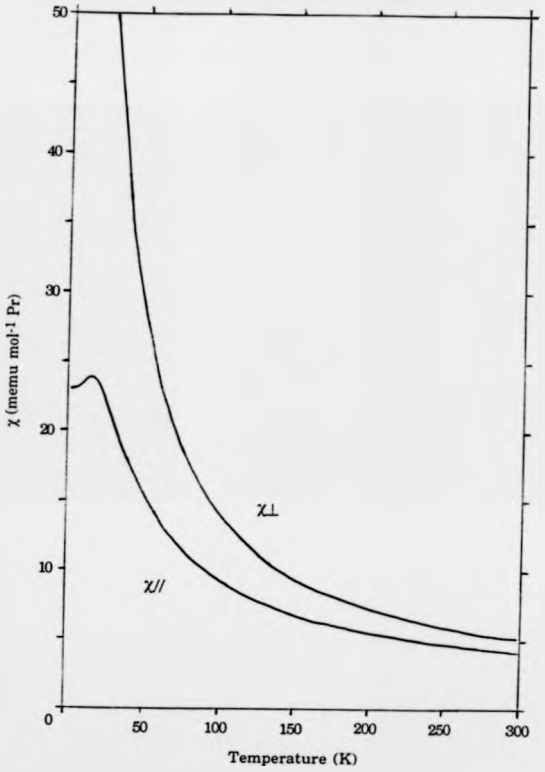

Figure 9.4 The calculated magnetic susceptibility perpendicular ($\chi_{\perp}$) and parallel ($\chi_{//}$) to the Cu-O planes of $Pr_{1.05}Ba_{1.95}Cu_3O_7$ as a function of temperature.

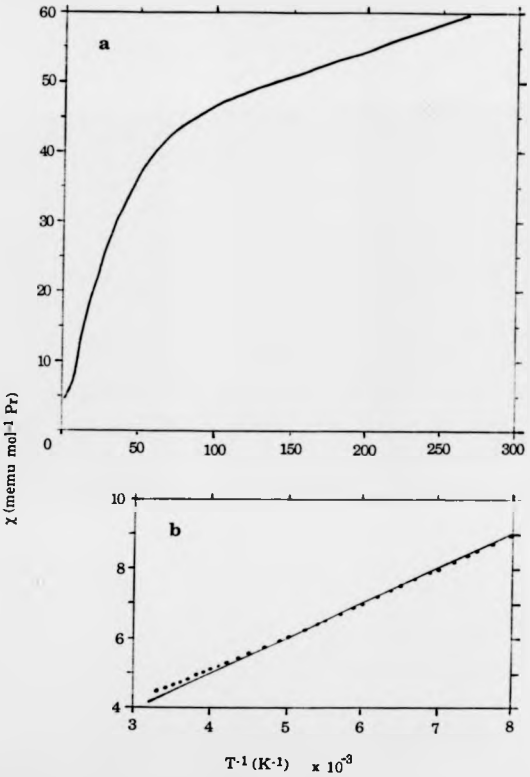

Figure 9.5 The calculated isotropic average magnetic susceptibility (χ) of $Pr_{1.05}Ba_{1.95}Cu_3O_7$ as a function of inverse temperature.

b : The solid line is the fit to the calculated data (points).

has been made to the data in range 100 - 300 K. The term χ_o is the temperature (T) independent contribution to χ and the Curie constant, C, is related to the effective magnetic moment, μ_{eff}, of the Pr ion (in units of Bohr magnetons) by:

$$\mu_{eff} = \sqrt{\frac{3\, k_B\, C}{N_A\, \mu_B^2}} \qquad 9.2$$

where k_B is the Boltzmann constant, N_A is the Avagadro constant and μ_B is the Bohr magneton. This predicts $\mu_{eff} = 2.85 \pm 0.01\mu_B$ which is close to the value ($2.87\mu_B$) obtained by Peng et al (1989) in a careful study of the Pr/Y123 system and is similar to values predicted Soderholm et al (1991). The latter group also give a detailed account of the problems involved in trying to compare the predicted values of χ_o (1.21 memu/mol in their study and 1.1 ± 0.1 memu/mol here) with their experimentally determined value of 2.18 memu/mol. They are forced to add a correction due to the contribution of the rest of the lattice of 0.97 memu/mol. They state that an independent estimate of this correction could be obtained from Y123, but as yet the variations of χ_o for Y123 with oxygen stoichiometry and lattice constants (which change with R doping) are not yet fully understood.

The electronic specific heat of Pr123 has been calculated, from the fitted CEF parameters, and shows a peak at ~17K (see figure 9.6) which is consistent with measurements made by others (see below). The contribution to the specific heat from the rest of the lattice can be assumed to follow the Debye specific heat (c_v) function which, at low temperatures, takes the form $c_v = 1944(T/\theta_D)^3$ $Jmol^{-1}$ K^{-1} (after Ashcroft and Mermin 1988). The Debye temperature for Pr123 has been estimated by Goodman et al (1991) as θ_D = 330 K. The lattice contribution and the

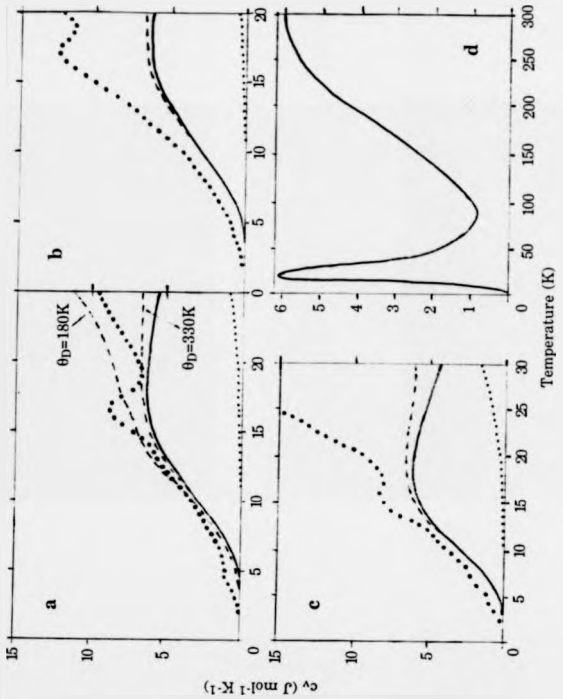

Figure 9.6 The calculated specific heat (c_v) of $Pr_{1.05}Ba_{1.95}Cu_3O_7$ as a function of temperature: (a) - (c) in the range 0 - 30K and (d) 0 - 300K. Observed data in (a) - (c) (see references in text) is given as *. The calculated electronic c_v is given by —, the lattice contribution (for θ_D=330K) by -- and the total c_v by ---. Only the electronic c_v is given in (d) and the total c_v with θ_D=180K is also given in (a).

total specific heat are also shown in figure 9.6 with overplots of observed data (up to 30 K) taken from (a) Jee et al (1988a), (b) Li et al (1989), and (c) Maple et al (1989). All the published data show the 17K peak but there are differences in the measured magnitude of c_v (the peak height varies from ~8 to ~13 $Jmol^{-1} K^{-1}$). The calculated total c_v is dominated by the electronic term at these temperatures and hence the reasonably good agreement between the calculated and observed data up to ~12K is another indication that the fit to the CEF parameters is sound. The match could be improved for each set of data (a) - (c) by choosing different values for θ_D (one example is given in (a) for θ_D=180K) but this does not seem worthwhile until the reasons for the differences between the present data can be explained — it is likely that sample quality may play some part. The electronic contribution to c_v is also plotted over the range 0 - 300K (see figure 9.6d) but this prediction is not expected to hold at the higher temperatures as it would indicate a total c_v greater than the Dulong-Petit value (24.9 $Jmol^{-1} K^{-1}$) above 200K. No data is available at present for c_v with T>30K.

The fit to the observed spectrum for Pr123 is very good with regard to both the energies and relative intensities of the transitions. Boothroyd et al (1992b) have also measured the transitions from the g.s. to the first excited multiplet (E_i=550 meV at 5K). A single weak magnetic peak at 282±5 meV was seen in the range 150 - 500 meV. Table 9.3 lists the energies and transition probabilities for these transitions ($^3H_4$ to $^3H_5$ of Pr^{3+}) as predicted by the fit (Table 9.1) to the intra-multiplet ($^3H_4$) transitions. It can be seen that the only possible peaks would be from the three transitions between 275 - 300 meV — in agreement with the high energy experiment.

Table 9.3 Observed* and calculated CEF transitions from the $^3H_4$ to $^3H_5$ multiplets for Pr(3+)123. Transitions grouped together were unresolved.

level j	E_{obs} (meV)	E_{calc} (meV)	Calculated transition probabilities, $\|\langle j\|\mu_\perp\|i\rangle\|^2$
10		277	0.55
11		285	0.01
12	282 ± 4	286	0.58
13	*	298	0.05
14		301	0.30
15		323	0.04
16		328	0.00
17		331	0.03
18		339	0.00
19		347	0.02
20		348	0.02

* By Boothroyd et al (1992).

The two peaks observed at highest energy transfer (see figure 9.2) were not included in the fit — attempts to do so did not produce satisfactory results. The possibility that these may indicate scattering from Pr^{4+} was investigated by scaling the fitted CEF parameters (Table 9.1) to Pr^{4+} but with $h_{MF} = 0$. With no molecular field, all the levels are degenerate Kramer's doublets (see Table 9.4) with the lowest six levels belonging to the $^2F_{5/2}$ g.s. and the next eight to the $^2F_{7/2}$ multiplet. The predicted level at 77 meV would partially overlap the Pr^{3+} 83 meV level (given the width of the observed peaks) but the stronger transition at 37 meV is well clear of the Pr^{3+} scattering and would certainly indicate the presence of Pr4+ in the sample.

In this study, no magnetic scattering has been observed in this region of the spectrum (figure 9.2) within the limits of error. The peak near 35 meV is also seen in the Y123 magnetic blank which, when the Q dependence is considered too, indicates that it is of phonon origin. This suggestion is supported by Soderholm et al (1991) who have considered similar spectra. The higher energy Pr^{4+} transition is predicted to overlap those from Pr^{3+} near 280 meV and cannot help to discriminate between the two possible valences. It should be noted that the 37 meV peak should have the greatest intensity of the three discussed (see Table 9.4) so its "absence" rules out any significant contribution to the observed spectrum (figure 9.2) from Pr^{4+} scattering. Considering the transition probability for the 37 meV level and the uncertainty in the observed data places an upper limit of roughly 5% on the concentration of Pr^{4+} ions on the R site in the Pr123.

Table 9.4 CEF transitions calculated for Pr^{4+}. The energies are calculated from the scaled parameters for Pr^{3+} given in Table 1 with h_{MF} set to zero.

level i	E_{calc} (meV)	Calculated transition probabilities, $\|\langle j\|\hat{\mu}_\perp\|i\rangle\|^2$
0,1	0	1.56
2,3	37	1.16
4,5	77	0.76
6,7	278	0.73
8,9	309	0.01
10,11	323	0.01
12,13	521	0.68

Conclusions

The CEF parameters obtained in this fit are similar to those of Goodman et al (1991) but with a change in the symmetry order of the three lowest levels resulting from different assumptions about the energies and relative intensities of the observed transitions. This reassignment has been justified by the correct modelling of the anisotropy of the components of the magnetic susceptibility below 100K. There is also a satisfactory agreement with the calculated and observed specific heat — data published to date extends only up to 30K and there is a need for observations to be made at higher temperatures. It has been demonstrated that the CEF spectrum of Pr123 can be adequately described by a Pr^{3+} valence when J-mixing in a weak molecular field is considered.

One characteristic of the magnetic scattering from Pr123 that distinguishes it from that of other magnetic R123 compounds (see for example Furrer et al 1988 and Soderholm et al 1991) is the large intrinsic widths of the peaks. The CEF at the R site is dominated by the O ions in the Cu-O planes and hence any local chemical disorder could produce broadening. No evidence of this has been reported so a different mechanism must be sought. It is suggested that there is a weak hybridisation of the Pr 4f electrons with states on the planes. The delocalised 4f electrons could be partially responsible for the suppression of superconductivity by hole-filling (see the introduction to this chapter) and the peak widths would result from the lifetime of the Pr^{3+} ($4f^2$) ion. This dynamic mixed-valence state must be very close to 3+ considering the results of this study and hence could not be fully responsible for the

disruption of the superconducting state as suggested for 4+ (a recent detailed review of the magnetic ordering of Pr123 by Jostarndt et al 1991 puts an upper limit on the Pr ion valence of 3.1+). A second effect of the hybridisation may be a strengthening of the exchange interaction through the Cu-O planes. This could account for the relatively high Neel temperature (for a R123 compound) of the Pr ordering which in turn may result in pair breaking or hole localisation leading to the full suppression of superconductivity.

The presence of magnetic peaks between 110 - 140 meV cannot be explained as resulting from either 3+ or 4+ Pr on the Y site. It is known that Pr (and other R) do populate the Ba site (see Soderholm and Goodman 1989) and this fact was assumed in the preparation of the sample used in this study. Roughly 10% of the Ba sites have been shown to be affected even in nominally stoichiometric samples of Pr123 (Nutley et al 1992 — by polarised neutron diffraction in a single crystal). The percentage may thus be higher in this, over-stoichiometric, sample. It is suggested that the additional peaks may result from magnetic scattering from the Pr at these sites which may be 3+ or 4+ valence.

CHAPTER 10

Zn AND Ga DOPING IN $YBa_2Cu_3O_{7-\delta}$

Introduction

The $YBa_2Cu_3O_7$ structure (see figure 10.1 — after David et al 1987) contains two distinct low dimensional features. There are Cu-O planes (also seen in other high T_c materials) and Cu-O chains. The respective roles of these features in sustaining the high T_c's (~90 K) of this and other R-123 compounds was of early interest. A widely used technique was to replace Cu, in varying amounts, with other ions (ie. Fe, Co, Ni, Cr, Zn, Ga and Al) and note the effect on T_c (see for example Narasimha Rao et al 1988 and references therein). It soon became clear that substitution by non-magnetic Zn caused a rapid decrease in T_c (Maeno et al 1987, Jee et al 1988b, Kajitani et al 1988, Tarascon et al 1988, Xiao et al 1988a,b) which was more severe than for magnetic ions such as Fe or Co (Oda et al 1987, Sankawa et al 1988). Other non-magnetic ions such as Ga had only a slight detrimental effect on T_c despite inducing small structural changes (Hiratani et al 1987, Maeno et al 1987, Xiao et al 1988a).

A number of explanations have been put forward to account for the effects of Zn doping:

(a) Xiao et al (1988a) suggest that Zn doping of the Cu-O planes decreases the number of 3d holes and reduces the density of states (DOS) at the Fermi level. This would give a corresponding decrease in T_c.

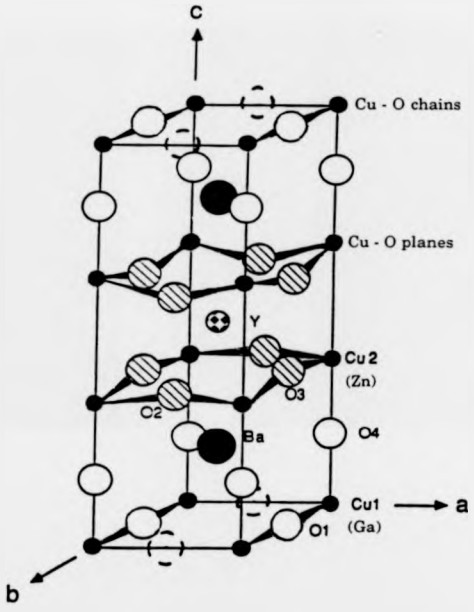

Figure 10.1 The "123" structure of $YBa_2(Cu_{1-x},M_x)_3O_7$ showing the Cu-O planes / chains and the substitution sites of M = Zn and Ga.

(b) Tarascon et al (1987) propose that d holes in the planes can become localised by the incorporation of Zn atoms. This induces magnetic moments on the Cu sites which destroy the superconducting state.

(c) Assuming the pairing interaction that allows for the formation of the superconducting state involves magnetic fluctuations (Emery 1987 and also see §1.2.3) then the range of these fluctuations will be limited by the presence of non-magnetic impurities. This may prevent the formation of the ordered state required for superconductivity.

The contrasting behaviour of Zn and Ga dopants led to the work presented in this chapter (previously published elsewhere — Balakrishnan et al 1989). They make excellent probes as they both have filled 3d shells but Zn (2^+) appears to substitute preferentially for the Cu ions in the planes whilst Ga (3^+) favours the chains (Xiao et al 1988a,b, Maeda et al 1989). The effect of these dopants was studied using high resolution NMR concerned with the shift and relaxation time of the ^{89}Y resonance.

Section 10.1 Sample Preparation

Initially samples (Batch 1) were prepared separately for Zn and Ga doping to find the range of most interest. The usual solid state route (see § 7.2) was followed to make three samples each with x=0.07, 0.14, 0.21 and x=0.033, 0.066, 0.099 respectively. The Zn x=0.07 and all the Ga samples were superconducting (see figure 10.2). For the main study

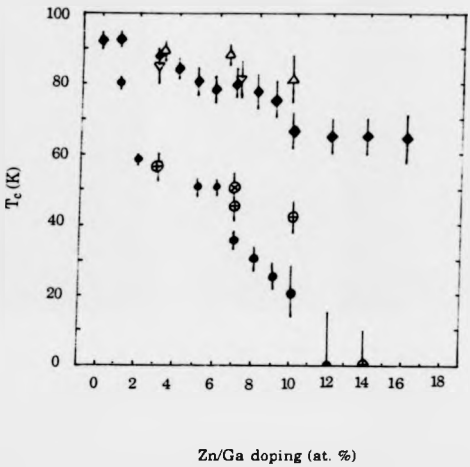

Figure 10.2 T_c as a function of doping in $YBa_2(Cu_{1-x},M_x)_3O_7$ (M=Zn,Ga).
Ga: • (Xiao et al), Δ (Batch 1) and ∇ (Batch 2).
Zn: • (Xiao et al), ⊗ (Batch 1) and ⊕ (Batch 2).

seven samples (Batch 2) were prepared in parallel from high purity powders of Y_2O_3, $BaCO_3$, CuO, ZnO and Ga_2O_3. One sample was undoped Y-123 prepared under the same conditions as a control. Four Zn doped samples, $YBa_2(Cu_{1-x}Zn_x)_3O_7$, with x = 0.03, 0.07, 0.10, 0.14 and two Ga doped samples, $YBa_2(Cu_{1-x}Ga_x)_3O_7$, with x = 0 03, 0.07 were made. Later an additional Ga sample with x = 0.015 was prepared by the same route so as to obtain more data for this system.

All the samples were calcined at 900°C for 15 Hrs., re-ground, pelletized, sintered at 910°C for 15 Hrs. and then checked for phase purity using XRD. This revealed incomplete reaction in the Y-123 and Ga doped samples. All the pellets were thus re-ground, re-pelletized and re-sintered at 900°C for 15 Hrs. XRD indicated sufficient phase purity at this stage so all the pellets were annealed under flowing oxygen at 900°C for 24 Hrs. and slow cooled to room temperature over 240 Hrs.

The samples were then characterized by XRD and resistance measurements. The former indicated a high phase purity (slightly less for the highest doping of Zn and Ga). The latter gave Tc's consistent with values in the literature (see for example Xiao et al 1988) and are summarised in figure 10.2 (the Batch 1 results are also included).

Section 10.2 The NMR Experiment

The NMR measurements were made at room temperature using a Bruker MSL 360 spectrometer operating at 17.646 MHz for the ^{89}Y nucleus. The reference sample was a one molar aqueous solution of YCl_3 and all shifts were measured relative to this resonance. The Magic

Angle Spinning (MAS) technique (see §6.3) was employed to narrow the ^{89}Y resonance line. Static NMR would have made the detection of the very small shifts (total range of 20ppm) difficult to detect.

The spin-lattice relaxation time, T_1, was measured using a saturating comb (see §6.2 for more details) of ten 90° pulses separated by 2ms followed by a sampling pulse.

All of the above measurements were carried out at the University of Warwick (Dept. of Physics) by M. E. Smith.

Section 10.3 Results

Figures 10.3 and 10.4 show the effect of Zn and Ga substitution on the ^{89}Y spectrum at room temperature. The broad line for high Zn doping (14%) indicates the inhomogeneous nature of this sample — as expected from XRD.

The ^{89}Y shift increases with concentration (x) for both Zn and Ga substitution but the rate is greatest for Ga. In figure 10.5 the shifts are plotted for both elements as a function of x. The smallest doping of Ga (x=1.5%) increases the ^{89}Y shift (ie. less negative) by 18ppm and greater doping changes it at a rate of 2.8 ± 0.6 ppm/%Ga. Zn substitution results in only a slight increase in shift at a rate of 0.8 ± 0.2 ppm/%Zn.

The data obtained in the T_1^{-1} measurements are well represented for each sample by a single exponential. There is a sharp contrast between the two substitutions in the effect on T_1^{-1}. The relaxation rate decreases with dopant concentration for Ga substitution but increases

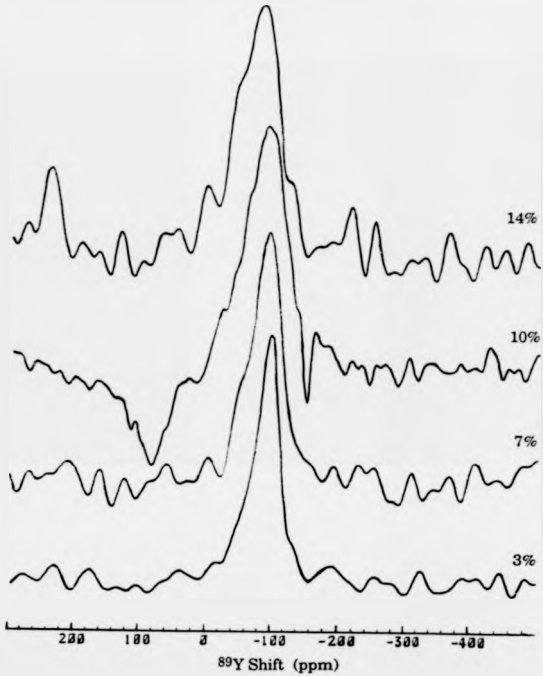

Figure 10.3 The ^{89}Y NMR spectra for $YBa_2(Cu_{1-x},Zn_x)_3O_7$ (x=0.03 to 0.14).

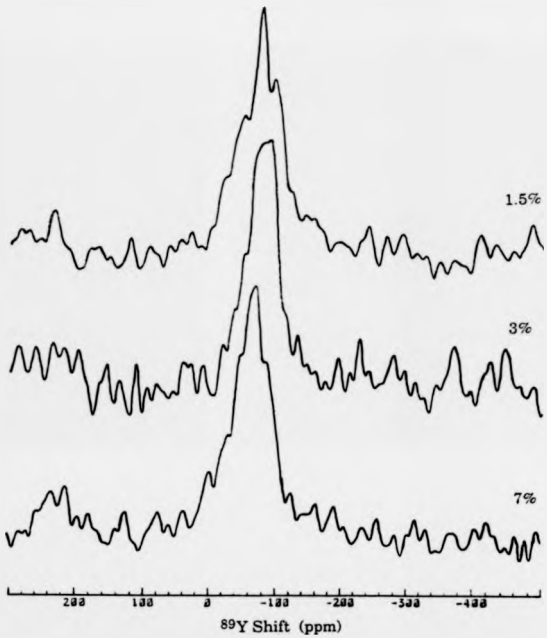

Figure 10.4 The ^{89}Y NMR spectra for $YBa_2(Cu_{1-x},Ga_x)_3O_7$ (x=0.015 to 0.7).

for Zn (see figure 10.6). Whereas Ga doping has the greater effect on shift, Zn doping has the greater effect on T_1^{-1}.

Section 10.4 Discussion and Conclusions

Linear extrapolation of the Ga induced shift to 0% doping gives a shift value of -90 ± 2 ppm. This indicates that the orthorhombic to tetragonal transition in these samples results in a change of shift of roughly +13 ppm (see figure 10.5). This is small compared to the estimated chemical shift of +200 ppm (from work using the same spectrometer by Balakrishnan et al 1988). A small change in the chemical shift is expected to result from the slight change in the local environment of the Y site. The additional, doping dependent, change in the the shift is interpreted as a reduction in the Knight shift (see §6.3) — previously estimated at roughly -303 ppm (Balakrishnan et al 1988). This indicates that the DOS at the Fermi level is reduced by Ga substitution (see equations 6.5a,b) and is consistent with the gradual decrease in T_c. Assuming that these materials, in the normal state ($T>T_c$), behave as simple metals then the Korringa relation (§6.3), K^2T_1T = constant, should hold. Table 10.1 gives the value of K^2T_1T for each value of Ga x. The change in T_1 with x is small compared to the uncertainty in the measurements hence the value of 11s quoted for each x in the table. This uncertainty dominates the error estimates for the K^2T_1T values which indicate a Korringa behaviour for Ga substitution.

Zn doped Y123 remains orthorhombic over the range of samples studied and the change in ^{89}Y shift extrapolates linearly to the value for

Table 10.1 The Korringa - like behaviour of $YBa_2(Cu_{1-x},Ga_x)_3O_7$ at room temperature.

x (%)	Shift (ppm) ± 5 ppm	K (ppm)* ± 10 ppm	T_1 (s)	$K^2 T_1 T$ (ppm^2 s K) x 10^8
0	- 103	- 303	11 ± 1	3.0 ± 0.3
1.5	- 85	- 298	11 ± 2	2.9 ± 0.6
3.0	- 82	- 295	11 ± 2	2.9 ± 0.6
7.0	- 68	- 281	11 ± 3	2.6 ± 0.7

* Note that the chemical shift changes by 13 ppm between x=0% and x=1.5%.

Table 10.2 The non -Korringa - like behaviour of $YBa_2(Cu_{1-x},Zn_x)_3O_7$ at room temperature.

x (%)	Shift (ppm) ± 5 ppm	K (ppm)* ± 10 ppm	T_1 (s)	$K^2 T_1 T$ (ppm^2 s K) x 10^8
0	- 103	- 303	11 ± 1	3.0 ± 0.3
3.0	- 101	- 301	9 ± 1	2.4 ± 0.2
7.0	- 98	- 298	6.0 ± 0.4	1.5 ± 0.1
10.0	- 94	- 294	5.3 ± 0.3	1.3 ± 0.1

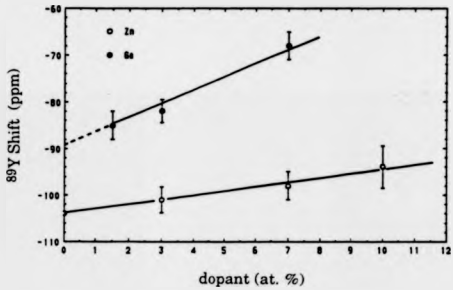

Figure 10.5 The isotropic ^{89}Y shift for $YBa_2(Cu_{1-x},M_x)_3O_7$ (M=Zn,Ga) as a function of dopant.

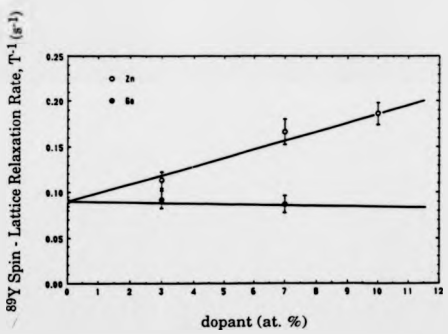

Figure 10.6 The ^{89}Y spin-lattice relaxation rate (T_1^{-1}) for $YBa_2(Cu_{1-x},M_x)_3O_7$ (M=Zn,Ga) as a function of dopant.

undoped Y123 (T_c=92K). Assuming that there is a negligible change in the chemical shift all the observed changes of shift must therefore be changes of Knight shift. The Knight shift is reduced by increasing Zn doping but only by a small amount (ie. 3% at x=0.1), thus there must only be a small decrease in the DOS at the Fermi level for these compounds even at high doping levels. Loram et al (1990) have subsequently concluded from their electronic specific heat measurements that there is no detectable change in the DOS (for $T>T_c$) up to 7% Zn doping in these materials. The observed rapid decrease in T_c with x cannot therefore be attributed to a decrease in the DOS — this rules out explanation (a) in the Introduction.

The Korringa relation is not seen to hold for Zn substitution — see Table 10.2. The uncertainty in T_1 again dominates the estimate of the error in the K^2T_1T values but the change in T_1 is more significant compared to the uncertainty and it is clear that K^2T_1T is not constant for Zn substitution. This can also be determined by inspection of figures 10.5 and 10.6 because, for the Korringa relation to hold, T_1 must increase as K decreases — this is not the case.

The linear increase in relaxation rate is unusual for a conducting system as the relaxation is normally dominated by the DOS and hence a decrease (as for Ga doping) would be expected. Such behaviour would normally be associated with localised fluctuating magnetic fields (ie. as produced by magnetic impurities) which allow the nuclear moments to give up energy more rapidly. It is difficult to think of other possible relaxation mechanisms that would not produce a shift and would also increase T_1^{-1} so rapidly with Zn concentration. The magnetic susceptibility of these compounds has been measured (Jee et al 1988b) and has shown that the effective magnetic moment increases with Zn

doping. This supports the idea ((b) above) that magnetic moments are induced on the Cu2 sites by the substitution of Zn on the Cu-O planes.

The life-time of any magnetic moments on either of the Cu sites must be short or they would have been detected in NMR (ie. Warren et al 1987 and Walstedt et al 1991) and μSR (Brewer et al 1988) measurements. This also restricts the time-scale for the temporal and spatial correlations between copper moments. These antiferromagnetic fluctuations form the basis of certain magnetic models of superconductivity discussed in §1.2.3. The doping of non-magnetic Zn into the plane sites may increase the life-time of the Cu moments by reducing the hopping of holes between sites and/or restricting the spatial correlation between moments. The moments may result in magnetic pair breaking or the correlation length of the fluctuations may be reduced to the extent that it cannot support pairing. Only the time averaged magnetic field would be observed by NMR and hence the change in shift on doping with Zn would be small — in agreement with the results presented here. This supports both ideas (b) and (c) mentioned above.

The change in T_1^{-1} due to these local fluctuating magnetic fields (B_{loc}) will be (after equation 6.4):

$$T_1^{-1} \propto (B_{loc})^2 \tau \qquad 10.1$$

where τ is the correlation time of B_{loc} at the Y site. The strength of the exchange interaction in Y123 has been estimated at 0.1 eV (Lyons et al 1988). This gives a value τ for this interaction of $\sim 10^{-15}$ s. If B_{loc} is taken to be the dipolar field from a moment of $0.6\mu_B$ at the Cu2 site in Zn doped Y123 then $\tau \sim 10^{-13}$ s — much longer than for pure Y123. However if the

pure Y123 value of t is assumed to hold for the case of Zn doping then B_{loc} would be an order of magnitude greater than the dipolar field.

This possibly could arise from a transferred hyperfine interaction from the Cu2 sites. Such an interaction has been suggested as contributing to the T_1's of the Cu1 and Cu2 nuclei in Y123 (Pennington et al 1989). It has also been used to interpret theoretically the ^{89}Y shift in Y123 in terms of the isotropic coupling field (D) between Y nuclei and the eight nearest neighbour Cu2 sites (see for example Mila and Rice 1989a,b, Imai 1990 and Millis et al 1990). The formulation used by the latter group is commonly referred to in the literature as the MMP model.

The precise nature of the mechanism that gives such a large increase in the relaxation rate (and rapid decrease in T_c) in Zn doped Y123 is not clear from the results presented here, however in general terms the only reasonable explanation is that localised fluctuating magnetic fields are induced in the Cu-O planes by the doping. It can also be concluded that the doping of Ga occurs preferentially on the Cu-O chains and reduces T_c by a different mechanism to Zn doping — a reduction in the DOS at the Fermi level. This work has been extended by A. Gencten with studies of other dopants on each site (chains: Ga, Fe, Co, Al ; planes: Ni. Zn ; mixed: V) which include the temperature dependence of the shifts/ relaxation times/ line widths of ^{51}V and ^{27}Al in addition to ^{89}Y (see Gencten 1992 and Dupree et al 1992). This has also included an attempt to interpret the results using the MMP model mentioned above. In brief the chain site dopants behave in the same manner as reported for Ga in this chapter — even to the extent of giving the same change in chemical shift (~ 13ppm) — and substituting Ni on the planes has a similar effect to Zn.

CONCLUSIONS

This study has highlighted, by various means, the similarities and differences between a small selection of the presently known High-T_c Superconductors. The investigations were undertaken to help to clarify which features of each of the systems were important/unrelated to the superconducting mechanism and to look for any common themes. A degree of success has been achieved in these aims.

The central issues considered have been:

1. How are structure and structural transitions related to superconductivity and how do they depend on the level of doping ?

2. Why is Pr the only magnetic R that, when substituted for Y in Y123, disrupts the superconducting state — is it because it adopts 4+ valence ?

3. Why do different dopant on the Cu sites in Y123 have such different effects on T_c and why do they have an effect at all ?

In this thesis two high resolution neutron diffraction studies were reported on La-Ba-Cu-O (LBCO) and Nd-Ce-Cu-O (NCCO) which address the first question. It was shown that LBCO undergoes a series of structural phase transitions as a function of temperature for a discrete range of Ba doping. This coincides with the appearance of superconductivity. The fact that these transitions are not seen in other superconductors, but are seen in similar non-superconductors, indicates that both the phase transitions and the superconductivity are symptoms of the structure — but one is not a pre-requisite for the other.

The lack of any resolvable phase changes in NCCO as a function of Ce doping and temperature supports the idea that structural changes are not strongly linked to the onset of superconductivity. The contrasting behaviour of LBCO and NCCO have been adequately explained by the respective presence and absence of apical oxygens to the Cu-O planes (see Chapter 8). The reported phase separation and local structural changes in NCCO cannot be ruled out by the results of this study but it is felt that phase separation may be due to sample preparation problems.

The anomalous behaviour of Pr in the 123 compounds and the question of its valence were the concern of the inelastic neutron scattering experiment reported in Chapter 9. A detailed fit to observed crystal electric field spectra has ruled out the suppression of superconductivity in Pr123 by hole-filling (in the Cu-O planes) as a result of a 4+ valence Pr ion. The valence has been determined to be essentially 3+ in character but a degree of dynamically mixed valence (Pr 4f hybridisation with the Cu-O planes) is suggested which could account for the large observed peak widths. This may also explain the high Néel temperature (for a R ion in R123) by allowing for a strong interaction between Pr ions via the Cu-O planes. The loss of superconductivity, on doping Pr onto the Y site of Y123, is probably due to the localisation of Cu-O plane holes because of the hybridisation with the Pr ions and/or magnetic pair breaking. The presence of Pr ions on the Ba sites is inferred from the excess magnetic scattering at high energy transfers. The valence of these ions has not been determined and their effect on the superconducting state is unknown.

The last issue — the effects of various Cu-site dopants in Y123 — was dealt with using high resolution magic angle spinning nuclear magnetic resonance. The results confirm that Zn and Ga substitute

preferentially onto different sites (the planes and chains). The slight decrease in T_c as a function of Ga doping is linked directly to a similar reduction in the DOS at the Fermi level. The drastic fall in T_c on doping Zn onto the Cu-O planes has been shown to be associated with induced localised fluctuating magnetic fields (the actual mechanism that gives rise to these fields has not been identified but the options are discussed in Chapter 10).

A common theme throughout all the studies presented in this thesis has been the role of the Cu-O planes in the 214 and 123 superconductors. The superconducting state has been shown to persist despite distortions of the planes by structural phase changes (in 214) but has proven to be highly sensitive to disruption of the electronic states in the planes by direct (Zn) or indirect (Pr) doping (in 123). There is some support from this work for theories of superconductivity that rely on antiferromagnetic fluctuations in the planes, as it is easiest to explain the effects of Pr and Zn doping, in Y123, as disrupting such a mechanism. No precise details of a magnetic model can be inferred.

A small role for the Cu-O chains in Y123 has been established by Ga doping and any general theories of superconductivity in these compounds must take this into account.

Very careful and thorough sample preparation has been shown to be essential in these materials; especially when considering the possible effects of various dopants and, more recently, when there is a suggestion of phase separation as in NCCO.

During the analysis of the data several suggestions for further work arose:

1. The NMR measurements on Zn and Ga doped Y123 should be extended to consider other dopants (such as Al, Fe, Ni etc.) on each site. This would check the assumption of an x=0 doping (extrapolated) chemical shift contribution to the total shift for chain site doping. It would establish whether all plane site dopants have the same effect as Zn. The measurements should also be repeated as a function of temperature. This could help to confirm the predicted Korringa behaviour with chain site doping. These suggestions have been taken-up by others in the department (see Dupree et al 1992 and Gencten 1992).

2. The idea that there may be magnetic inelastic neutron scattering from Pr ions on the Ba site in Pr123 could be checked by using samples such as $YBa_{2-x}Pr_xCu_3O_7$ (if they can be fabricated with sufficient confidence). This would require a large sample mass and high neutron flux/ long count-times but if the 110 - 140 meV peaks do result from such scattering then their intensities should be greater (relative to any from Pr on the Y site) than observered in this study.

3. Specific heat measurements on Pr123 should be performed at temperatures greater than 30K to allow for a better comparison between calculated (from CEF fits) and experimental data.

4. The issue of phase separation in NCCO could be addressed by a high resolution neutron diffraction study of multiple samples of Ce-doping in the range x=0.07 - 0.12. For each x the samples would have to be prepared carefully but under slightly different conditions. One important part of the process is the reduction of oxygen content. Phase separation could be looked for in the same samples before and after this stage.

5. Neutron diffraction on a single crystal of LBCO would be helpful in checking the assignment of the LTT phase as $P4_2/ncm$. This will have to wait until sufficiently large single crystals can be fabricated. It would be most interesting at the Ba-doping which corresponds to the highest onset temperature (and the reported dip in T_c) — $x=0.125$.

REFERENCES

Abrikosov A A and Gor'kov L P 1961 *Soviet Phys. JETP* **12** 1245

Alexandrov A S 1983 *Russ. J. Phys. Chem.* **57** 167

Allenspach P, Cheong S -W, Dommann A, Fischer P, Fisk Z, Furrer A, Ott H R and Rupp B 1989 *Z. Phys.* **B 77** 185

Anderson P W 1987 *Science* **235** 1196

Anderson P W and Zou Z 1988 *Phys. Rev. Lett.* **60** 132

Arend H, Hofmann R and Waldner F 1973 *Solid State Comm.* **11** 1629

Axe J D, Moudden A H, Hohlwein D, Cox D E, Mohanty K M, Moodenbough A R, and Xu Y 1989a *Phys. Rev. Lett.* **62** 2751

Axe J D, Cox D E, Mohanty K M, Moudden A H, Moodenbough A R, Xu Y and Thurston T R 1989b *IBM J. Res. Develop.* **33** 382

Baird N C and Burdett J K 1990 *Physica* **C 168** 637

Barbee T W III, Cohen M L, Bourne L C and Zettl A 1988 *J. Phys. C: Solid State Phys.* **21** 5977

Balakrishnan G, Dupree R, Farnan I, Paul D McK and Smith M E 1988 *J. Phys. C: Solid State Phys.* **21** L847

Balakrishnan G, Caves L W J, Dupree R, Paul D McK and Smith M E 1989 *Physica C* **161** 9

Bardeen J, Cooper L N and Schrieffer J R 1957 *Phys. Rev* **106** 162

Bednorz J G and Müller K A 1986 *Z. Phys.* **B 64** 189

Beille J, Cabanel R, Chaillout C, Chevalier B, Demazeau G, Deslandes F, Etourneau J, Lejey P, Michel C, Provost J, Raveau B, Sulpice A, Tholence J L and Tournier R 1987 *C. R. Acad. Sc. Paris II* **18** 304

Bilbro G and McMillan W L 1976 *Phys. Rev.* **B 14** 1887

Billinge S J L, Egami T, Richards D R, Hinks D C, Dabrowski B, Jorgensen J D and Volin K J 1991 *Physica* **C 179** 279

Boothroyd A T, Doyle S M, Paul D McK and Misra D S 1990 *Physica* **C 165** 17

Boothroyd A T, Caves L W J, Paul D McK and Osborn R 1991 *Bull Mater. Sci.* **14** 613

Boothroyd A T, Doyle S M, Paul D McK and Osborn R 1992a *Phys. Rev.* **B 45** 10075

Boothroyd A T, Doyle S M, and Osborn R 1992b (pre-print)

Bordet P, Hodeau J L, Marezio M, McWhan D B, Melville R J and Palmer S 1991 *Physica* **C 185-189** 543

Brewer J H, Ansaldo E J, Carolan J F, Chaklader A C D, Hardy W N, Harshman D R, Hayden M E, Ishikawa M, Kaplan N, Keitel R, Kempton J, Kiefl R F, Kussler W J, Kreizman S R, Kulpa A, Kuno Y, Luke B M, Migatake H, Nagamine K, Nakazawa Y, Nishida M, Nishiyama K, Ohkuma S, Riseman T M, Roehmer S, Schieger P, Shimida D, Stronach C E, Takabatake T, Uemura Y J, Watanabe Y, Williams D Ll, Yamazaki T and Yang B 1988 *Phys. Rev. Lett.* **60** 1073

Bulaevskii L N, Ginzburg V L and Sobyanin A A 1988 *Physica* **C 152** 378

Carbotte J P 1990 *Rev. Mod. Phys.* **62** 1027

Chen C H, Werder D J, James A C W P, Murphy D W, Zahurak S M, Fleming R M, Batlogg B and Schneemeyer L F 1989 *Physica* **C 160** 375

Chen D X, Sanchez A, Puig T, Martinez L M and Muñoz J S 1990 *Physica* **C 168** 652

Chu C W, Bechtold J, Gao L, Hor P H, Huang Z J, Meng R L, Sun Y Y, Wang Y Q , and Xue Y Y 1988 *Phys. Rev. Lett.* **60** 941

Civale L and Martinez E N 1988 *Phys. Rev.* **B 38** 928

Cooper L N 1956 *Phys. Rev.* **104** 1189

Dalichaouch Y, Torikachvili M S, Early E A, Lee B W, Seaman C L, Yang K N, Zhou H and Maple M B 1988 *Solid State Commun.* **65** 1001

David W I F, Harrison W T A, Gunn J M F, Moze O, Soper A K, Day P, Jorgensen J D, Hinks D G, Beno M A, Soderholm L, Capone II D W, Schuller I K, Segre C U, Zhang K and Grace J D 1987 *Nature* **327** 310

David W I F 1988 *Neutron Scattering at a Pulsed Source* ed. by Newport R J, Rainford B D and Cywinski R (Bristol: Adam Hilgar) 189

David W I F, Ibberson R M and Wilson C C 1988 Rutherford Appleton Laboratory Report RAL-88-103

Day P, Rosseinsky M, Prassides K, David W I F, Moze O and Soper 1987 *J.Phys. C: Solid State Phys.* **20** L429

Degiorgi L, Rusiecki S and Wachter P 1989 *Physica* **C 161** 239

de Jongh L J 1988 *Solid State Commun.* **22** 409

Dinger T R, Worthington T K, Gallagher W J and Sandstrom R L 1987 *Phys. Rev. Lett.* **58** 2687

Dupree R, Gencten A and Paul D McK 1992 *Physica* **C 193** 81

Eliashberg G M 1960 *Soviet Phys. JETP* **11** 996

Emery V J 1987 *Nature* **328** 756

— 1989 *Nature* **337** 345

Estéve D, Martines J M, Urbina C, Devoret M H, Collin G. Ribault M, Monod Ph. and Revcholevski A 1987 *Europhys. Lett.* **3** 1247

Fisher A J, Hayes W and Wallace D S 1989 *J. Phys.: Condens. Matter* **1** 5567

Fleming R M, Batlogg B, Cava R J and Reitman E A 1987 *Phys. Rev* **B 35** 7191

Freeman A J and Watson R E 1962 *Phys. Rev.* **127** 2058

Freeman A J and Desclaux 1979 *J. Magn. Magn. Mater.* **12** 11

Freeman A J, Yu J, Massidda S and Koelling D D 1988 *Theories of High Temperature Superconductivity* ed. by Woods Halley J (New York: Addison - Wesley) 53

Friedel J 1989 *J. Phys.: Condens. Matter.* **1** 7757

Fulde P, Keller J and Zwicknagl G 1988 *Solid State Phys.* **41** 1

Furrer A, Brüesch P and Unternährer P 1988 *Phys. Rev.* **B 36** 4616

Gavaler J R 1973 *Appl. Phys. Lett.* **23** 480

Geerk J, Xi X X and Linker G 1988 *Z. Phys. B — Condensed Matter* **73** 329

Gencten A 1992 Ph. D. Thesis, University of Warwick, Coventry, U.K. (in preparation)

Gering E, Renker B, Gompf F, Ewert D, Schmidt H, Ahrens R, Bonnet M and Dianoux A 1988 *Physica* **C 153-155** 184

Goodman G L, Loong C -K and Soderholm 1991 *J. Phys. Condens. Matter* **3** 49

Gorter C J and Casimir H B G 1934a *Physica* **1** 306

— 1934b *Phys. Z* **35** 963

— 1934c *Z. Tech. Phys.* **15** 539

Gough C E, Colclough M S, Forgan E M, Jordan R G, Keene P M, Muirhead C M, Rae A I M, Thomas N, Abell S and Sutton S 1987 *Nature* **326** 855

Grande Von B, Müller-Buschbaum Von Hk and Schweizer 1977 *Z. Anorg. Allg. Chem.* **428** 120

Gunn J M F 1988 *Neutron Scattering at a Pulsed Source* ed. by Newport R J, Rainford B D and Cywinski R (Bristol: Adam Hilgar) 13

Han Z P, Dupree R, Paul D McK, Howes A P and Caves L W J 1991 *Physica* **C 181** 355

Hazen R M, Prewitt C T, Angel R J, Ross N L, Finger L W, Hadidiacos C G, Veblen D R, Heaney P J, Hor P H, Meng R L, Sun Y Y, Wang Y Q ,Xue Y Y, Huang Z J, Gao L, Bechtold J and Chu C W 1988 *Phys. Rev. Lett.* **60** 1174

Hiratani M, Ito Y, Miyauchi K and Kudo T 1987 *Jpn. J. Appl. Phys.* **26** L1997

Hor P H, Meng R L, Wang Y Q , Gao L, Huang Z J, Bechtold J, Forster K and Chu C W 1987 *Phys. Rev. Lett.* **58** 1891

Howes A P 1992 Ph.D. Thesis, University of Warwick, Coventry, U.K.

Hubbard J 1963 *Proc. Roy. Soc.* **A 276** 283

— 1964 *Proc. Roy. Soc.* **A 281** 401

Imai T 1990 *J. Phys. Soc. Jpn.* **59** 2508

Imer J M, Patthey F, Dardel B, Schneider W D, Baer Y, Petroff Y and Zettl A 1989 *Phys. Rev. Lett.* **62** 336

Jahn H A and Teller E 1937 *Proc. R. Soc.* **A 161** 220

Jee C S, Kebede A, Nichols D, Crow J E, Mihalisin T, Myer G H, Perez I, Salomon R E and Schlottmann P 1989 *Solid State Commun.* **69** 379

Jee C S, Kebede A, Yuen T, Bloom S H, Kurie M V, Crow J E, Guertin R P, Mihalisin T, Myer G H and Schlottmann P 1988a *J. Magn. Magn. Mater.* **76,77** 617

Jee C S, Nichols D, Kebede A, Rahman S, Crow J E, Ponte Goncalves A M, Mihalisin T, Myer G H, Perez I, Salomon R E, Schlottmann P, Kuric M V, Yao Y S and Guertin R P 1988b *J. Superconduct.* **1** 63

Jorgensen J D, Schüttler H B, Hinks D G, Capone II D W, Zhang K, Brodsky M B and Scalapino D J 1987 *Phys. Rev. Lett.* **58** 1024

Jorgensen J D and Slaski M 1987 *J. Phys.* **C 20** L935

Jorgensen J D, Hinks D G, Lightfoot P, Richards D R, Dabrowski B, Pei S, Marx D T, Mitchell A W and Zheng Y S 1990 *Physica* **B 165-166** 1509

Jostarndt H -D, Walter U, Harnischmacher J, Kalenborn J, Severing A and Holland-Moritz E 1991 (pre-print)

Kajitani T, Kusaba K, Kikuchi M, Syono Y and Hirabayashi M 1988 *Jpn. J. Appl. Phys.* **27** L354

Kassman A J 1970 *J. Chem. Solids* **45** 401

Kebede A, Jee C S, Schwegler J, Crow J E, Mihalisin T, Myer G H, Salomon R E, Schlottmann P, Kuric M V, Bloom S H and Guertin R P 1989 *Phys. Rev.* **B 40** 4453

Kes P H 1992 *Supercond. Sci. Technol.* **5** S41

Kobayashi N, Ito A, Hiroi M and Iwasaki H 1991 *Physica* **C 185-189** 741

Labbé J and Bok J 1987 *Europhys. Lett.* **3** 1225

Lee W C, Klemm R A and Johnston D C 1989 *Phys. Rev. Lett.* **63** 1012

Le Page Y, Siegrist T, Sunshine S A, Schneemeyer L F, Murphy D W, Zahurak S M, Waszczak J V, McKinnon W R, Tarascon F M, Hull G W and Greene L H 1987 *Phys. Rev.* **B 36** 3617

Li W H, Lynn J W, Skanthakumar S, Clinton T W, Kebede A, Jee C S, Crow J E and Mihalisin T 1989 *Phys. Rev.* **B 40** 5300

Lightfoot P, Richards D R, Dabrowski B, Hinks D G, Pei S, Marx D T, Mitchell A W, Zheng Y S and Jorgensen J D 1990 *Physica* **C 168** 627

Loran J W, Mirza K A and Freeman 1990 *Physica* **C 171** 243

Lyons K B, Fleury P A, Schneemeyer L F and Waszczak J V 1988 *Phys. Rev. Lett.* **60** 732

Maeda H, Tanaka Y, Fukutomi M and Asano T 1988 *Jpn. J. Appl. Phys.* **27** L209

Maeda H, Koizumi A, Bamba N, Takayama-Muromachi E, Izumi F, Asano H, Shimizu K, Moriwaki H, Maruyama H, Kuroda Y, and Yamazaki H 1989 *Physica* **C 157** 483

Maeno Y, Tomita T, Kyogoku M, Awaji S, Aoki Y, Hosino K, Minami A and Fujita T 1987 *Nature* **328** 512

Maple M B, Yang K N, Torikachvili M S, Ferreira J M, Neumeier J J, Zhou H, Delichaouch Y and Lee B W 1987 *Solid State Commun.* **63** 635

Maple M B, Ferreira J M, Hake R R, Lee B W, Neumeier J J, Seaman C L, Yang K N and Zhou H 1989 *J. Less Common Met.* **149** 405

Markiewicz R S 1989a *J. Phys: Condens. Matter* **1** 8911

— 1989b *J. Phys: Condens. Matter* **1** 8931

— 1990 *J. Phys: Condens. Matter* **2** 6223

Marshall W and Lovesey S W 1971 "Theory of Thermal Neutron Scattering" (London: Oxford Univ. Press) a:7, b:81, c:83, d:94, e:106, f:107, g:169, h:154, j:170, i:Appendix B

Matsuda A, Kineshita K, Ishii T, Shibata H, Watanabe T and Yamada T 1988 *Phys. Rev.* **B 38** 2910

Micnas R, Ranninger J and Robaszkiewcz S 1987 *Phys. Rev.* **B 36** 4051

— 1990 *Rev. Mod. Phys.* **62** 113

Mila F and Rice T M 1989a *Physica* **C 157** 561

— 1989b *Phys. Rev.* **B 34** 11382

Millis A J, Monien H and Pines D 1990 *Phys. Rev.* **B 42** 167

Momono N, Ido M, Oda M, Yamada N and Onodera A 1991 *Physica* **C 183** 241

Moodera J S, Merservy R, Tkaczyk J E, Hao C X, Gibson G A and Tedrow P M 1988 *Phys. Rev.* **B 37** 619

Müller-Bushbaum Von Hk and Wollschläger W 1975 *Z. Anorg. Allg. Chem.* **414** 76

Murayama C, Môri N, Yomo S, Takagi H, Uchida S and Tokura Y 1989 *Nature* **339** 293

Nagao T, Mori H, Yonezawa F and Nishikawa K 1990 *Solid State Commun.* **74** 1309

Narasimha Rao C V, Jayaram B, Agarwal S K and Narlikar A V 1988 *Physica* **C 152** 479

Nekvasil V 1988 *Solid State Commun.* **65** 1103

Nekvasil V, Stehno J, Sebek J, Havela L, Sechovsky V and Svobada P 1988 *J. de Phys.* **49** C8-955

Neukirch U, Simmons C T, Sladeczek P, Laubschat C, Strebel O, Kaindl G and Sarma D D 1988 *Europhys. Lett.* **5** 567

Neumeier J J, Bjørnholm T, Maple M B, Rhyne J J and Gotaas J A 1990 *Physica* **C 166** 191

Nutley M P, Boothroyd A T and McIntyre G J 1992 *J. Magn. Magn. Mater.* **104-107** 623

Oda Y, Fugita H, Toyada H, Kaneko T, Kohara T, Nakada I and Asayama K 1987 *Jpn. J. Appl. Phys.* **26** L1660

Oh-Ishi K, Kikuchi M, Syono Y, Kobayashi N, Sasaoka T, Matsuhira T, Muto Y, and Yamauchi H 1988 *Jpn. J. Appl. Phys.* **27** L1449

Okai B, Kosuge M, Nozaki H, Takahashi K and Ohta M 1988 *Jap. J. Appl. Phys.* **27** L41

Onoda M, Shamoto S and Hosoya S 1987 *Jpn. J. Appl. Phys.* **26** L363

Parkin S S P, Lee V Y, Engler E M, Nazzal A I, Huang T C, Gorman G, Savoy R and Beyers R 1988a *Phys. Rev. Lett.* **60** 2539

Parkin S S P, Lee V Y, Nazzal A I, Savoy R, Beyers R and La Placa S J 1988b *Phys. Rev. Lett.* **61** 750

Paul D McK, Balakrishnan G, Bernhoeft N R, David W I F and Harrison W T A 1987 *Phys. Rev. Lett.* **58** 1976

Peng J L, Klavins P, Shelton R N, Radousky H B, Hahn P A and Bernardez L 1989 *Phys. Rev.* **B 40** 4517

Pennington C H, Durand D J, Slichter C P, Rice J P, Bukowski E D and Ginsberg D M 1989 *Phys. Rev.* **B 39** 2902

Phillips J C 1989 Physics of High-Tc Superconductors (Boston: Academic Press) a: ch **4**, b: pg 327

Pickett W E 1989 *Rev. Mod. Phys.* **61** 433

Poole C P Jr., Datta T and Farach H 1988 *Copper Oxide Superconductors* (New York: Wiley) chapter 1

Prassides K and Kroto H 1992 *Physics World* **5** 44

Rainford B D 1988 *Neutron Scattering at a Pulsed Source* ed. by Newport R J, Rainford B D and Cywinski R (Bristol: Adam Hilgar) Ch. 20

Reitveld H M 1967 *Acta Crystallogr.* **22** 151

— 1969 *J. Appl. Crystallogr.* **2** 65

Rodríguez-Carvajal J, Fernández-Díaz M T, Fernández F and Saez-Puche R 1990a *Europhys. Lett.* **11** 261

Rodríguez-Carvajal J, Fernández-Díaz M T and Martínez J L 1990b Preprint (to appear in *J. Phys: Cond. Matt.*)

Rosenberg H M 1978 *The Solid State 2nd Ed.* (Oxford:Clarendon) 236

Ruvalds J 1988 *Theories of High Temperature Superconductivity* ed. by Woods Halley J (New York: Addison - Wesley) 91

Sankawa I, Sato M and Konaka T 1988 *Jpn. J. Appl. Phys.* **27** L28

Schrieffer J R, Wen X G and Zhang S C 1988 *Phys. Rev. Lett.* **60** 944

Sigmund E and Stevens K W H 1988 *Physica* **C 152** 349

Sheng Z Z, Herman A M, El Ali A, Almasan C, Estrada J, Datta T and Matson R J 1988 *Phys. Rev. Lett.* **60** 937

Soderholm L, Zhang K, Hinks D G, Beno M A, Jorgensen J D, Segre C U and Schuller I K 1988 *Nature* **328** 604

Soderholm L and Goodman G L 1989 *J. Solid State Chem* **81** 121

Soderholm L, Loong C -K, Goodman G L and Dabrowski B D 1991 *Phys. Rev.* **B 43** 7923

Soderholm L, Loong C -K, and Kern S 1992 *Phys. Rev.* **B 45** 10062

Stevens K W H 1952 *Proc. Phys. Soc. London Sect.* **A 65** 209

Suzuki T and Fujita T 1989 *Physica* **C 159** 111

Takagi H, Uchida S and Tokura Y 1989 *Phys. Rev. Lett.* **62** 1197

Takahashi T, Katayama-Yoshida H and Matsuyama H 1990 *Z. Phys. B — Condensed Matter* **78** 343

Tarascon J M, Greene L H, Barboux P, McKinnon W R, Hull G W, Orlando T P, Delin K A, Foner S and McNiff Jr. E J 1987 *Phys. Rev.* **B 36** 8393

Tarascon J M, Barboux P, Miceali P F, Greene L H, Hull G W, Eibschutz M and Sunshine S A 1988 *Phys. Rev.* **B 37** 7458

Taylor A D, Boland B C, Bowden Z A and Jones T J L 1987 *Rutherford Appleton Laboratory internal report* RAL-87-012

Taylor A D, Osbourn R, Lovesey S W, Bowden Z A, Williams W G, Balcar E, McEwan K A and Stirling W G 1988 *Phys. Rev. Lett.* **61** 1309

Tilley D R and Tilley J 1990 *Superfluidity and Superconductivity* 3rd ed. (Bristol: Adam Hilger) a: ch 4, b: ch 5, c: ch 8, d: ch 6, e: ch's 9-11, f: ch 2

Tokura Y, Takagi H and Uchida S 1989a *Nature* **337** 345

Tokura Y, Torrance J B, Nazzal A I, Takagi H and Uchida S 1989b *Mechanisms of High Temperature Superconductivity, Springer Series in Materials Science II* (Berlin: Springer-Verlag) 294

Tolfield B C, Jacobson A J and Fender B E F 1972 *J. Phys. C: Solid State Phys.* **5** 2887

Walstedt R E, Warren W W Jr., Dupree R and Gencten A 1991 (preprint)

Walter U 1984 *J. Phys. Chem. Solids* **45** 401

Walter U, Holland-Moritz E, Severing A, Erle A, Schmidt H and Zirngiebl E 1988 *Physica* **C 153-155** 170

Wang J H, Chen G H, Chu X, Yan Y F, Zheng D N, Mai Z H,Yang Q S and Zhao Z X 1988 *Supercond. Sci. Technol.* **1** 27

Warren W W Jr., Walstedt R E, Brennert G F, Espinosa G P, and Remeika J P 1987 *Phys. Rev. Lett.* **60** 1860

Warren W W Jr., Walstedt R E, Brennert G F, Cava R J, Tycko R, Bell R F and Dabbagh G 1989 *Phys. Rev. Lett.* **62** 1193

Williams W G and Lovesey S W 1989 *Contemporary Physics* **30** 35

Windsor C G 1981 *Pulsed Neutron Scattering* (London: Taylor & Francis)

Worthington T K, Gallagher W J and Dinger T R 1987 *Phys. Rev. Lett.* **59** 1160

Wu M K, Ashburn J R, Torng C J, Hor P H, Meng R L, Gao L, Huang Z J, Wang Y Q and Chu C W 1987 *Phys. Rev. Lett.* **58** 908

Wu J B, Ying H P and Li W Z 1992 *Phys. Lett.* **A 161** 458

Xiao G, Cieplak M Z, Gavrin A, Streitz F H, Bakhshai A and Chien C L 1988a *Phys. Rev. Lett.* **60** 1446

Xiao G, Cieplak M Z, Musser D, Gavrin A, Streitz F H, Chien C L, Rhyne J J and Gotaas J A 1988b *Nature* **332** 238

Yamada K, Matsuda M, Endoh Y, Keimer B, Birgeneau R J, Onodera S, Mizusaki J, Matsura T and Shirane G 1989 *Phys. Rev.* **B 39** 2336

Yang K N, Dalichaouch Y, Ferreira J M, Lee B W,Neumeier J J, Torikachvili M S, Zhou H, Maple M B and Hake R R 1987 *Solid State Commun.* **63** 515

Yoshida K H, Hirooka T, Oyamada A, Okabe Y, Takahashi T, Sasaki T, Ochiai A and Suzuki T 1988 *Physica* **C 156** 481

Yvon K and François M 1989 *Z Phys. B — Condensed Matter* **76** 413

Zacher R A 1987 *Phys. Rev.* **B 36** 7115

BIBLIOGRAPHY

General:

Preparation of Ph.D. Theses PHYS/PG/3 (University of Warwick) 1988

Solid State Physics Ashcroft N W and Mermin N D (Saunders College: Philadelphia) 1988

The Solid State 2nd ed. Rosenberg H M (Oxford: Clarendon) 1978

X-ray Diffraction Procedures for Polycrystalline and Amorphous Materials 2nd Ed. Klug H P and Alexander L E (New York: Wiley) 1974

Neutron Scattering:

HRPD : The High Resolution Powder Diffractometer at ISIS -- An Introductory Users Guide Version 1.0 David W I F, Akporiaye D E, Ibberson R M and Wilson C C (unpublished -- copies from Rutherford Appleton Laboratory, UK) 1988

Neutron Scattering at a Pulsed Source ed. by Newport R J, Rainford B D and Cywinski R (Bristol: Adam Hilgar) 1988

Theory of Neutron Scattering from Condensed Matter Lovesey S W (Oxford: Clarendon) 1984

Theory of Thermal Neutron Scattering Marshall W and Lovesey S W (London: Oxford Univ. Press) 1971

Treatise on Materials Science and Technology **15** (*Neutron Scattering*) ed. by Kostorz G (New York: Academic Press) 1979

NMR:

Experimental Pulse NMR — A Nuts and Bolts Approach Fukushima E and Roeder S B W (New York: Addison - Wesley) 1981

Nuclear Magnetic Resonance General Concepts and Applications Paudler W W (New York: Wiley) 1987

Principals of Magnetic Resonance 3rd Ed. Slichter C P (Berlin: Springer-Verlag) Springer Series in Solid State Physics 1 Ed. by Fulde P. 1990

Principals of Nuclear Magnetism Abragam A (Oxford:Clarendon) 1984

Principals of Nuclear Magnetic Resonance Abragam A (Oxford:Oxford Univ. Press) 1982

Superconductivity:

Copper Oxide Superconductors Poole C P Jr., Datta T and Farach H (New York: Wiley) 1988

Superfluidity and Superconductivity 3rd ed. Tilley D R and Tilley J (Bristol: Adam Hilger) 1990

Physics of High-Tc Superconductors Phillips J C (Boston: Academic Press) 1989

Theories of High Temperature Superconductivity ed. by Woods Halley J (New York: Addison - Wesley) 1988